Anomalous $g t\bar{t}$ coupling in Single-Lepton $t\bar{t}$ events from $p\overline{p}$ Collisions at $\sqrt{s} = 1.8$ TeV

by

Kwok Ming Chan

Submitted in Partial Fulfillment
of the
Requirements for the Degree
Doctor of Philosophy

Supervised by
Professor Paul Slattery
Department of Physics and Astronomy
The College
Arts and Sciences

University of Rochester
Rochester, New York

2005

To those with a passion for *truth*.

Curriculum Vitae

The author was born in Hong Kong, China on August 4, 1973. He attended the University of Chicago from 1992 to 1996, and graduated with a Bachelor of Arts degree in 1996. He came to the University of Rochester in the fall of 1996 and began graduate studies in Physics. Upon receiving the Master of Arts degree in 1998, he joined the Rochester group at Fermilab on the DØ experiment. He pursued his research on the top quark under the direction of Professor Paul Slattery and supervision of Professor Tom Ferbel.

Acknowledgments

First of all I would like to thank my adviser, Paul Slattery, for his guidance and support on academic and other issues all through these years. His many insightful comments on this analysis have been invaluable.

Special thanks to Tom Ferbel who encouraged me to pursue this analysis, and shared his wisdom on many of the complex issues that came along. His energy and enthusiasm has been the driving force behind this work.

Many thanks to Marek Zieliński and Vishnu Zutshi from whom I learned much about the inner workings of the detector and other software and data analysis issues. The many discussions with Marek on this analysis have also been illuminating.

The $gt\bar{t}$ Monte Carlo generator from Aurelio Juste and his expert advices had been instrumental to the analysis. His numerous suggestions to improve the analysis have vastly expanded my understanding of many statistical and analysis issues.

I would like to thank Juan Estrada and Florencia Canelli for developing and their help in applying the method of analysis used here. Brian Connolly showed me the crucial steps in generating Monte Carlo events on the VAX system which made it easier for me to generate new events on a different system.

I would also like to thank the many colleagues who I had the pleasure to work with and learn from, especially Gaston Gutierrez, Qi-Zhong Li, and Volker Buescher.

Lastly, I thank my family for their unyielding supports, without which it would have been much harder to complete this work.

Abstract

Using the effective Lagrangian formulation with the requirements of Standard Model SU(3)×SU(2)×U(1) symmetries, the leading order effects of new physics at an energy scale Λ on the $gt\bar{t}$ vertex can be shown to be determined by the strengths of three anomalous couplings C_{tG}, C_{qG} and $C_{tG\phi}$. Applying a method designed to utilize the full kinematic information of an event on the top-quarks collected from $p\bar{p}$ collisions at $\sqrt{s}$=1.8 TeV by the DØ experiment during Run I of the Fermilab Tevatron, we have measured $\frac{C_{qG}}{\Lambda^2} = 2.84 \pm 1.78(\mathrm{stat}) \pm 0.88(\mathrm{syst})$, where Λ is set to be 1 TeV and the other two couplings are assumed zero. This is the first direct measurement of $gt\bar{t}$ coupling and the result is consistent with the Standard Model prediction of zero.

Contents

List of Figures

List of Tables

Chapter 1

Theory

1.1 The Standard Model

The development of the theory of special relativity, quantum mechanics and ingenious experimental techniques in the past century resulted in a tidal wave of new discoveries at unimaginably small length scales. Atoms and nuclei, once regarded as the smallest unit of matter, turned out to be systems composed of even smaller constituents. As we currently understand, all matter is made up of identical copies of only one dozen fundamental particles. Six of them are called quarks and the other six leptons. These matter particles interact with each other through exchanges of force-mediating particles called gauge bosons. (And, interestingly, some of these mediators can also interact with each other.) There are four known types of interactions, or forces, of varying strengths and characteristics [1]. Different theories are required to describe these interactions, though there are continuing efforts (some successful) to combine these theories into a single formalism, such as the Grand Unified Theory (GUT) [2, 3] or Theory of Everything (TOE) [4]. The currently most widely accepted theories of these elementary particles and their interactions are collectively known as the Standard Model (SM) [3].

The fundamental particles are distinguished by their different quantum numbers, or intrinsic properties, such as mass, charge and angular momentum (spin), which affect how they interact with one another. Some of the properties are listed in Table 1.1. Particles of half integer spins are called fermions, and follow the Pauli exclusion principle and Fermi-Dirac statistics, while those of integer spins are called bosons, and obey Bose-Einstein statistics. Quarks and leptons, the known fermions, are believed to be pointlike and structureless down to a scale of $< 10^{-17}$ m. They can be arranged into three groups, or generations, with each group containing members that share almost all properties with those in other groups, except for mass. (In the Standard Model, neutrinos are customarily assumed to be all massless and so are distinguished between generations by the processes in which they take part, although recent experiments have shown evidence of neutrino "oscillation" between generations, suggesting a non-zero mass for neutrinos [5].) The first generation consist of the up and down quarks, the electron and the electron neutrino. The electron, as defined, has an electric charge (e) of -1, while the quarks have fractional electric charges of $+2/3$ and $-1/3$. Essentially all ordinary matter is made up of members of the first generation (for example, protons and neutrons are made mostly of up and down quarks.) Particles in the higher generations are more massive and unstable, and eventually decay to particles of the first generation (or into photons). These particles can be produced when high energy cosmic rays interact in the atmosphere, or at man-made particle accelerators. The explanation for having three generations of such similar particles remains an open and actively pursued question.

The variety of fundamental particles (almost) doubles when antimatter is included. As we now know, all fundamental particles have corresponding antiparticles that have same mass but reversed charge and other properties [6]. Antiparticles are

Table 1.1: Particles in the Standard Model [3].

	Particle Name	Charge	Mass (GeV)	Interaction
Leptons (spin = 1/2)	Electron (e)	-1	0.000511	EM, Weak
	Electron neutrino (ν_e)	0	$<3 \times 10^{-6}$	Weak
	Muon (μ)	-1	0.1057	EM, Weak
	Muon neutrino (ν_μ)	0	$<0.19 \times 10^{-3}$	Weak
	Tau (τ)	-1	1.777	EM, Weak
	Tau neutrino (ν_τ)	0	$<18.2 \times 10^{-3}$	Weak
Quarks (spin = 1/2)	Up (u)	+2/3	1.5 to 4.5 $\times 10^{-3}$	EM, Weak, Strong
	Down (d)	-1/3	5 to 8.5 $\times 10^{-3}$	EM, Weak, Strong
	Strange (s)	-1/3	80 to 155 $\times 10^{-3}$	EM, Weak, Strong
	Charm (c)	+2/3	1 to 1.4	EM, Weak, Strong
	Bottom (b)	-1/3	4 to 4.5	EM, Weak, Strong
	Top (t)	+2/3	178	EM, Weak, Strong
Gauge Bosons (spin = 1)	Photon (γ)	0	0	EM
	W boson (W)	1.	80.4	Weak
	Z boson (Z)	0	91.2	Weak
	Gluon (g)	0	0	Strong

denoted by placing a bar above the symbols of their ordinary-particle counterparts. Fermions and antifermions can only be created and annihilated in pairs from vacuum. The annihilation of particle and antiparticle provides a way to create new particles. The proton-antiproton ($p\overline{p}$) collision which produced the top quarks at Fermilab is an example of this (although it should be pointed out that it is the constituent fundamental particles inside the proton and antiproton that annihilate). Some of the neutral bosons, such as the photon, are their own antiparticles.

The four known fundamental forces of nature are the electromagnetic (EM), strong, weak, and gravitational forces. The first three are described by the Standard Model. The electromagnetic force is probably the most familiar, since it is the force that underlies chemistry and biology. The strong force is responsible for binding quarks inside the proton, neutron and the nucleus of atoms, while the weak force is responsible for β decays of neutrons and interactions of neutrinos. The gravitational force, while ubiquitous, is very weak for individual particles separated at distance of greater than or about 10^{-17} m and is not included in the Standard Model.

In quantum mechanics, each matter particle is represented by a wavefunction, or matter field, with quantized energy states. Quantum field theory [7] takes this further by quantizing the forces, and describes all interactions as excitations of quantum fields. The quanta of the force fields are interpreted as the force mediating particles of the interaction. As in classical field theories, each quantum field theory is characterized by a Lagrangian density, which is a function of the field operators and can be used to derive the equations of motion, or space-time-dependent equations of the fields. These equations, however, usually cannot be solved exactly. To derive reasonable prediction for physical processes, approximation techniques are required. The most commonly used is perturbation theory, in which interactions are treated as small perturbations of the vacuum state (lowest energy state of a free particle). The result is an infinite series of calculable additive terms in increasing order of the coupling strength of the interaction. When the coupling strengths are small, the leading terms can provide a good approximation to the exact solution. Problems arise, however, when higher-order terms are needed but found to be infinite. This is remedied by a process called *renormalization*, in which positive infinite terms are matched to and cancel negative infinite terms, with the remaining terms providing a finite measurable result [8, 9].

At the heart of the Standard Model is the concept of symmetries. A symmetry is the property of a theory such that a transformation leaves the theory (i.e., its physical predictions) invariant. An example of this is Lorentz invariance.

While quantum field theories allow many possibilities in formulating models for particle interactions, the simplest and most elegant way to proceed is through the use of gauge theories [10], which form the foundation of the Standard Model. In gauge theories, Lagrangians are required to be invariant under a local (in the space-time vicinity of the interaction) gauge transformation. To satisfy this requirement, new fields (additional terms in the Lagrangian) are needed and can be introduced, which then turn out to represent the observed interaction. These fields are known as gauge fields, and the corresponding force mediators are called the gauge bosons. Standard Model therefore has this remarkable property that every interaction is the result of an underlying symmetry. By Noether's theorem [11], each symmetry in a theory also represents a conserved quantity. This helps in determining the specific form of any new interaction if the conserved quantity is known, or vice versa. Finally, gauge theories also possess a particularly crucial characteristic: that they are renormalizable. A qualitative account of the gauge theories can be found in Ref.[12]

1.1.1 Quantum Electrodynamics

The quantum theory that describes the interaction between electrically charged particles is Quantum Electrodynamics (QED) [13]. The electromagnetic (EM) force is transmitted via the exchange of quanta of the EM field, or photons. The strength of the EM force, which is characterized by a coupling constant α_{EM}, increases with increasing energy and decreases with increasing distance. The local gauge transformation that is invariant in this theory forms a mathematical group called the U(1), or unitary group of dimension 1 [10].

1.1.2 Quantum Chromodynamics

The strong force is described by Quantum Chromodynamics (QCD) [3, 14]. The gauge boson of this theory is the massless gluon. Analogous to electric charge, the strong force is experienced by particles that carry “color” charge. There are three of these charges: “red”, “green”, and ”blue” (R,G,B) (antiparticles carry the anticolor charges $\overline{R}$, $\overline{G}$,$\overline{B}$). When these quantum numbers are combined, they can produce objects that have color, but also colorless particles. Quarks and gluons are the only particles that carry color charge. Protons and neutrons are colorless objects consisting of three quarks of different color, and mesons are colorless objects composed of quark-antiquark pairs that carry no net color. Only these kinds of combination of quarks exist freely in nature, because other combinations produce a non-binding potential. Since gluons carry the color charge, they can also couple to each other, and should be able to produce colorless glueballs [15]. An important feature of QCD is that the coupling strength α_{STRONG} decreases with increasing energy and grows with increasing distance. As a result, quarks behave increasingly like free particles at high energy (small distances). This is known as “asymptotic freedom”, and suggest the use of perturbative calculations at high energy [16]. At large distances, however, the coupling grows rapidly. This phenomenon is called “confinement”, and keeps quarks and gluons always in bound states [17]. Even in high energy collisions where “free” quarks or gluons may be produced, rather than traveling a large distance, they quickly generate energetically more favorable quark-antiquark pairs (e.g., mesons) from the vacuum, until all available energy is dissipated. This process is known as fragmentation or hadronization [18], and turns a quark or gluon into a collimated “jet” of mesons that move in approximately the same direction as the original quark or gluon. As a result, no free quarks have ever been observed directly in any production processes. The local gauge transformation underlying QCD is based on the group SU(3), which stands for Special Unitary group of 3 components [10].

1.1.3 Weak interaction

The weak force acts on all matter particles, regardless of charge or mass. It is the only interaction (other than gravity) that neutrinos are known to participate in. It allows particles to change flavor within (and even between) the generations. There are three force mediators. Two of them, the W^+ and W^- are electrically charged, and provide the flavor transitions between "weak isospin" partners (e and ν_e, u and d quarks, etc) [10] The third, the Z^0, is electrically neutral. As opposed to the massless photons and gluons, these gauge bosons, also known as $Intermediate\ Vector\ Bosons(IVBs)$ have masses close to 100 GeV/c^2. As the name suggests, the characteristic coupling strength of the weak interaction is much smaller than the EM and strong interactions, and has a short range ($\approx 10^{-3}$ fm) characterized by the massive gauge bosons. The theory that describes the weak force is the V-A theory [19], and it is part of the SM.

1.1.4 Electroweak Symmetry and Symmetry Breaking

In the quest to remove some of the inconsistencies in the theory that describes the weak interaction, and to combine the seemingly disparate weak and EM interactions, the EM and weak forces were unified into the *electroweak* (EW) interaction through the introduction of a larger symmetry [21]. In this EW model, the EM and weak interaction are only different manifestations of the same force. Four fields are postulated in the Lagrangian: W^+, W^-,W^0 and B^0, with the charged fields corresponding to the W bosons of the weak force. The neutral components mix together to yield the photon and the Z^0. One immediate problem with this model is that all particles must remain massless for the theory to be renormalizable (or gauge invariant). This is solved through the introduction of the *Higgs mechanism*, in which a new field, called the Higgs field, with a non-zero vacuum expectation value (VEV), breaks the symmetries present in the Lagrangian and generate massive particles [20]. This effect, in which the Lagrangian has a set of symmetries that are not shared by the states, is referred to as a spontaneously broken symmetry, and gives rise to the difference between EM and weak force that we see at energies below the VEV. The gauge invariant transformation of the electroweak sector forms a combined group SU(2)×U(1), with SU(2) referring to the weak isospin and U(1) to the symmetry of electromagnetism [10].

1.2 Top Production and Decay

The top quark is the heaviest of all known fundamental particles. It was first observed by the CDF and DØ collaborations in 1995 [26, 25]. Since its discovery, many measurements of its mass have been performed. The current world average is 172.7±2.9 GeV/c^2[27].

The production of $t\bar{t}$ pairs can be calculated in QCD, with the top quarks decaying via the weak interaction. At the Tevatron of the Fermi National Accelerator Laboratory (Fermilab), the primary mechanisms for $t\bar{t}$ production are expected to be from quark-antiquark annihilation $q\bar{q} \rightarrow t\bar{t}$ and gluon-gluon fusion $gg \rightarrow t\bar{t}$. The lowest order diagrams for these processes are illustrated in Fig. 1.1 The relative contribution of these processes changes with $\sqrt{s}$. At the Tevatron energy ($\sqrt{s} = 1.8$ TeV), 90% of the $t\bar{t}$ production takes place through the $q\bar{q}$ annihilation process [29].

With a high mass of about 175 GeV/c^2, the top quark possess a unique feature

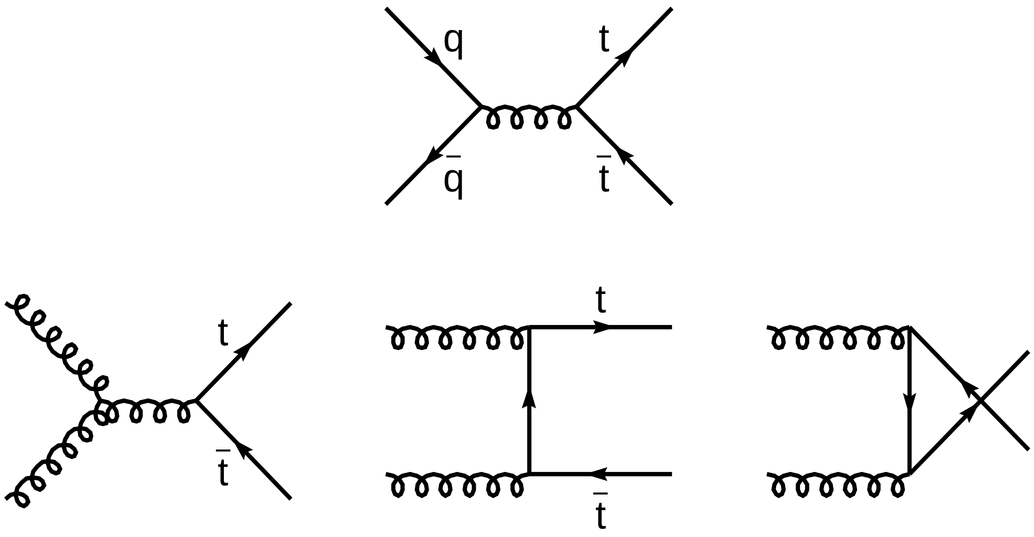

Figure 1.1: Leading order Feynman diagrams for $t\bar{t}$ production at the Tevatron. The upper diagram contributes to the $q\bar{q} \to t\bar{t}$ and the lower diagrams contribute to the $gg \to t\bar{t}$ process.

that it decays before it hadronizes [30]. As a result, many intrinsic properties of the top quarks at production time (mass, spin, etc) are passed directly on to their decay products, with little effect from other QCD interactions. Although they still cannot be observed directly as free quarks, through the study of their decay products, top quarks can provide the best opportunity for understanding the precise production dynamics of quark-antiquark pairs.

In the Standard Model, a top quark, with $M_t > M_W + M_b$, almost always decays into a real W^+ boson and a b quark, while the antitop decays to W^- and $\bar{b}$ [30]. The b will form a jet, and the W^+ will decay either into a lepton pair (l^+, $\overline{\nu}_l$) or into quark-antiquark $u\overline{d}$ or $c\overline{s}$ pairs (which in turn become two jets). To leading order approximation, each possible final state of the W is equally probable, but each quark flavor counts separately, and three times, since quarks come in three colors. Thus the branching ratio for each lepton flavor is 1/9, while that for each quark flavor is

Table 1.2: $t\bar{t}$ decay branching ratios for different combinations of decay channels. The factor of 2/3 for $q\bar{q}$ reflects the two hadronic channels and three colors for all quarks: 2×3×1/9=2/3.

	$W \rightarrow e\nu_e$ (1/9)	$W \rightarrow \mu\nu_\mu$ (1/9)	$W \rightarrow \tau\nu_\tau$ (1/9)	$W \rightarrow q\bar{q}$ (2/3)
$W \rightarrow e\nu_e$ (1/9)	1/81	1/81	1/81	2/27
$W \rightarrow \mu\nu_\mu$ (1/9)	1/81	1/81	1/81	2/27
$W \rightarrow \tau\nu_\tau$ (1/9)	1/81	1/81	1/81	2/27
$W \rightarrow q\bar{q}$ (2/3)	2/27	2/27	2/27	4/9

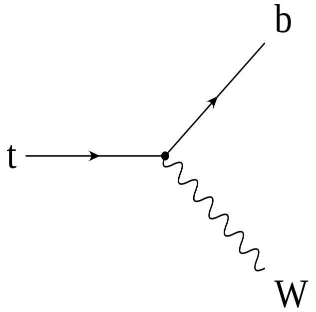

Figure 1.2: Decay of the top (t) quark into a W boson and a bottom (b) quark.

1/3. The breakdown of the decay modes is shown in Table 1.2. Depending on the W decay, $t\bar{t}$ events are generally divided into three categories:

- All-jets channel: $t\bar{t}$ events when both Ws decay into jets constitute 44% (36/81) of all $t\bar{t}$ events, and represent the largest branching fraction. However, these events also have tremendous background from multijet events, which are produced copiously in $p\bar{p}$ collisions. Much care is therefore required to reduce the presence or effect of such background.

- Dilepton channel: These are $t\bar{t}$ events in which both Ws decay to lepton pairs. Events with the τ lepton, being difficult to detect with high efficiency, are generally ignored. The rest are usually further divided into the ee, $\mu\mu$ and

$e\mu$ channels. This constitutes about 5% (4/81) of the total $t\bar{t}$ events. Such events have least background of the three $t\bar{t}$ categories (and the $e\mu$ channel is especially clean), but suffer from a small branching ratio and the loss of information due to the two "missing" neutrinos, which are not measured.

- Lepton + jets channel: The remaining $t\bar{t}$ events, in which one W decays to leptons and the other decays to jets, belong to the lepton + jets channel. For the same reason as in the dilepton channel, only events containing an electron or muon are included. This represent a branching fraction of 24/81 (30%). For these events, the knowledge of the W mass can, in principle, be used to reconstruct the full kinematics of the top quarks, with only a two-fold ambiguity in the longitudinal momentum (p_z) of the neutrino (this is not quite the case because the flavors of the jets are also unknown).

The decay modes used in the analysis presented in this dissertation are the lepton + jets modes. This final state contains a lepton (electron or muon), a neutrino, two b jets, and two additional jets from the hadronic W decay.

1.3 Beyond the Standard Model

The predictions of Standard Model are in agreement with virtually all known experiments [22, 23]. However, there remain unanswered questions about some of its features and predictions (see e.g. Ref. [24]). It is widely believed that there is still new physics, i.e., new particles and interactions, that have as yet been unobserved because of their high mass energy scales.

In searching for new physics, there are two general approaches. One, is to develop specific models of new particles and interactions at higher energy scales that would aim to solve some or all shortcomings of the Standard Model. If the masses of such particles are sufficiently small to be produced in current experiments, the signatures of these new particles can be sought in the data. The other approach, is to look for virtual effects due to new high-energy interaction in data that appear consistent with SM interactions. Our analysis is based on the second approach.

1.3.1 Effective Lagrangian

In an “effective” field theory, or the effective Lagrangian method, a series of terms of increasing (mass) dimensions, divided by powers of the energy scale of the new physics, are added to the SM Lagrangian. These non-standard terms contain all field operators that satisfy certain desired symmetries or properties. Any two specific new physics theories will in general contain some or all of these terms. Or, to put it in another way, an effective Lagrangian can represent or parametrize an entire class of new theories that have some common features such as symmetries, by including all possible terms that respect that feature. The final constraints on the relative strengths of these terms, and thus the full theory, can only be determined from experiment.

At energies much below the scale of new physics, the lowest order (dimension) terms in the expansion determine the physical effects, because the higher order terms are greatly suppressed by the value of the scale. By requiring SU(3)×SU(2)×U(1) invariance, operators of dimension five cannot be constructed because these violate lepton-number conservation[31]. Therefore, extension to the SM Lagrangian with operators that satisfy SU(3)×SU(2)×U(1) invariance starts at dimension-six. The leading-order effective Lagrangian, including the effect of new physics can be written as:

$$L_{eff} = L_0 + \frac{1}{\Lambda^2}\sum_i C_i O_i \tag{1.1}$$

where L_0 is the SM Lagrangian, Λ is the energy scale of new physics, O_i are SU(3)×SU(2)×U(1) invariant dimension-six operators, with strengths represented by the coupling constants C_i.

1.3.2 Anomalous $gt\bar{t}$ Couplings

The discovery of the top quark provided further proof for the validity of the Standard Model and at the same time presented a tool for exploring the higher-energy regime. With a mass that is a factor of 35 larger than that of the next heaviest fermion (the b quark), the top quark is naturally regarded to be more sensitive to new physics, which is expected to appear beyond the energy scale of electroweak symmetry breaking. Without knowing the exact structure of the new physics, the effective-Lagrangian method provides just the right tool to study any effect that new physics might have on SM interactions.

Of all the dimension-six operators that satisfy SU(3)×SU(2)×U(1) invariance, there are 3 CP-conserving operators that contribute to non-standard couplings at the $gt\bar{t}$ vertex. For the $q\bar{q} \to t\bar{t}$ process, with "on-shell" or real t and $\bar{t}$, the CP-conserving operators provides new contributions to the $gt\bar{t}$ vertex given by [32]:

$$\Gamma^{\mu}_{gt\bar{t}} = T^i[\gamma^{\mu}(F_V) + (\gamma^{\mu}\gamma^5 - \frac{2m_t}{q^2}q^{\mu}\gamma^5)F_A + \frac{p_t^{\mu} - p_{\bar{t}}^{\mu}}{2m_t}F_M] \tag{1.2}$$

where q, p_t and $p_{\bar{t}}$ are the momenta of the gluon, t and $\bar{t}$, respectively. $T^i = \lambda^i/2$ with

λ^i $(i = 1, \ldots, 8)$ denoting the Gell-Mann matrices. The form factors corresponding to the new interactions are:

$$\begin{aligned} F_V(q^2) &= -\frac{q^2}{2}[\frac{C_{tG}}{\Lambda^2} + \frac{C_{qG}}{\Lambda^2}] + 2\sqrt{2}vm_t\frac{C_{tG\phi}}{\Lambda^2} \\ F_A(q^2) &= -\frac{q^2}{2}[\frac{C_{tG}}{\Lambda^2} - \frac{C_{qG}}{\Lambda^2}] \\ F_M(q^2) &= 2\sqrt{2}vm_t\frac{C_{tG\phi}}{\Lambda^2} \end{aligned}$$

For a given Λ, the form factors are completely determined by the coupling strengths C_{tG}, C_{qG} and $C_{tG\phi}$. In the rest of the analysis, for convenience, the factors $\frac{C_{tG}}{\Lambda^2}$, $\frac{C_{qG}}{\Lambda^2}$ and $\frac{C_{tG\phi}}{\Lambda^2}$, with Λ being customarily set to 1 TeV$/c^2$ (or put in another way, C_{tG}, C_{qG} and $C_{tG\phi}$ in units of $(\Lambda/\text{TeV})^{-2}$), will be referred to as A_1, A_2 and A_3, respectively.

Because of poor statistics, and since this is the first analysis attempting to measure the $gt\bar{t}$ coupling , we restrict our attention to only one of the three couplings, and assume that the other two have their SM values. As the studies by Hikasa et al. [32] show, a change in A_3 has little effect on the "shape" of distributions in $t\bar{t}$ events, and since the method we employ in this analysis emphasizes the event topology, we will focus on A_1 and A_2.

The presence of anomalous $gt\bar{t}$ couplings modifies the dynamics of $q\bar{q} \to t\bar{t}$ process in several ways. We discuss here three of the observables that are affected. Differential cross sections are derived using a Madgraph-based [33] matrix element generator[34], which utilizes the HELAS routines[35] for calculating helicity amplitudes. The SM $gt\bar{t}$ coupling is modified within the generator to allow non-standard contributions. We concentrate on only the $q\bar{q} \to t\bar{t}$ process, ignoring the ≈ 10 % contribution from $gg \to t\bar{t}$. Results shown are for a top and W mass of 175 and 80.4

GeV/c^2, respectively, at $p\overline{p}$ $\sqrt{s} = 1.8$ TeV, using the CTEQ3M parton distribution function [36] which is used in Run I Monte Carlo generation of $t\overline{t}$ events.

The contributions of the operators associated with A_1 and A_2 are energy dependent and therefore modify the $t\overline{t}$ invariant mass distribution from that of the SM, (this is not the case for A_3)[32]. Figure 1.3(a) shows the $t\overline{t}$ invariant mass distribution for different values of A_1, with the other couplings set at SM values, while 1.3(b) shows the same distributions for A_2. The deviations from SM distribution exhibit identical dependence on A_1 and A_2 when they are varied alone.

As the axial vector coupling F_A contributes with opposite signs to left and right-handed top-quark cross section[32], $t\overline{t}$ spin correlation is also altered by the non-standard couplings. To illustrate the effect on spin correlation, we follow the conventions of Mahlon and Parke[37] and use the off-diagonal basis to define the spin axis for the top (and antitop). We calculate the angle (θ) between a decay product of the W and the spin axis of the top quark in the top-quark rest frame, and the angle ($\overline{\theta}$) between a decay product of the W^- and the spin axis of the antitop in the antitop rest frame. For the decay product we use either the down-type quark (d,s) or the charged lepton. Figures 1.4 and 1.5 show the distribution of cosθ vs cos$\overline{\theta}$ for different A_1 and A_2 values. The deviation from SM exhibits identical dependence on A_1 and -A_2.

Finally, we also note that the couplings change the $t\overline{t}$ production cross section σ, as shown in Fig. 1.6. Again, the dependence on A_1 and A_2 is very similar.

As we noticed, the effect of varying A_1 is similar to that of varying A_2, and therefore the sensitivity to either parameter should be comparable, and study of either one would yield similar results. We choose to focus on A_2, with both A_1 and A_3 set to 0 (SM value).

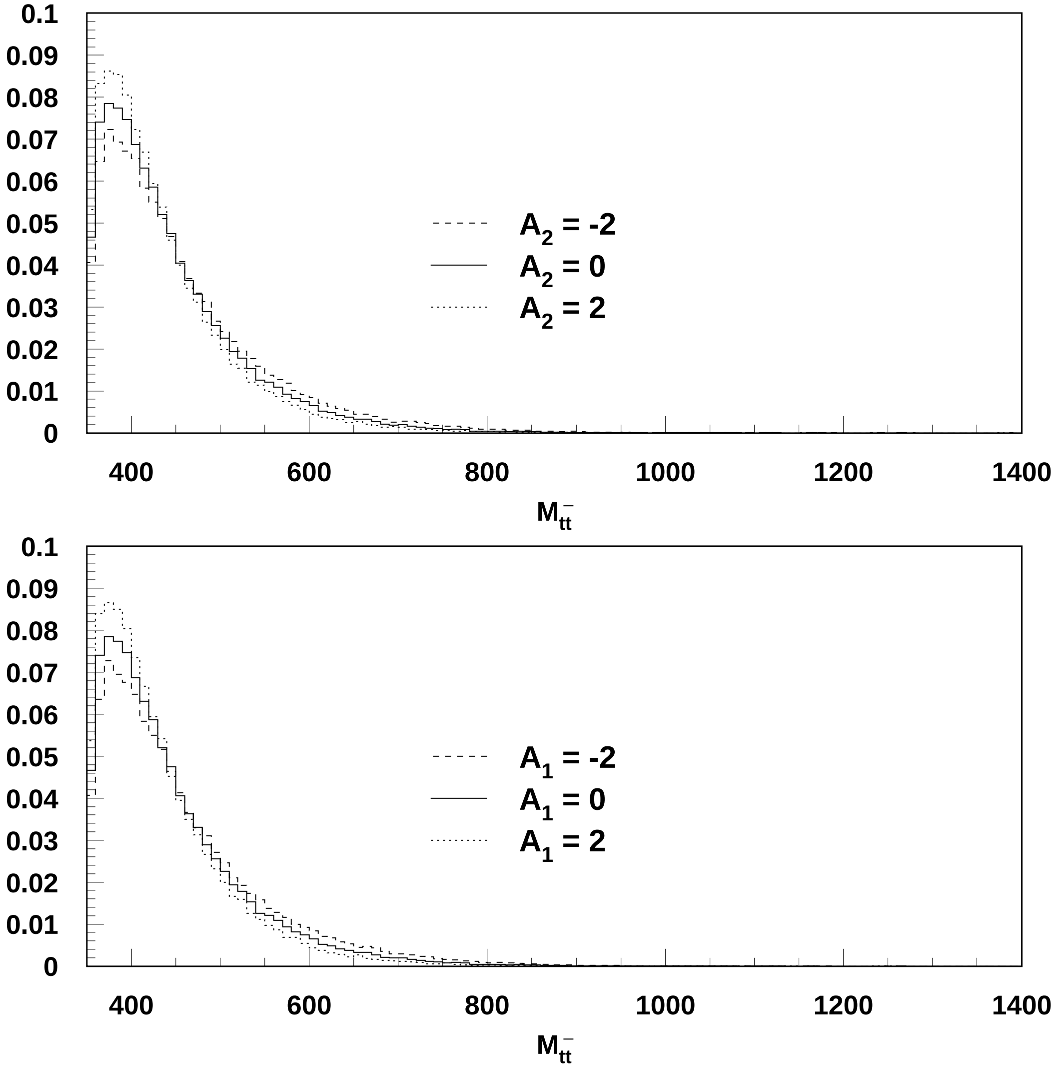

Figure 1.3: $t\bar{t}$ invariant mass distribution for (a) A_1, $A_3 = 0$, and (b) A_2, $A_3 = 0$

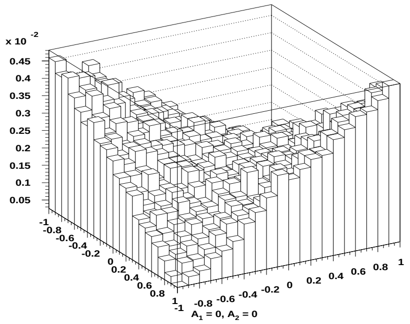

Figure 1.4: Lego plot of cosθ vs cos$\overline{\theta}$ for SM $t\bar{t}$ events

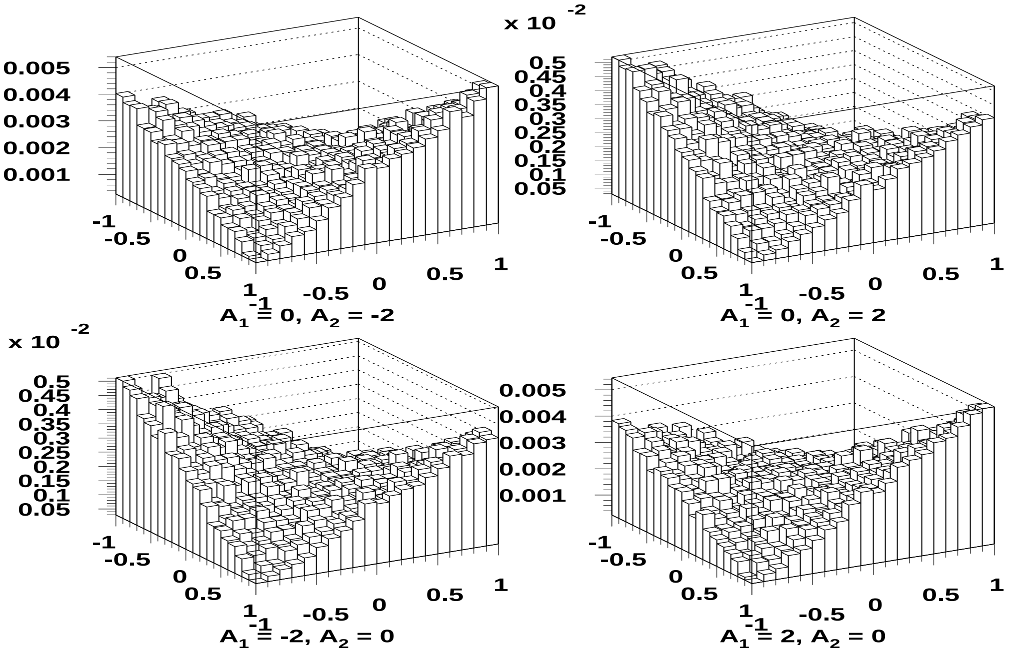

Figure 1.5: Lego plot of cosθ vs cos$\overline{\theta}$ for various A_1 and A_2 values.

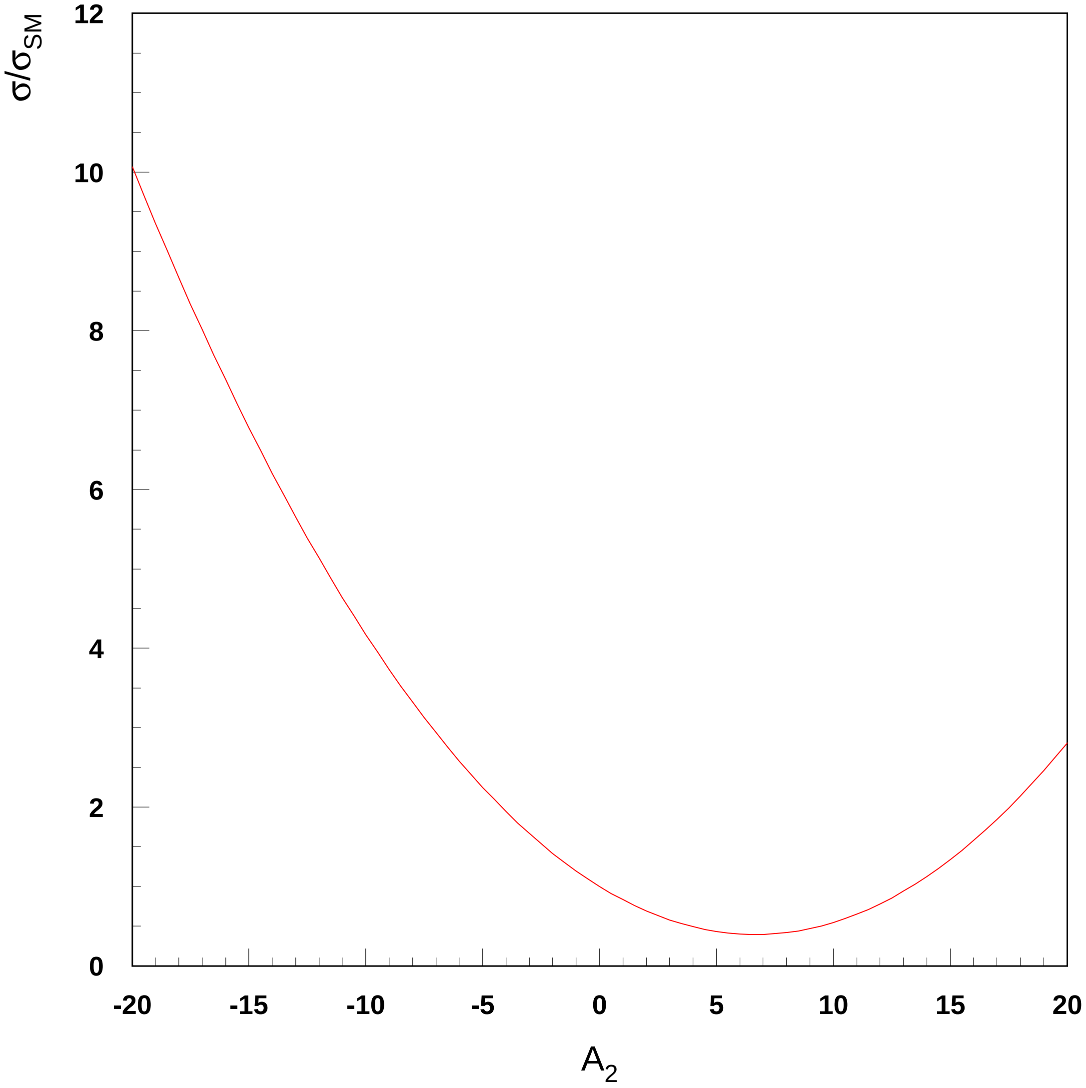

Figure 1.6: Ratio of $t\bar{t}$ cross section relative to that of the SM as a function of A_2, with A_1, $A_3 = 0$.

Chapter 2

The Experimental Apparatus

The data for this analysis were produced at the Fermilab Tevatron proton-antiproton collider and collected using the DØ detector, during the 'Run I' operation period from 1992 to 1996. Another active data collecting period (Run II) is now underway after improvements were made to various elements of the accelerator and detector. This chapter describes the essential components of the accelerator and the DØ detector in Run I. More detailed descriptions can be found in Ref. [38, 39, 40, 41, 42].

2.1 The Tevatron

Located in the Batavia suburb of Chicago, Illinois, the Fermilab Tevatron was the first and remains the only collider in the world that can produce collisions at a sufficiently high center-of-mass energy for producing top quarks. In Run I, protons and antiprotons beams were collided at a center-of-mass energy of 1.8 TeV. This energy was increased to 1.96 TeV in Run II. To attain the high energy, the particles go through several stages of accelerations. Each stage is specifically designed to achieve its final beam energy. Fig. 2.1 shows a schematic of the Fermilab accelerator complex in Run I.

H^- ions are first produced by injecting hydrogen into an H^- ion source under high pressure, and then extracted and injected into the Cockcroft-Walton accelerator where they are accelerated to 750 keV by applying a series of potential differences to the ions. The beams from the Cockcroft-Walton accelerator are created as pulses since there is a time lag between each series of acceleration.

The Linac is a linear accelerator approximately 150m long. H^- ions from the Cockcroft-Walton accelerator are sent to the Linac where they are boosted to an energy of 400 MeV. At the end of the Linac the H^- are sent through a carbon foil which strips off electrons, leaving only protons, which are then sent to the Booster synchrotron ring.

The Booster is a synchrotron where the protons are confined in a circular orbit with bending magnets while being accelerated by synchronized RF cavities. As the particle energy increases, the magnetic field in the bending magnets must also be increased accordingly in order to keep the beams in a closed orbit. The protons are accelerated to an energy of 8 GeV in the Booster and are then sent to the Main Ring.

The Main Ring is a synchrotron ring with a radius of about 1 km. Protons are accelerated to an energy of 150 GeV before they are either sent to the Tevatron ring or directed to a target hall to produce antiprotons.

To produce antiprotons, the 150 GeV protons from the Main Ring are sent to a cylindrical Nickel/Copper target. The collision produces about 20 antiproton for every million protons. The antiprotons of different energies are then 'focused' by a lithium lens, which is a cylinder of liquid lithium with a focusing magnetic field. Following the lens, a pulsed dipole magnet selects antiprotons with an energy of 8 GeV and sends them to the antiproton storage ring, known as the Debuncher.

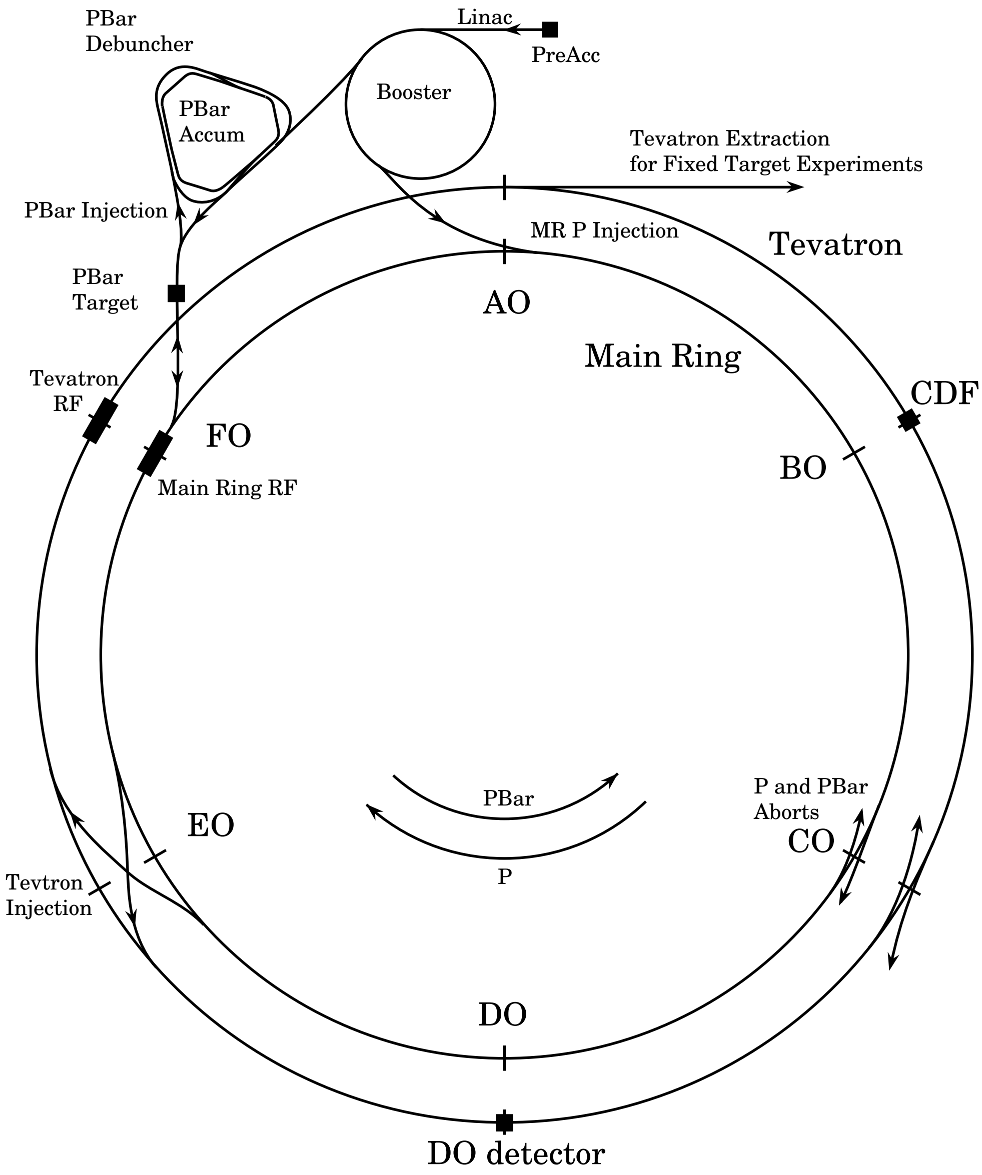

Figure 2.1: Schematic of the Fermilab accelerator complex.

Initially, the antiprotons have a large spread in momentum. The Debuncher uses two processes to reduce this spread. The first process, known as debunching, uses radio frequency techniques to smooth the antiproton bunch into a uniform continuous ring, where all the particles have approximately the same momentum. The second process, known as stochastic cooling [43, 44], improves the roundness of the circular orbit by measuring the trajectory of a collection of particles relative to the desired orbit, and sends correction signals to kicker electrodes to adjust the path of any particle whose orbits are not ideal. The antiprotons are kept in the Debuncher until just before the arrival of the next pulse (about 2.4 s later), when they are transferred to the Accumulator.

The Accumulator is a storage ring that resides in the same tunnel as the Debuncher. It provides further cooling to the antiproton beam and increases the density by a factor of about one million. After about four to six hours, when enough of them have been accumulated, the 8 GeV antiprotons are injected into the Main Ring and accelerated to 150 GeV.

The Tevatron is a synchrotron with super-conducting magnets that produce a strong magnetic field of close to 4.0 Tesla (at highest beam energy). It is housed in the same tunnel as the Main Ring and provides the final stage of acceleration to the particle beams. In the collider mode, six bunches of protons and six bunches of antiprotons of 150 GeV from the Main Ring, traveling in opposite directions, are injected into the Tevatron ring, where they are accelerated to the highest achievable energy (900 GeV in Run I). Once at full energy, the beams are made to collide at two beam crossing points B0 (CDF) and DØ. The beams are typically kept colliding for about 10-20 hours, after which time the machine is emptied and refilled with new batches of protons and antiprotons.

2.2 The DØ Detector.

To detect and study the many types of particle produced by $p\overline{p}$ collisions, different detection techniques and equipment are needed. The DØ detector[42] is a sophisticated, multipurpose detector that allows the identification of different objects like electrons, muons, jets and neutrinos simultaneously with high precision and at high rates. It is built around one of the $p\overline{p}$ interaction points to provide maximum detection coverage. The entire detector measures around $13 \times 11 \times 17 m^3$ and weighs close to 5,500 tons. There are three major detector components: the central tracker, the calorimeter, and the muon system, laid out and integrated in a way that maximize their detection capabilities. Figure 2.2 shows a schematic of the DØ detector.

2.2.1 Coordinate System

The coordinate system used by DØ follows the right-hand rule, with the z-axis, which runs along the beamline, pointing towards the direction of the circulating protons and the y-axis pointing upward. The center of the detector defines the origin. As the calorimeter and tracker are in the shape of a cylinder, it is natural to use the cylindrical coordinates, with polar angle θ and azimuthal angle ϕ. A quantity called pseudorapidity η $(= -\ln(\tan\frac{\theta}{2}))$ is commonly used in place of the polar angle in particle physics since it is a good approximation to the true rapidity $y = \frac{1}{2}\ln((E+p_z)/(E-p_z))$ at high energies. A differential interval in rapidity is also Lorentz invariant.

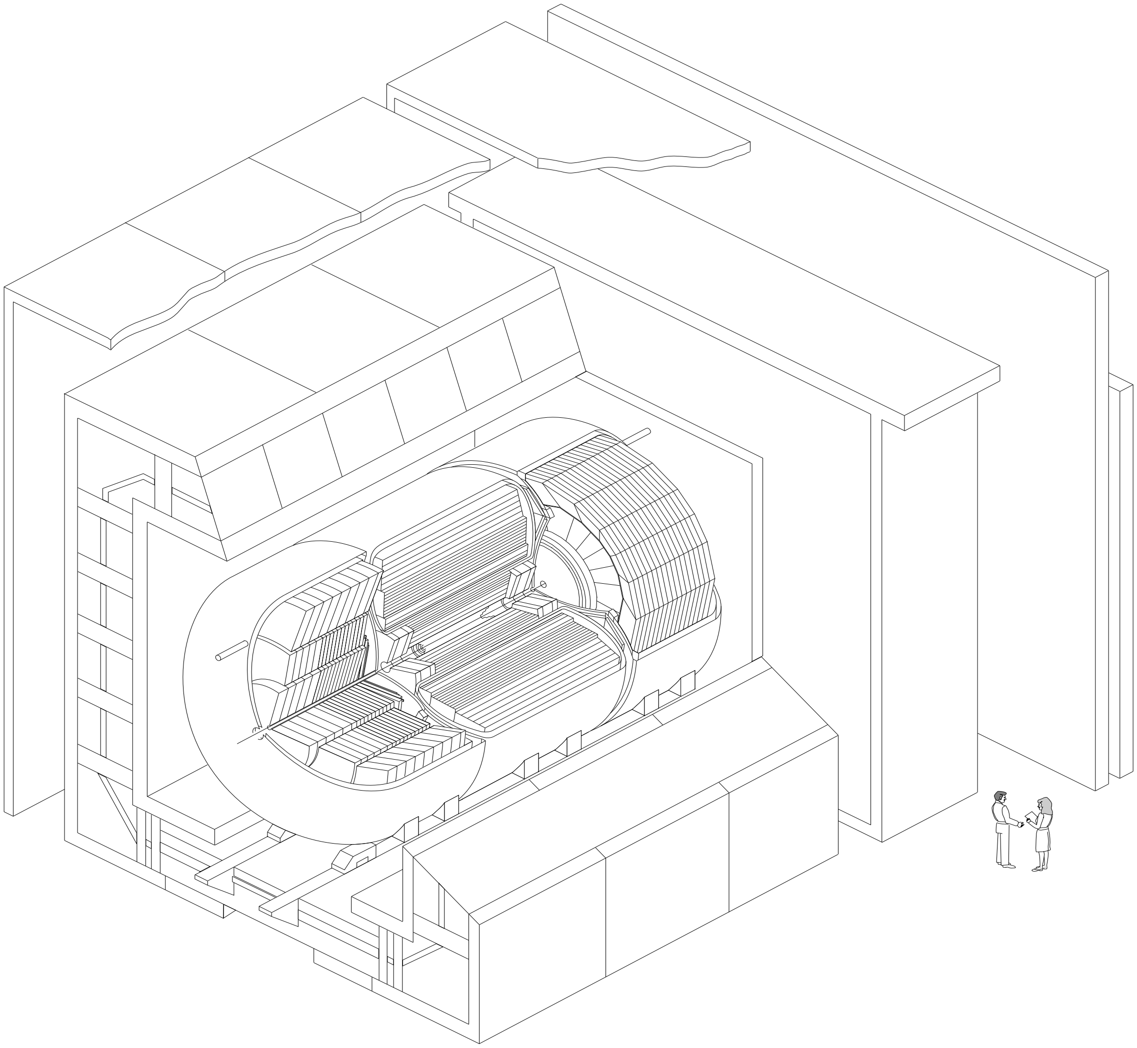

DØ Detector

Figure 2.2: Schematic of the DØ detector at the Tevatron.

2.3 The Central Tracker

The central tracking systems are used to detect the and measure paths of charged particles, which are used to locate the interaction coordinates (vertex) of an event and in identifying electrons. They also measure the ionization of charged particles to aid in distinguishing a single electron track from electron pairs coming from photon conversions ($\gamma \rightarrow e^+e^-$). In order to attain good vertex resolution, the tracking systems are placed in the innermost section of the detector, closest to the interaction region. The Run I tracker was based on the drift chamber technique, in which a voltage is applied through thin wires across a gas-filled enclosure. As the ionization created by a charged particle traversing the region drifts towards the thin wires, the large electric field close the the wires creates an avalanche of secondary ionization and a detectable signal. There was no magnetic field in the tracking region in Run I, therefore there was no momentum information from the charged tracks. The Central Tracker is comprised of three main tracking systems: the Vertex Chamber (VTX), the Transition Radiation Detector (TRD) and the Central Drift Chamber (CDC). The arrangement of the tracker is shown in Fig. 2.3.

2.3.1 Vertex Drift Chamber (VTX).

The Vertex Chamber[48] occupies the innermost layers of the central tracker, wrapping around the beam pipe and extending from a radius of 3.7 cm to 16.2 cm, with a length of about 97 cm. It consists of three concentric layers of cells, each containing eight sense wires running parallel to the beamline, to measure the r-ϕ coordinates of a track. The sense wires are kept at an electric potential of 2.5keV, The innermost layer has 16 cells in azimuth, and the outer two have 32 cells each. The z-coordinate is determined by comparing the sizes of signals read out at both ends of the sense

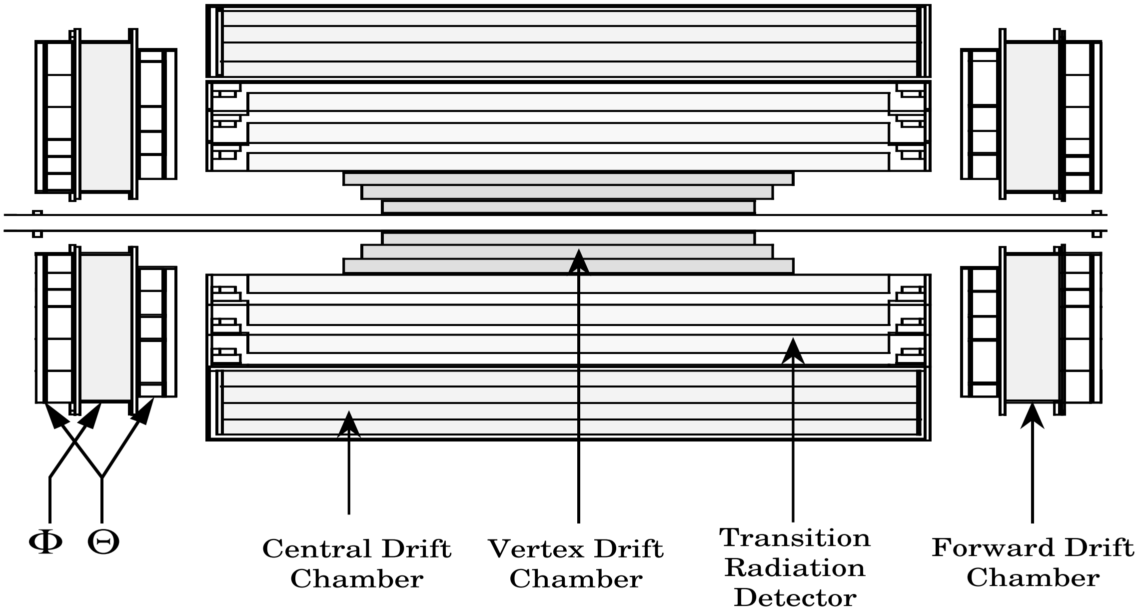

Figure 2.3: Schematic of the DØ central tracker.

wires, which have a resistivity of 1.8 kΩ/m. The gas used in the VTX is $CO_2(95\%)$, ethane (5%), and $H_2O(5\%)$. The resolution achieved along $r\delta\phi$ is $\approx 60\mu$m and ≈ 1.5 cm in z.

2.3.2 Transition Radiation Detector (TRD).

The Transition Radiation Detector [51] is located between the VTX and the CDC. It provides a different kind of electron detection technique that supplements the information from the drift chambers and the calorimeter. When highly relativistic charged particles ($\gamma = E/m > 10^3$) traverse boundaries between media of different dielectric constants, transition-radiation X-rays are produced. Since electrons are many times lighter than hadrons, measuring these radiation can help distinguish true electrons from charged hadrons.

The TRD consists of three concentric, nitrogen gas-filled cylinders, each containing 393 layers of 18μ m thick polypropylene foil to induce radiation from charged particles. Immediately behind them and separated by a mylar window, is a section filled with a mixture of $Xe(91\%)$, $CH_4(7\%)$ and C_2H_6. Here the X-rays create ionization, which drifts towards sense wires running parallel to the z-axis. The magnitude and timing of the signals will then provide information on the type of particle that produced the radiation.

2.3.3 Central Drift Chamber (CDC).

The Central Drift Chamber [49] is the outermost section of the central tracker. It extends from a radius of 49.5 cm to 74.5 cm, with a length of 184 cm. It consists of 4 concentric cylinders, each with 32 azimuthal cells. Inside each cell are seven sense wires and two delay lines running along the length of the chamber. The sense wires are only read out at one end to provided r-ϕ measurement, while the delay lines, located just inside the first wire and outside the last wire, are read out at both ends to provide z measurement. The ionization medium is a mixture of argon(92.5%), methane(4%), $CO_2(3\%)$, and $H_2O(0.5\%)$. The $r\delta\phi$ resolution achieved is $\cong$ 180 μm, and about 3 mm in z

2.3.4 Forward Drift Chambers (FDC).

The Forward Drift Chambers [50] are located at either end of the concentric barrels of the VTX, TRD, and CDC, and just before the inner walls of the end calorimeters. They extend the coverage for charge-particle tracking down to $\theta = 5^o$. Each FDC package consists of three separate chambers, as shown in Figure 2.4. The Φ module has radial sense wires used to measure the ϕ coordinate. It is sandwiched between

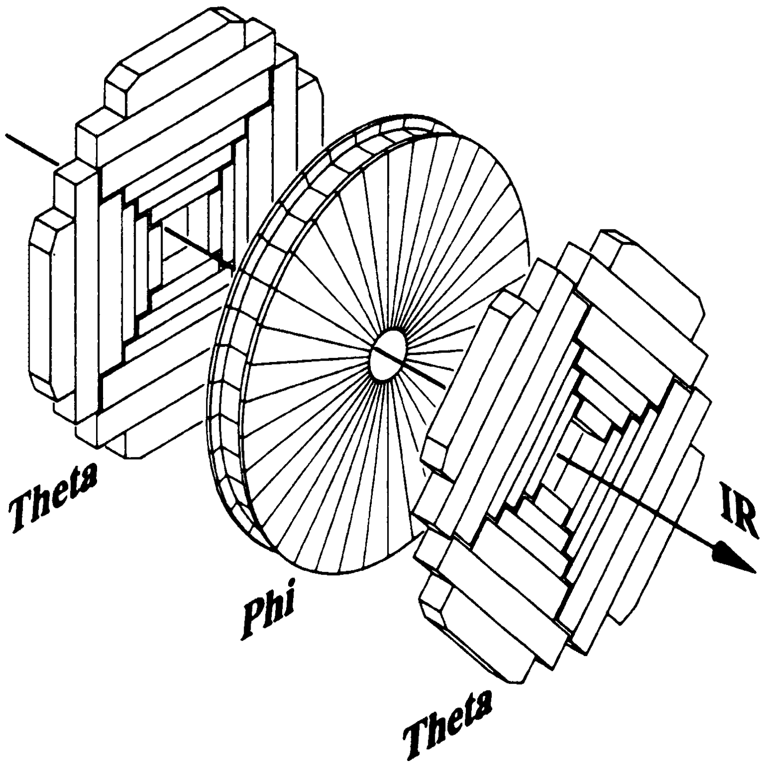

Figure 2.4: Schematic of the FDC. Two Θ modules with a Φ module in between.

a pair of Θ modules, whose sense wires determine the θ coordinate. The geometry of the FDC is more complicated than that of the CDC, but the operating principle is similar, and the chamber gas is the same. The position resolution is about 200 μm in $r\delta\phi$ and 300 μm in $r\delta\theta$.

2.4 The Calorimeter.

The calorimeter is the primary information gathering device for many of the particles (electrons, photons and jets). It serves three important functions: to capture and measure all the energy of these particles, to measure the location of the energy shower, and record the pattern of energy deposition to aid particle identification.

The DØ calorimeter [42] design is based on the sampling detector technique [52]. The basic structure is layers of dense, energy absorbing materials (absorbers) sandwiched between sensitive (active) medium, where the energy of a particle is sampled and measured. The sampled energy is then converted to the total incident energy through proper calibration. This ensure good containment of shower energy within the calorimeter, while allowing precise measurement of energy and energy profile of the shower. The absorbers used by DØ are made of depleted uranium and copper, and the active medium of choice is liquid argon.

The energy deposited by particles usually spread out over a finite volume in the calorimeter due to the production of secondary particles. As a result it is common to refer them as energy showers, both to indicate the extent and dynamics of the deposition. Electromagnetic showers induced by electrons and photons are typically different from those by hadrons.

At high energy, an electron mainly loses its energy through bremsstrahlung. These radiations (photons) in turn create secondary e^+e^- pairs. This results in a cascade of electrons and positrons traveling through the calorimeter. As the energy of the particles decrease, it reaches a critical value below which ionization becomes the main source of energy loss and pair production, together with the shower, subside, until all energy is dissipated through ionization and excitation. The longitudinal development of electromagnetic showers in a medium is characterized by the radiation length (X_0), which is the mean distance over which a high energy electron loses all but 1/e of its energy through bremsstrahlung, and, has the empirical form:

$$X_0 \approx \frac{716.4A}{Z(Z+1)\ln(287/\sqrt{Z})}\mathrm{g/cm}^2 \tag{2.1}$$

where Z and A are, respectively, the atomic number and the atomic weight of that medium. The transverse dimension of the shower is approximated by the Moliere radius $R_M = X_0 E_s / E_c$ where $E_s = 21$ MeV, and E_c is the critical energy defined as the energy at which the ionization loss per radiation length is equal to the electron energy [53].

Hadrons lose energy mainly through inelastic interactions with the nuclei, which typically have a lower probability of occurrence than EM interactions. As a result hadron showers tend to spread over a larger volume and thicker absorbers are required to contain them. The shower develops by creation of additional hadrons in the nuclear interactions, which cascade until the energy of the hadrons are simply absorbed by nuclei or dissipated through ionization. The typical length scale for hadronic shower development in a medium is the nuclear interaction mean free path (also called absorption length), empirically given by:

$$\lambda \approx 35 A^{\frac{1}{3}} \text{ g/cm}^2 \quad , \tag{2.2}$$

where A is the atomic weight of the medium. The longitudinal shower development reaches a maximum at about a depth of $(0.2 \ln E + 0.7)\lambda$ where E is the energy of the incident particle in GeV, with a gradual energy loss afterwards. The transverse dimension shows a similar profile, with most energy contained within 1λ. Part of a hadron shower can also contain neutral pions (π^0), which decay to two photons, and deposit their energy as electromagnetic showers. Therefore it is important to have even response for EM and hadronic shower. Response for hadronic shower tends to be lower because most of the energy loss occurs in nuclear excitations and breakup which may not translate into measurable ionizing energy. For this reason, uranium has an added advantage as absorber since some of the interactions will induce fission of uranium nuclei and produce energy that can be detected.

The DØ calorimeter is a combination of three calorimeters: the central calorimeter (CC) and two end calorimeters (EC), each housed in a separate cryostat maintained at liquid argon temperature. To help distinguish EM showers from hadronic showers, each calorimeter is divided into three sections. The electromagnetic section (EM) is closest to the interaction point, with the fine hadronic (FH) immediately behind it and coarse hadronic (CH) section occupying the outermost region. These sections are further subdivided in ϕ, depths(layers), and z(r) in CC(EC). The division in z or r are designed such that these subdivisions, or readout cells, can also be grouped into pseudo-projective towers, which are approximately aligned with the directions of particles coming from near the center of the detector. The term pseudo-projective refers to the fact that the centers of cells in each tower lie on rays projecting from the center of interaction region, but not the cell boundaries. The EM modules have four layers, with the third layer located at a depth (in radiation length) near the maximum of a typical EM shower, and twice as finely segmented in η and ϕ to give more precise measurement of the shower profile. The FH modules have 3 or 4 layers, while the CH have 1 or 3 layers. The typical size of a tower is about $\Delta\eta = 0.1$ and $\Delta\phi = 2\pi/64 \approx 0.1$.

2.4.1 Unit Cell

A readout cell typically consists of a number of unit cells, at approximately the same η and ϕ, connected together. Each unit cell, shown in fig. 2.6, is a pair of absorber plate and signal board, which are made by laminating two 0.5mm thick G-10 plates, with high resistive epoxy coating on the outside. During operation, an electric field is maintained between the two by connecting the resistive surface of

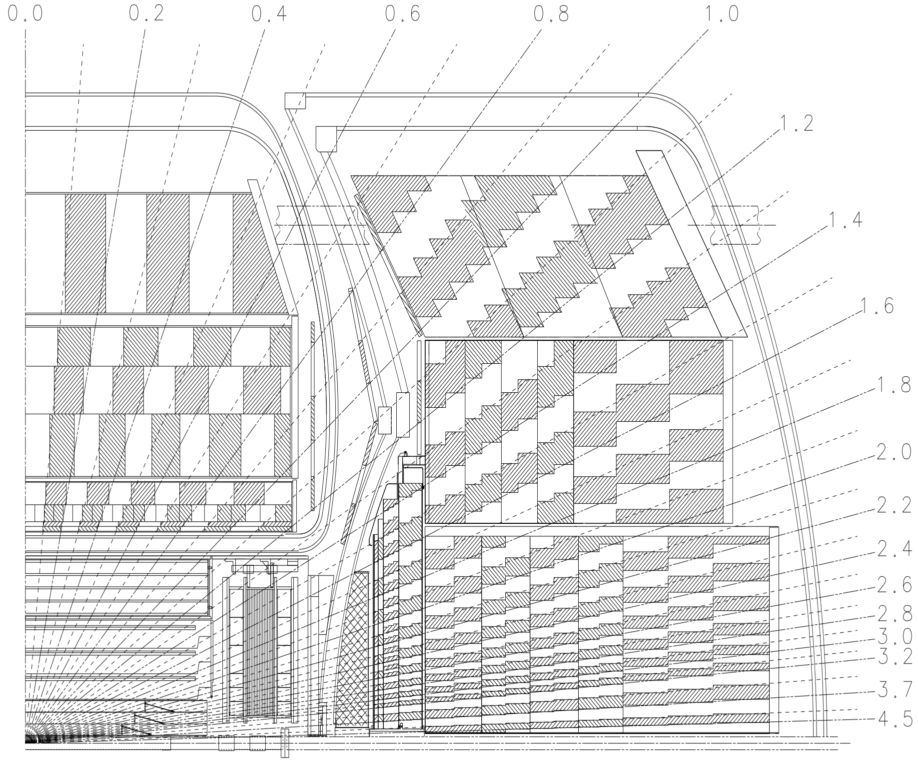

Figure 2.5: Side view of the DØ calorimeters. Rays of fixed η relative to the center of the detector are given in the sketch.

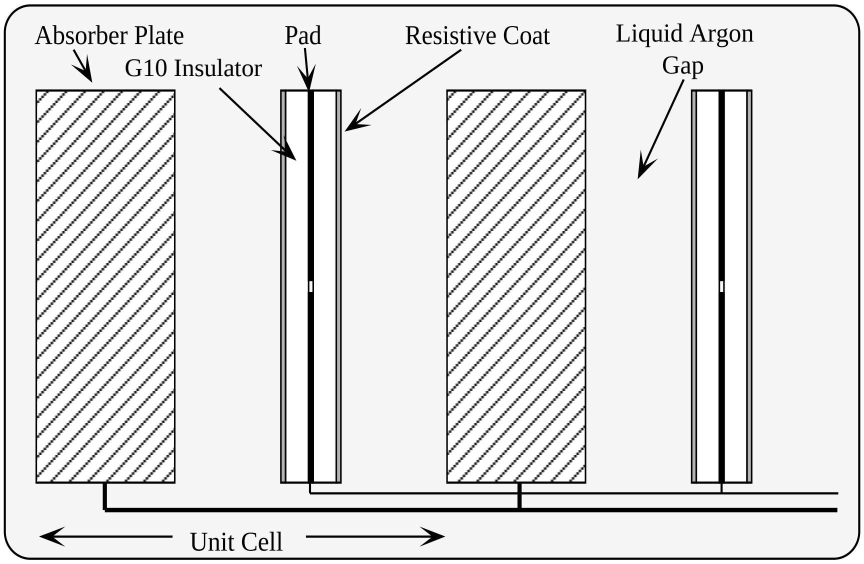

Figure 2.6: Unit cell in the DØ calorimeter.

the signal board to positive high voltage (2.0-2.5 kV), while grounding the absorber plate. The electron drift time across a 2.3 mm Argon gap is ≈ 450 nsec.

2.4.2 Central Calorimeter

The central calorimeter (CC) contains readout cells up to pseudorapidity of $|\eta| \leq 1.2$. The EM, FH and CH sections are 3 concentric cylinders. Absorber in the EM section are 3 mm thick nearly pure depleted uranium plates, while those in the FH are 6 mm thick made of uranium and niobium(2%). Copper plates of 46.5 mm are used in the CH. The four EM layers are of approximately 2.0, 2.0, 6.8. and 9.8 X_0, respectively, and a total of about 0.76 λ. The FH contains three layers of around 1.3, 1.0 and 0.9 λ, while the CH contains one layer of 3.2 λ.

There are 32 EM modules and 16 FH and CH modules in ϕ, each consists of 2 or 4 readout cells. There are no readout components in the gaps (informally known as "cracks") between these modules, therefore the three cylinders are rotated relative to each other to create a ϕ offset and prevent the gaps from lining up.

2.4.3 End Calorimeter

The end calorimeter contains readout cells up to $|\eta| \leq 4.2$. The fine and coarse hadronic sections behind the EM calorimeter are together called the inner hadronic (IH) section. The EM contains 4 mm while the fine hadronic section of IH contains 6mm thick absorber plates, each made of the same material as their CC counterparts. The coarse hadronic section of the IH contains 46.5 mm steel plates. The four EM layers are of 0.3, 2.6, 7.9, 9.3 X_0, respectively, with the material of the cryostat serving as additional absorber. The IH consists of 4 layers (1.1 λ each) in the fine hadronic and 1 layer (4.1 λ) in the coarse hadronic section. Outside the EM and IH, which extends approximately up to the outer radius of the central tracker, there are additional concentric rings of detectors, called the middle (MH) and outer (OH) hadronic sections, which provide additional hadronic energy measurement coverage up to the outer radius of the central calorimeter.

2.4.4 Calorimeter performance

The resolutions of energy measurement by the calorimeter were studied by an early test-beam run[54, 55], in which electron and pion beams of known energy (between 10 and 150 GeV) were used. The parametrized resolution are found to be: [54, 55]:

$$\frac{\sigma(E)}{E} = \frac{16\%}{\sqrt{E(GeV)}} \oplus 0.3\% \quad \text{for electrons and} \tag{2.3}$$

$$\frac{\sigma(E)}{E} = \frac{41\%}{\sqrt{E(GeV)}} \oplus 3.2\% \quad \text{for pions.} \tag{2.4}$$

where $\sigma(E)$ is the resolution as a function of energy E, and $\oplus$ means to be added in quadrature.

2.5 Muon System

Most muons produced at the Tevatron pass through the calorimeter with little interaction since they do not have high enough energy to radiate substantially and they do not interact with nuclei through strong interaction. To detect them is the main purpose of the muon system.

The muon system consists of a set of five magnetized iron toroids positioned outside and surrounding the calorimeter. Layers of proportional drift tubes (PDT's), each with a single 50μm gold plated tungsten sense wire, are put on both sides of the toroids to detect and measure the passage location of a muon. The change in direction of the muon before and after passing through the magnetic field inside the toroids thus provide a measurement of its energy. There is little need to distinguish the signal between different particle types since muons are the only SM particle (besides neutrinos) that can easily escape the calorimeter. There are however cosmic muons which can mimic Tevatron produced muons. Therefore vertex, tracking and possibly calorimeter information are used for better identification at a later stage.

The Wide-Angle Muon System (WAMUS) covers the region up to $|\eta| \leq 2.5$. It consists of a central toroid (CF) and two end toroids (EFs). Most of the η range is covered by three layers (chambers) of PDTs. The first (A) layer is attached to the surface on interaction side of the toroid, the second (B) layer on the outside surface of the toroid, while the third (C) layer sits about 1-3 m further out after an air gap. There are four layers of PDT in the A layer and three in the B, C layers. The B and C layers together give an outgoing position and direction resolution of 0.17 mm

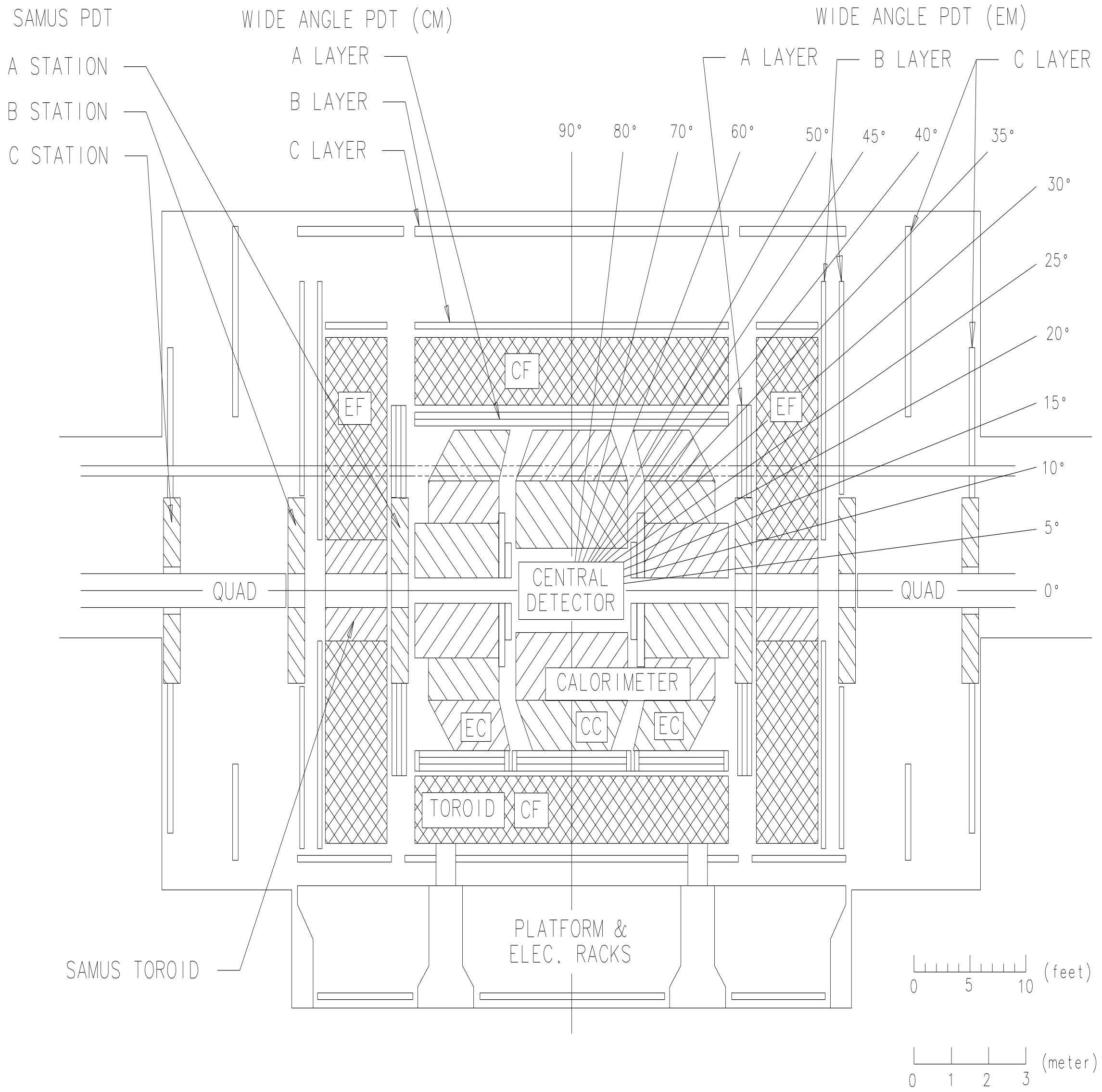

Figure 2.7: Muon System in the DØ detector.

and 0.2 mrad. The Muon System is shown in Figure 2.7.

The Small Angle Muon System (SAMUS) covers the region of $1.7 < |\eta| < 3.6$. It consists of two toroids located in the central hole of the WAMUS end toroids, and cover $2.5 < |\eta| < 3.6$. Similar to WAMUS, The PDTs, each with a single sense wire, are arranged into 3 layers, with one on the interaction side and two on the outer side. Each layer consists of three planes of PDTs, which are oriented in different directions on the planes to reduce ambiguities in hit location. There are two staggered subplanes for each plane.

The resolution of the muon momentum measurement is limited largely by multiple coulomb scattering in the toroids and by the hit-position resolution in the drift chambers. The resolution was determined by comparing $Z \to \mu^+\mu^-$ data with similar Monte Carlo events where the resolution was degraded until the width of the $\mu^+\mu^-$ invariant mass for the Z matched that observed in the data. The resolution is approximately Gaussian in $1/p$, and can be parameterized as [56, 57]:

$$\delta(\frac{1}{p}) = \frac{0.18(p-2)}{p^2} \oplus 0.003 \quad , \tag{2.5}$$

where p is the momentum in GeV.

2.6 Trigger System

Events produced from the $p\overline{p}$ collisions are immediately filtered through a complex multi-stage trigger system and only those of interest are selected for offline reconstruction. The decision to select (trigger) an event is based on the information processed, in real time, at each stage. In Run I, the nominal time interval between beam/bunch crossings is 3.5 μs, corresponding to a frequency of about 286 kHz. At a typical luminosity of $L = 5 \times 10^{30} cm^2 s^{-1}$, there is about one $p\overline{p}$ collision per crossing. This enormous event rate is first reduced by the Level 0 trigger system, which makes the fastest decision, to about 150 kHz. This is followed by the Level 1 and 1.5 triggers which are mainly hardware-based and the more sophisticated software-based Level 2 triggers. The Level 1 triggers reduces the event rate to about 800 Hz and Level 1.5 reduces the rate to under 100 Hz. The Level 2 triggers, with dedicated algorithms to analyze the information from all Level 0, 1 and 1.5, selects events at a rate of about 2 Hz. The layout of the DØ trigger system is shown in Fig. 2.8

2.6.1 Level 0 Trigger

The Level-0 trigger system is a set of scintillating detectors situated on the surfaces of the end calorimeters close to the beam pipe ($1.9 < |\eta| < 4.3$) [58]. It registers the occurrence of non-diffractive inelastic $p\overline{p}$ collision (beam-beam events, as opposed to beam-gas events) by identifying simultaneous activities (coincidences) in the forward and backward regions. The signal arrival times at the two ends provide a measure of the z-position of the interaction point (z_{vtx}). A fast estimation of z_{vtx} with resolution of ± 15cm is available about 800ns after a collision and passed to Level 1 for calculation of transverse energies. A more precise estimation, which includes calibration corrections and has a resolution of ± 3.5cm, is available within 2.1 μs for use in Level 2.

2.6.2 Level 1 Trigger

The Level 1 trigger system utilizes information from Level 0, the calorimeter and the muon system to determine, usually within the 3.5 μs between beam crossings (otherwise the processing of the next event may not be able to take place, resulting

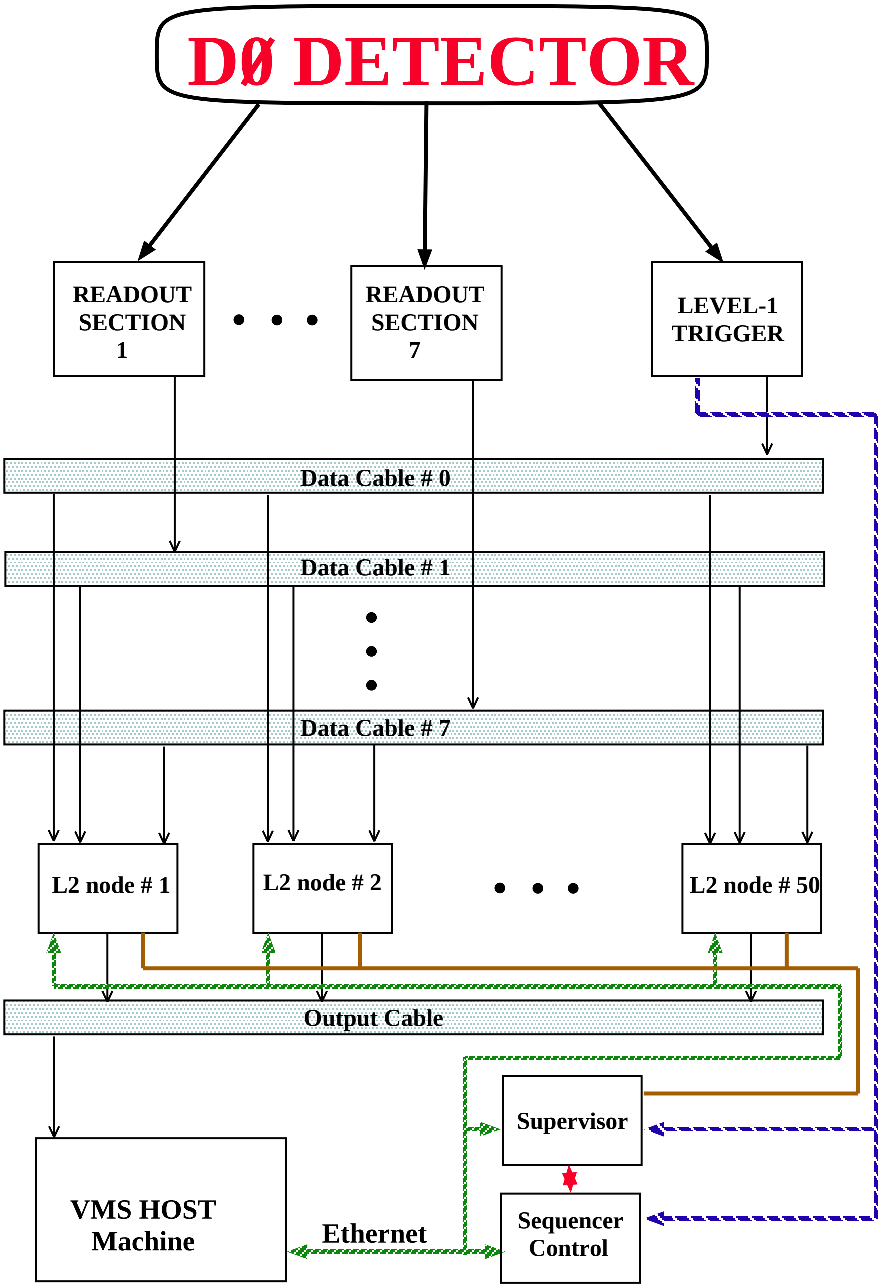

Figure 2.8: Schematic view of the DØ DAQ/Trigger systems.

in “deadtime”), whether to accept an event [59]. The calorimeter at this stage is segmented into trigger towers with a size of $\Delta\eta \times \Delta\phi = 0.2 \times 0.2$. A fast analog sum of cell energies in each trigger tower is performed to provide estimation of transverse energy deposited in both the electromagnetic and hadronic sections of that tower. This information is digitized before being input to Level 1 calorimeter triggers. For the muon system, PDTs on each (A, B or C) layer that have a hit are matched (among layers) to form track candidates. The muon triggers look for track candidates with hit pattern consistent with a muon coming from the nominal interaction vertex. These detector-specific triggers, along with all other necessary information, are collected and processed by the Level 1 trigger framework [60], where each event is compared to pre-determined sets of event characteristics, such as number of trigger towers above certain transverse energy threshold. Events that meet the requirements of any of the sets are passed on for further processing.

2.6.3 Level 1.5

Information from Level 1 is refined at Level 1.5 through fast clustering of calorimeter trigger towers and finer matching of layer hits in the muon system. This provide additional criteria for identifying events of interest.

2.6.4 Level 2

The Level 2 trigger system [62] consists of a set of software filters running on the complete data of an event. Information of an event is digitized before input to Level 2. Since event rate is reduced by the Level 0 and Level 1/1.5 triggers, more sophisticated (yet still relatively fast) algorithms are used to reconstruct objects such as electrons, muons and jets. Events selected by Level 2, which usually have a data size of 0.5 Mbyte, are written to magnetic tapes for offline reconstruction and permanent storage.

The triggers used to select the $t\bar{t}$ event candidates in this analysis can be found in Ref. [73].

Chapter 3

Event Reconstruction

Once an event passes the requirements of the trigger systems, all information necessary for offline reconstruction is written to tape. The information include ADC (Analog-to-Digital Converter) counts from the calorimeter, TDC (Time-to-Digital Converter) counts from the drift chamber and analog and digital signals from the muon system. These 'raw' signals are then further processed by the DØRECO event reconstruction program to identify the various physics objects, such as leptons, photons and jets, in the event. In this chapter we describe the reconstruction and identification of leptons and jets, which are used in this analysis. A more detailed description of the DØRECO program can be found in [63]

The reconstruction process can be divided in two stages:

3.1 Detector reconstruction.

Information in each detector is first analyzed and converted to elementary objects that can be used for particle identification. Signals from the sense wires in the tracking chamber are processed to indicate the spatial positions where the signal originated. These coordinates, or 'hits', are then matched to form the trajectory of tracks. For the calorimeter, ADC counts for each calorimeter cell is converted into energy deposition. These cells are also grouped in η to form towers, which will be used in the clustering process for particle identification.

3.2 Particle Identification.

3.2.1 Electrons

Electrons are characterized by a localized deposition of energy in the electromagnetic section of the calorimeter, with a matching track pointing back to the interaction vertex. The identification process starts with the clustering of towers using the nearest neighbor algorithm. With the highest E_T tower in an event as a seed, all neighboring towers with E_T above 50 MeV are grouped together to form a cluster. The highest E_T tower in the remaining towers will then become the next seed. This process is repeated until no tower can be used as a seed.

Energy clusters with more than 90% of its energy in the EM layers of the calorimeter and more than 40% in a single tower is identified as an electron or photon candidate. This removes most hadronic jets while retaining more than 99% of true electrons and photons. Electron candidates are distinguished from the photon candidates by the presence of CDC or FDC track within a $\Delta\eta\Delta\phi$ window of 0.1 x 0.1.

There are two main processes that contribute to the background in electron identification: π^0 decay and photon conversion. A π^0 decays primarily to two photons, producing an electromagnetic cluster that can be randomly matched to tracks from low-energy charged hadrons. Photon conversion early in the tracking system creates e^+e^- pairs that can be close to each other in direction of travel and, without a magnetic field, continue so through the tracking medium. This may therefore be misidentified as a single track with a single matching electromagnetic shower. In order to further suppress these and other backgrounds, while retaining high efficiency for genuine electrons, many quality criteria were developed which individual analyses can apply to suit their specific event details. Here we discuss the additional selection criteria used in this analysis:

- Shower isolation

  Since most electron clusters are contained in the electromagnetic layers within a cone of radius R = $\sqrt{(\delta\phi)^2 + (\delta\eta)^2} = 0.2$ from the cluster center, the isolation fraction is defined as:

  $$f_{iso} = \frac{E(0.4) - EM(0.2)}{EM(0.2)} \tag{3.1}$$

  where E(0.4) is the total cluster energy in a cone of R = 0.4, and EM(0.2) is the electromagnetic energy in a core concentric cone of R = 0.2. An electron from a W decay should usually not be close to any other objects in the event, therefore corresponds to a small isolation fraction. For our analysis, a F_{iso} <0.1 is required. This retains most of the true electrons, while significantly suppressing the backgrounds from pi^0 decays (which are usually associated with a jet) with random track matches and semileptonic decays of b or c quarks (which produce electrons within or close to a jet).

- Shower Shape

  Within the electromagnetic layers, the pattern of energy deposition by an electromagnetic object (electron or photons) is generally different from other particles. This pattern can be characterized by the longitudinal and transverse profile of the shower, i.e, fraction of energy deposited in each layer or cell inside the cluster. These fraction are correlated. For example, an electron that deposits large amount of energy in the first layer will deposit less in the other layers. To take into account the correlations, a 41 variable covariance matrix was developed [64, 65]. The variables consist of fractional energies in layers 1,2, and 4 of the EM calorimeter, the fractional energies in each cell of 6x6 array in EM3 centered on the most energetic tower in the cluster, the logarithm of the cluster energy, and the z-position of the interaction vertex. These matrices were computed for electrons from both the test beam data and Monte Carlo. For a sample of N electrons the covariance matrix is defined as:

$$M_{ij} = \frac{1}{N}\sum_{n=1}^{N}(x_i^n - \bar{x}_i)(x_j^n - \bar{x}_j) \tag{3.2}$$

where the x_i are the variables that define the shape. The matrix M is calculated individually for towers at different η, assuming symmetry in ϕ. In addition, reflection symmetry is assumed for positive and negative η regions of the detector, and so there are 37 distinct matrices.

With the matrices M, one can define a χ^2 that signifies the degree of agreement between an individual shower and that expected from an electron of that energy and η:

$$\chi^2 = \sum_{i,j=1}^{41}(x_i - \bar{x}_i)H_{ij}(x_j - \bar{x}_j) \tag{3.3}$$

where H is the inverse of M.

- Since an EM shower usually develops close to the trajectory of the originating particle, one way to reduce fake electrons coming from random matches of tracks is to require a good agreement between the direction of a track and the centroid of the shower. We defined this track match significance as:

$$\sigma_{TRK}(CC(EC)) = \sqrt{(\frac{\Delta\phi}{\delta_{\Delta\phi}})^2 + (\frac{\Delta z(r)}{\delta_{\Delta z(r)}})^2} \tag{3.4}$$

where Δx are the differences in coordinate between the centroid of the cluster and the point at which the trajectory extrapolates to the calorimeter, and $\delta_{\Delta x}$ is the resolution in the mismatch of the measurement. For this analysis, good electron candidates are defined as those with σ_{TRK} <5.

- Since DØ has no central magnetic field, the measured *track ionization* (dE/dx) is used to discriminate between prompt electrons and photon conversions. To reduce background from conversions, events with dE/dx >2 MIPs (minimum ionizing particle) are removed.

The $t\bar{t} \rightarrow e$+jets analysis also applies kinematic requirements of $E_T > 20$ GeV and $|\eta^{det}|$ <2 (where *det* refers to η defined relative to the center of the detector) for the electrons to further enhance signal purity. The final efficiency for identifying single isolated electrons with these selections is 72% in the CC and 43% in the EC, and is essentially independent of electron energy.

Electromagnetic Energy Calibration

The absolute electromagnetic energy scale was originally derived from test beam calibration data. However, due to the difference between the test-beam and the DØ setup, the calibration turns out to be slightly low, as indicated by the reconstructed mass of the Z boson, which is off from the value measured very accurately by LEP experiments [3]. Therefore for this analysis the measured electron energies are scaled up so that the Z mass peak in $Z \rightarrow e^+e^-$ events matches the LEP measurement. This correction is about 5% in the central calorimeter, and $1-2\%$ in the end calorimeter.

3.2.2 Muons

Muons are primarily identified as tracks in the muon systems. Hits are first matched within the A layer and the B and C layers to form track segments before and after the magnetic toroids. These track segments are then matched to form a muon track. If an outer segment has no matching inner segment, it is extrapolated to the mid-toroid plane, and a line connecting the intersection point and interaction vertex is used as the pre-toroid direction. The change in direction (bend angle) by the toroids, corrected for the energy lost in the calorimeter, is used to provide a first estimate of the muon momentum.

The main source of muon background comes from cosmic rays, which contain muons that leave tracks in the muon systems, and tracks that come from instrumental noise in the muon chamber. Using information from calorimeter and tracking system, one can reduce this background by requiring only tracks that are consistent with coming from a Tevatron $p\overline{p}$ collision. Some hadronic showers can also develop beyond the calorimeter (called punch through) and create muon-like activities in the muon chamber. However they are usually contained by the iron toroid, except in the gap between the central and end toroids.

There are several requirements that are imposed to identify true Tevatron-produced muons. Beside rejecting backgrounds, information from the calorimeter and tracking system can also help improve the resolution of muon momentum. The main requirements are as follows:

- Impact parameters. To ensure a muon track comes from near the interaction vertex, thus reducing cosmic ray backgrounds, two impact parameters of the track are calculated. The *non-bend impact paramter* is calculated by first projecting the track onto the x-y plane, where it does not bend, and extrapolating the track formed by the B and C layers towards the center of the detector. Any track with a non-bend impact parameter greater than 40 cm are rejected. The *bend-view impact parameter* is derived by projecting the track onto the plane where it bends and extrapolating the projection. Muon tracks are required to have a bend-view impact parameter of less than 25 cm.

- Track timing. As with impact parameters in spatial separation, another way to reduce cosmic ray backgrounds is to require that the track passes through the drift chamber close to the primary interaction in time. The time T_0, relative to the beam crossing, that minimizes the χ^2 of a track is required to be less than 100ns for it to be accepted.

- Cosmic Ray Veto. A muon track in the central region ($\eta^{det} < 1.0$) that is back-to-back with another track or large number of hits on the other side of the interaction vertex is consistent with a cosmic ray passing through the entire detector and is rejected.

- Hit multiplicity. A typical muon track contains hits in 7-10 drift tubes, depending on the particular region of the detector. For high p_T muon tracks in the end regions a minimum of 5 hits is required (there is no explicit requirement in the central region).

- Calorimeter confirmation. A muon that passes through the caloriemter typically deposits 1 to 3 GeV of energy through ionization. This energy loss is estimated using Monte Carlo and added back to the measured momentum to improve resolution. To reject non-muon tracks, the energy deposited in the calorimeter within a one cell radius around the track is required to be at least 1 Gev. A higher threshold of 1.5 GeV is used if the track does not match with any CD track.

- Isolation. The distance R, in η, ϕ space, between a muon track and the nearest jet must be at least 0.5.

Our muon candidates are also required to be contained entirely within the WAMUS system, with $|\eta| <1.7$ (the muons are required to be contained in the central muon (CF) system for a later part of the run due to efficency issues in the end chambers as a result of chamber aging). A requirement of $E_T > 15$ GeV is applied for muons form W decays. The efficiency for identifying energetic and isolated muons in $t\bar{t}$ events with the above criteria is ≈41%. A somewhat looser set of requirements is used for identifying soft muons from semileptonic decays of b quarks.

3.2.3 Missing-E_T

Since a typical $p\overline{p}$ collision has negligible net transverse energy, the presence of neutrinos or any particles that escape detection creates an imbalance in the observed total transverse momentum. This imbalance is known as "missing E_T" (denoted by $\not\!\!E_T$). It is measured by first summing the transverse components of energy deposited in every calorimeter and ICD cell [74]:

$$\not{E}_{T\ x}^{\mathrm{cal}} = -\sum_{i=1}^{N_{cells}} E_{xi} \tag{3.5}$$

$$\not{E}_{T\ y}^{\mathrm{cal}} = -\sum_{i=1}^{N_{cells}} E_{yi} \tag{3.6}$$

The magnitude of $\not{E}_T^{\mathrm{cal}}$is given by summing the x and y components in quadrature. Any energy correction applied to electrons or jets in the event will also be applied to the $\not{E}_T^{\mathrm{cal}}$. The $\not{E}_T$of an event is simply given by $\not{E}_T^{\mathrm{cal}}$, except for the case where a muon is present, for which the the E_T of a muon will be first subtracted, component-wise, from the $\not{E}_T^{\mathrm{cal}}$. Based on the distribution of $\not{E}_T$in a sample of minimum-bias events, which were required to pass only the Level 0 trigger, the resolution can be parameterized as [74]:

$$\sigma(\not{E}_T) = 1.08GeV + 0.019 \times \sum_{Cells} E_T \tag{3.7}$$

3.2.4 Jets and Jet Energy Calibration

Due to hadronization and fragmentation, a quark or gluon produced in a $p\overline{p}$ collision is usually observed in the calorimeter as the combined energy shower of multiple hadrons, in the vicinity of the original parton. This cluster of energy is known as a calorimeter jet. There are several jet reconstruction method. This analysis uses the cone-clustering algorithm[66, 67, 68, 69]. In this algorithm, jets are formed using cones in η, ϕ space, defined by a radius R=$\sqrt{(\Delta\phi)^2 + (\Delta\eta)^2}$=0.5, where $\Delta\phi$ and $\Delta\eta$ correspond, respectively, to the sizes of the clusters in azimuth and pseudorapidity .

This is a standard algorithm used in previous experiments, and will not be discussed any further.

In a top analysis, one is usually interested in identifying the energy of a jet with that of its originating parton, so that one can accurately reconstruct the $t\bar{t}$ event. DØ achieves this kind of calibration in two steps. An initial standard energy correction is applied before event selection through a software package called "CAFIX"[70]. This calibrate jet energy, on average, back to the summed energies of the final-state particles contained within the jet cone. However, the energy in the jet cone may itself be different from the corresponding parton energy due to gluon radiation that carried energy outside the jet cone. Figure 3.1 [73] shows a scatter plot of the energies of generated partons versus those of their reconstructed jets in lepton+jets $t\bar{t}$ Monte Carlo events [80]. As can be seen, the R=0.5 cone algorithm used in this study yields jets of smaller energy than carried by the original partons. It is therefore important to apply further corrections to bring the jet energy, on average, back to that of the originating parton.

The procedures taken by DØ are described in Refs. [71, 72]. Two main corrections are applied. The first is a parton-level correction derived from matching reconstructed Monte Carlo jets to the corresponding partons in $t\bar{t}$ events. Different corrections are obtained for light quark and b quark jets by fitting plots similar to Fig. 3.1. The results are shown in Table 3.1 for different η regions of the calorimeter. There are separate corrections for b quarks that are tagged by soft muons, and are described in Ref. [71, 72]

After the parton-level corrections, a final adjustment is derived from both data and Monte Carlo, by selecting events with exactly one photon and one jet, and requiring them to be almost back-to-back (i.e. going in exact opposite direction in ϕ). Since the electromagnetic energy scale is well calibrated, a comparison of the

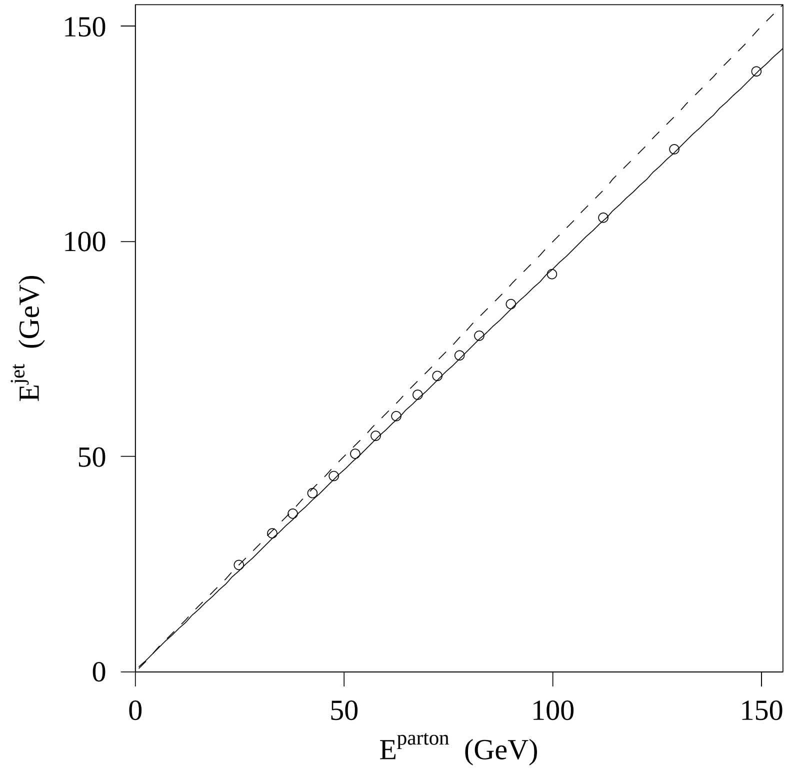

Figure 3.1: Effect of radiation outside the jet cone [73]. The reconstructed jets have on average less energy than the original parton, and require corrections that are based on a comparison of parton energies and energies of reconstructed jets in $t\bar{t}$ events (circles). The correction attempts to provide a 1:1 correspondence (given by the dashed line).

reconstructed E_T response can reveal any deviation between the true (EM) energy scale and the jet energy scale. This deviation is summarized as a fractional difference ΔS between the E_T of the photon and the jet:

$$\Delta S = \frac{E_T(jet) - E_T(\gamma)}{E_T(\gamma)} \tag{3.8}$$

Table 3.1: Parameters for jet energy corrections to the parton level. $E_{corr} = (E_{jet} - A)/B$.

	Light quark jets		Untagged b jets	
η region	A (GeV)	B	A (GeV)	B
$0.0 < \|\eta_{\rm det}\| < 0.2$	0.322	0.933	-0.672	0.907
$0.2 < \|\eta_{\rm det}\| < 0.6$	0.635	0.930	-1.34	0.914
$0.6 < \|\eta_{\rm det}\| < 0.9$	1.86	0.883	0.002	0.868
$0.9 < \|\eta_{\rm det}\| < 1.3$	1.70	0.933	-0.548	0.904
$1.3 < \|\eta_{\rm det}\|$	4.50	0.882	2.46	0.859

The results for both MC and data [75, 80] are shown in Fig. 3.2. The fit to the plots gives separate corrections for data and MC events, and are independent of jet types.

In this analysis, we use a new, more precise jet energy correction parametrization, taking into account the fact that energy losses due to hadronization and radiation are strongly asymmetric relative to the original parton energy, that was developed for the most recent DØ Run I top mass and W helicity measurement[76, 77]. This is described in the next chapter.

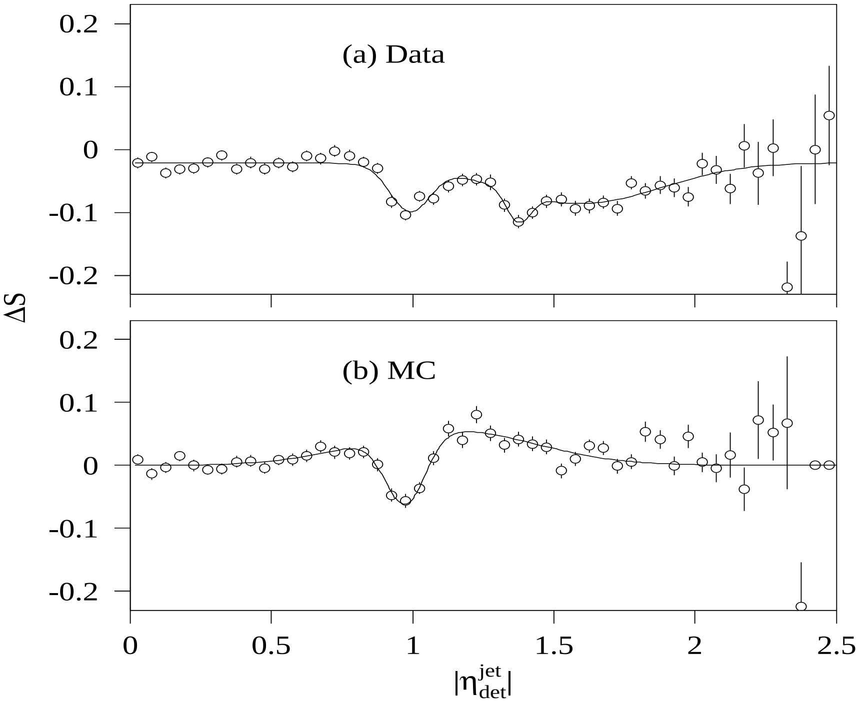

Figure 3.2: Dependence of the deviation in the jet energy scale (ΔS) for γ+jets data and MC events, as a function of $|\eta|$ [73].

Chapter 4

The Method of Analysis

This analysis employs a method that was recently developed for studying the properties of top quark. The central idea is to calculate the likelihood of occurrence of any event by directly using the matrix element, or theoretical differential cross section, for the production and decay processes. The strength of this method is that all the correlations between observed kinematic variables in an event are included in determining the theory that fits the data best. The method has been used in the measurement of the top mass and W helicity in Run I [76, 77], with results that show great improvement over methods used in previous analyses. We outline the method in the following sections. More details can be found elsewhere [76, 77].

4.1 General Calculation of Event Probability

In its simplest form, the differential probability of observing an event with n final-state partons and corresponding four-momenta $y = (p_1,...,p_n)$ in a proton-antiproton collision can be written as:

$$P(y,\alpha) = \frac{1}{\sigma}\int d\sigma(q_1,q_2,y,\alpha) f(x_1) f(x_2) dx_1 dx_2 \tag{4.1}$$

where α is the parameter of interest, q_i and x_i are the four-momenta and momentum fractions, respectively, carried by the initial partons, and $f(x_i)$ are the parton distribution functions (PDF). The differential cross section $d\sigma$ is given by [3]:

$$d\sigma = \frac{(2\pi)^4|M|^2}{4\sqrt{(q_1\cdot q_2)^2 - m_{q1}^2 m_{q2}^2}} \quad d\Phi_n(q_1+q_2; p_1, ..., p_n) \quad , \tag{4.2}$$

where M is a Lorentz-invariant matrix element, m_{q_1}, and m_{q_2} are the masses of the initial partons, and $d\Phi_n$ is an element of n-body phase space given by

$$d\Phi_n(P; p_1, ..., p_n) = \delta^4(P - \sum_{i=1}^{n} p_i) \prod_{i=1}^{n} \frac{d^3 p_i}{(2\pi)^3 2E_i} \quad . \tag{4.3}$$

For convenience, we will use $P(y)$ and $P(y,\alpha)$ interchangeably in the rest of the discussion.

In most experiments, the parton momenta cannot be measured perfectly, and not all produced events are detectable. Therefore, effects of measuring resolution and acceptance have to be taken into account. Knowing the resolution function (also called transfer function) $W(x|y)$, which gives the probability density for measuring $x = (p'_1,...,p'_n)$ given the corresponding parton values (y), the total differential probability of measuring x is:

$$P(x)dx = (\int W(x|y)P(y)dy)dx \tag{4.4}$$

where $P(x)$ is a probability density in x.

When acceptance is taken into account, the probability of observing a particular event will change because the total observable cross section will change. As a result, the probability will be modified to:

$$P'(x)dx = \frac{A(x)P(x)dx}{\int A(x)P(x)dx} \tag{4.5}$$

where $A(x)$ is the acceptance function, and $\int A(x)P(x)dx$ is (by definition) the average acceptance $\langle A \rangle$.

To calculate the probability for any given event, one can in principle generate a large number of events according to $P(y)$, pass them through the full event simulation and reconstruction to apply resolution and acceptance effects, and estimate $A(x)P(x)dx$ by counting how many events fall within dx. This is, however, usually an impossible task due to the time required for processing each event. The only practical solution is to parametrize the effects of simulation and reconstruction, and perform numerical integration over y according to the parametrization. Therefore the calculation of $A(x)P(x)dx$ is effectively a series of parametrized Monte Carlo simulation (PMCS), except that no events are actually being generated. This will be the approach used.

For any set of N independent events, with the event probabilities known, the parameter of interest can be estimated by the method of maximum likelihood, in which the likelihood is defined by:

$$L(\alpha) = \prod_{i=1}^{N} P(x_i, \alpha) \tag{4.6}$$

The estimator of true α is taken to be the α value that maximizes the likelihood. Since $L(\alpha)$ usually changes rapidly with α, it is customary to minimize -ln$L(\alpha)$ instead. Both procedures yield the same estimator. The acceptance function $A(x)$, while does not depend on α (nor on whether the event is signal or background), affects the value of the estimator through $\langle A\rangle(\alpha) = \int A(x)P(x,\alpha)dx$, and therefore its effect must be estimated.

4.2 Probability of Single-Lepton $t\bar{t}$ Events

4.2.1 Transfer Function

As mentioned in Section 1.2, a typical lepton+jets $t\bar{t}$ event involves two initial and six final state fermions. Neglecting the transverse momentum of the initial partons, the differential cross section depends on 20 variables: the momenta of the 4 final state quarks, the lepton and the neutrino, and the longitudinal momenta of the 2 initial quarks. Each of the measured quantities (the momenta of the 4 final state quarks and the lepton) is associated with a transfer function:

- For quantities that are well-measured, such as the electron momenta and the directions of muons and quarks, a Dirac δ-function $\delta(x_i - y_i)$ is used as the transfer function (i.e., assuming the measured value is same as the produced value).

- The muon and jet momenta are not measured to the precision of the electrons. To account for the resolution effects, the muon transfer function, given by Eq. 2.5, is included in the integration. For the jets, specific transfer functions were derived by comparing parton and reconstructed jet energies in Monte Carlo $t\bar{t}$

events. The details, including extensive Monte Carlo studies, can be found in Ref. [77].

4.2.2 Transfer Function for Jets

The jet transfer functions are parametrized by the sum of two Gaussians of the form:

$$W_{jet}(E_{jet}|E_{parton}) = \frac{1}{\sqrt{2\pi}(p_2 + p_3 p_5)}[\exp\frac{-(\delta_E - p_1)^2}{2p_2^2} + p_3 \exp\frac{-(\delta_E - p_4)^2}{2p_5^2}] \tag{4.7}$$

where E_{parton} is the energy of the parton, E_{jet} the corresponding reconstructed jet energy, and $\delta_E = E_{parton} - E_{jet}$. The p_i are in turn parametrized as:

$$p_i = a_i + b_i E_{parton} \tag{4.8}$$

The parameters p_i are observed to be essentially independent of the η of the partons/jets, but do depend on whether the parton is a heavy (b) or light quark (u, d, c, s). Two separate sets of p_i are therefore derived (and subsequently used) based on the flavors of the quarks. The parameters for the transfer functions are shown in Table 4.1

4.2.3 The Phase Space

The calculation of $P(x)$ is an integration over 20 parton variables. The use of δ-functions as transfer functions eliminates 11 of the integrations (3 for the electron momentum vector and 8 for the jet directions), and the total energy-momentum

Table 4.1: Parameters for $W(E_{parton}, E_{jet})$ for jets from HERWIG $t\bar{t}$ events that were matched to partons.

	Light quark jets		b jets	
$p_i = a_i + b_i \times E_{parton}$	a_i	b_i	a_i	b_i
p_1 (GeV)	-1.65	-0.038	-3.41	-0.0333
p_2 (GeV)	2.84	0.067	3.98	0.0673
p_3 (dimensionless)	0.00	0.001	0.00	0.002
p_4 (GeV)	11.56	-0.302	3.36	-0.227
p_5 (GeV)	10.73	0.173	15.17	0.138

conservation constraints remove 4 others (the (p_x, p_y) of the neutrino and p_z of the two initial quarks). The integration over the remaining 5 parton variables (momentum $|\overrightarrow{p_i}| = \rho_i$ of the four quarks and p_z of the neutrino) is done numerically. To take advantage of the concentration of differential cross section around the four top and W Breit-Wigner(BW) mass peaks, a change of variables is performed which transforms the integration variables to those four masses and ρ_1 of one of the final state quarks. This provides a better knowledge of where to search for large $P(y)$, and thus $P(x)$, in phase space. Appendix A describes this transformation and contains the details of the phase space for single-lepton $t\bar{t}$ events.

For each set of masses and ρ, the remaining undetermined parton quantities are calculated by applying the mass constraints and solving the corresponding kinematic equations simultaneously. Details of the calculation can be found in the Appendix of Ref. [77].

The total phase space factor after integrating over the δ-functions for total energy and momentum conservation (i.e., over the p_x, p_y of the neutrino and the longitudinal momenta of the initial quarks) is:

$$d\Phi_6 = \frac{4}{(2\pi)^4}\ \Phi_6\ d^3\overrightarrow{p}_e\ d\rho_1 dm_1^2 dM_1^2 dm_2^2 dM_2^2 \prod_{i=1}^{4} d\Omega_i \tag{4.9}$$

with

$$\begin{aligned}\Phi_6 = {} & \frac{4}{(4\pi)^{14}}\frac{1}{E_e E_\nu}\prod_{i=1}^{4}\frac{\rho_i^2}{E_i} \\ & \times \frac{1}{|E_1\frac{\rho_2}{E_2} - \rho_1\cos\theta_{12}|}\frac{1}{|E_1\frac{\rho_3}{E_3} - \rho_1\cos\theta_{13} + E_2\frac{\rho_3}{E_3} - \rho_2\cos\theta_{23}|} \\ & \times \frac{1}{|E_e\frac{p_\nu^z}{E_\nu} - p_e^z|}\frac{1}{|E_e\frac{\rho_4}{E_4} - \rho_e\cos\theta_{e4} + E_\nu\frac{\rho_4}{E_4} - \rho_\nu\cos\theta_{\nu 4}|} \quad ,\end{aligned} \tag{4.10}$$

where $\rho_i = |\overrightarrow{p}^i_{quarks}|$, E_i are the quark energies, Ω_i are the solid angles of the quarks, $m_1(m_2)$ is the invariant mass of the W in $W \to q\overline{q}$ ($W \to e\nu$), and $M_1(M_2)$ is the invariant mass of the top quark in the hadronic (leptonic) branch.

4.2.4 Calculation of $P_{t\bar{t}}(x)$

Combining eq. 4.1, 4.4, and 4.9, the probability for single-lepton $t\bar{t}$ events can be written as:

$$P_{t\bar{t}}(x) = \frac{1}{\sigma_{t\bar{t}}}\int |M|^2\ \frac{f(q_1)}{|q_1|}\frac{f(q_2)}{|q_2|}\ W(x|y)\ \Phi_6\ d\rho_1 dm_1^2 dM_1^2 dm_2^2 dM_2^2 d^3\overrightarrow{p}_e \prod_{i=1}^{4} d\Omega_i \quad , \tag{4.11}$$

where the masses and transverse momenta of the initial partons are neglected – that is, we assume $\sqrt{(q_1 \cdot q_2)^2 - m_{q_1}^2 m_{q_2}^2} = 2|q_1||q_2|$.

Since it cannot be determined with certainty which jet originates from which parton, there is ambiguity in assigning the jet quantities to the partons. Therefore all 24 possible combinations of jet-parton correspondences are considered and added together with the same weight in the probability. In addition, after the change of integration variables to the W and top masses, due to the relation between mass and momentum, it is possible for a given set of masses to correspond to more than one set of parton values. In particular, multiple solutions for the p_z of the neutrino can be found. All of these p_z solution are combined. Taking these into account, and integrating over all the δ-functions, the probability density for single-lepton $t\bar{t}$ events is given by:

$$\boxed{P_{t\bar{t}}(x;\alpha) = \frac{1}{24\,\sigma_{t\bar{t}}} \int d\rho_1 dm_1^2 dM_1^2 dm_2^2 dM_2^2 \sum_{comb.+\nu} |M|^2 \frac{f(q_1)}{|q_1|}\frac{f(q_2)}{|q_2|}\,\Phi_6 \prod_{i=1}^{4} W_{jet}(E_i^x|E_i^y)} \tag{4.12}$$

where $W_{jet}(E^x|E^y)$ is defined in Section 4.2.2, Φ_6 is the phase space factor given in Section 4.2.3, and $f(q)$ is the parton distribution function. The summation is over all combinations and solutions for the neutrino p_z. It should be noted that there is no difference between performing the summation inside or outside the integral.

The $t\bar{t}$ matrix element is calculated using a Madgraph-based[33] leading order matrix element generator [34], with modifications to include the effect of anomalous $gt\bar{t}$ couplings. In this analysis, we focus on the $q\bar{q} \to t\bar{t}$ process and its matrix element, and ignore the $\approx$ 10 % contribution from $gg \to t\bar{t}$. Since the top width is very small, the integration over the top masses are performed using the narrow width approximation:

$$\int \frac{F(m^2)dm^2}{(m^2 - M^2)^2 + (M\Gamma)^2} \approx \frac{\pi F(M)}{M\Gamma} \tag{4.13}$$

For the integration over the W masses, a CERN mathematical library subroutine which employs a multi-dimensional adaptive quadrature integration method[78] is used, after minor modifications to provide speed improvements. For each given set of W and top masses, an integration over ρ_1 is performed with a subroutine, also from the CERN mathematical library, that uses the one-dimensional adaptive Gaussian quadrature method.

4.3 Probability for Signal and Background

Besides $t\bar{t}$ production, any background process that can contribute to the final state observed must be included in the probability calculation. The total event probability with N possible production process can be written as:

$$P(x) = \sum_{i=1}^{N} c_i P_i(x) \quad , \tag{4.14}$$

where

$$c_i = \frac{\sigma_i}{\sum_{i=1}^{N} \sigma_i} \tag{4.15}$$

i.e. the c_i represent the fractional cross section for process i. (The cross sections should be replaced by accepted cross sections $\langle A \rangle \sigma_i$ when acceptance effects are present). Since $\sum c_i = 1$, there are only N-1 independent c_i. If any one of these N-1 c_i is not known, it can be estimated from data as an additional parameter in the minimization.

For the l+jets $t\bar{t}$ data sample from DØ in Run I, W+4 jets production represents about 80% of all physics background, while the remaining background is mostly multi-jet events. In this analysis, only the matrix element for the W+jets process will be included in the calculation of the final cross section. The effect of multi-jet events will be estimated from observed multijet data, and included as a systematic uncertainty.

The total event probability is therefore:

$$P(x, c_1, c_2, \alpha) = c_1 P_{t\bar{t}}(x, \alpha) + c_2 P_{W+jets}(x) \quad , \tag{4.16}$$

where $c_2 = (1 - c_1)$

The W+jets matrix element is calculated using one of the matrix element subroutines in the Monte Carlo event generator VECBOS[82], requiring that there are 4 partons. The integration variables are the momentum ρ_i of the four jets and the W mass. Since heavy quarks are relatively uncommon in the four jets accompanying the W, only transfer functions for light quark jets are used in the calculation of background probability. The integration is performed, with the use of the Monte Carlo integration routine VEGAS[79], over all 5 variables.

4.4 Acceptance

As indicated earlier, the final probability must be corrected for acceptance effects. The average acceptance in Eq. 4.5 is calculated using Monte Carlo methods. We generate parton-level events according to the differential cross section (i.e., these events are unweighted), then hadronize and pass them through detector simulation, reconstruction, and event selections. Since the events are generated according to the differential cross section:

$$P(y)dy = \frac{dN(y)}{N_{gen}} \tag{4.17}$$

where N_{gen} is the total number of events generated and $dN = N_{gen}P(y)dy$.

After processing, the events will be distributed according to:

$$A(x)P(x)dx = \frac{dN_{acc}(x)}{N_{gen}} \quad , \tag{4.18}$$

where $P(x)$ is the probability for x before acceptance effect and $dN_{acc} = N_{gen}A(x)P(x)dx$ is the number of accepted events in the differential volume dx. The average acceptance is therefore given by:

$$\int A(x)P(x)dx = \frac{N_{acc}}{N_{gen}} \tag{4.19}$$

where N_{acc} is the total number of events accepted.

From a set of events generated for a particular value of α, the average acceptance for a different α' can be calculated by reweighting:

At parton-level, for a set of unweighted events, from eq. 4.17

$$\begin{aligned} \int P(y,\alpha')dy &= \int P(y,\alpha')\frac{dN(y,\alpha)}{P(y,\alpha)N_{gen}} \\ &= \frac{1}{N_{gen}}\sum_{i=1}^{N_{gen}}\frac{P(y_i,\alpha')}{P(y_i,\alpha)} \end{aligned} \tag{4.20}$$

where in the last line we have written the integral as a sum over all generated events.

For fully simulated and reconstructed events, we first rearrange the order of integration in eq. 4.5:

$$\int A(x) \int W(x|y)P(y)dy\, dx = \int P(y) \int A(x)W(x|y)dx\, dy \qquad (4.21)$$

Since $\int A(x)W(x|y)dx$ is independent of α, one can proceed to calculate the average acceptance for a different α as in eq. 4.20.

Chapter 5

Studies using Resolution-Smeared MC Events

To estimate the reliability of the method and to uncover any potential biases, we first studied Monte Carlo events at the parton level, before proceeding with the more complex full simulation and reconstruction studies. Leading-order generators were used to simulate these events. The energies of the outgoing partons were smeared with appropriate jet transfer functions, which also enter into the calculation of the likelihood.

5.1 Event Samples

As discussed in Section 1.3, the predicted $t\bar{t}$ production cross section varies with A_2. We therefore use the observed cross section ($\sigma_{t\bar{t}}$) in Run I, and its uncertainty ($\delta\sigma_{t\bar{t}}$) as a guide for selecting the range of our investigation, and we limit the A_2 values to those that correspond to less than or about $3 \times \delta\sigma_{t\bar{t}}/\sigma_{t\bar{t}}$ deviations from the predicted Standard Model $t\bar{t}$ cross section (σ_{SM}). The $t\bar{t}$ production cross section from Run

I is 5.69 ± 1.60 pb for a top mass of 172.1 GeV/c^2 [29]. Since $\pm\ 3 \times 1.60/5.69 = 0.84\ \sigma_{SM}$, the approximate range of interest in cross sections is $0.16\sigma_{SM}$ to $1.84\sigma_{SM}$ with the corresponding range of A_2 values.

Smeared parton-level event samples, each with about 100,000 $t\bar{t} \rightarrow$ e+jets or μ+jets events, were generated with a leading-order (tree-level) matrix-element generator [34] based on Madgraph[33] for $A_2 = -4, -2, 0$ (SM), 2, 4, 6, 9, 12 using a top mass of 175 GeV/c^2, W mass of 80.4 GeV/c^2, and $\sqrt{s} = 1.8$ TeV. (For these parameters, the corresponding values of $\sigma(A_2)/\sigma_{SM}$ values, as calculated using the same generator, are 1.94, 1.42, 1, 0.69, 0.49, 0.4, 0.47 and 0.78). As mentioned in Chapter 4, we ignore the $\approx$ 10% contribution from $gg \rightarrow t\bar{t}$ to the cross section, and focus on the $q\bar{q} \rightarrow t\bar{t}$ process. (The incorporation of the small gg component is left for future analyses with more data and greater sensitivity.) For the W+jets background, we use the Monte Carlo event generator VECBOS[82], with the same specifications that were used for the Run I W+jets Monte Carlo samples (see Chapter 6). After the energies of the final-state partons were smeared with the jet transfer function according to their flavors, the final samples were selected with some of the same criteria used for Run I data:

- electron $E_T > 20$ GeV and $|\eta|$ <2.0
- smeared parton $E_T > 15$ GeV and $|\eta|$ <2.0
- $\not{E}_T$(from smeared quantities) >20 GeV

An additional $\Delta R = \sqrt{(\delta\phi)^2 + (\delta\eta)^2} > 0.5$ requirement between any two final-state partons was applied to simulate the effect of using 0.5 cone jet algorithm in the fully reconstructed Monte Carlo and data.

Only a small fraction of events remains after the above selections, with 2000 events from each sample used for the calculation of the likelihood and further studies.

5.2 Determination of A_2

We study the A_2 extraction method with Monte Carlo experiments for large and small statistics and different signal-background compositions. For each event, a grid of likelihood values was first calculated in steps of 1.0 from A_2 = -15 to 25. These likelihoods are combined for each "experiment" and, when background probabilities are included, they are combined with a variable signal fraction c_1 (Eq. 4.16). A two-dimensional(2-D) simultaneous minimization is then carried out on this combined likelihood (L) in A_2 and c_1, using the CERN numerical minimization package MINUIT[83]. During the minimization, at each c_1 probe value, the grid points in A_2 are interpolated with a 3-point quadratic (exact) fit, except near a local minimum where a 5-point quartic (exact) fit is performed. The uncertainty δA_2 (or δc_1) on the extracted value (the one with the smallest -ln(L) and therefore highest combined probability density) is given by a Gaussian fit (also performed by MINUIT) to the region around the minimum. (In more technical terms, it is the diagonal element in the inverse of the second derivative matrix $\partial^2 \ln L / \partial A_2 \partial c_1$ that corresponds to A_2 (or c_1). This uncertainty therefore takes into account the correlation between A_2 and c_1.)

The distribution in the extracted minimum (for many pseudo-experiments) provides an estimate of the response of the method for each input A_2. To minimize bias due to asymmetry in the likelihood functions and in the resulting distribution, we use the mode (instead of mean) of the distribution as the estimator of response. The mode is calculated by an iterative procedure studied by Bickel[84]. To estimate the uncertainty on the mode, we repeat this procedure many (in our case 50) times (i.e., creating multiple ensemble distributions) to obtain a distribution of the modes, and use the RMS of this distribution as the uncertainty for this estimator.

5.3 Studies using Signal

We first examined ensembles of Monte Carlo experiments consisting of only $t\bar{t}$ (signal) events, and only a signal probability in the likelihood calculation. Figure 5.1 shows the response as a function of A_2 from a single experiment of 2000 different $t\bar{t}$ events at each input value. The error bars are the widths (δA_2) of the likelihoods for the extracted A_2 values. The linear fit to the response is consistent with no bias (slope of 1 and no offset), as expected since the transfer functions in the likelihood calculation match identically those used to produce the samples. The -ln$L$ function for the SM sample ($A_2 = 0$) is shown in Fig. 5.2.

For the same pure $t\bar{t}$ experiments, we then include a background probability (W+jets) in the likelihood calculation, and extract A_2 and c_1 simultaneously. Figure 5.3 shows the response as a function of input A_2, and we see that the correlation is unaffected. The extracted c_1 values as a function of A_2 are shown in Fig. 5.4. They are slightly smaller than the expected value of 1.0. This is understandable because we are optimizing the sum of signal and background contributions to the likelihood, and it is sometimes advantageous to assign a signal event to background when it falls into an overlapping region of kinematic phase space, where it may be more likely for the event to be produced through the background rather than signal process.

For experiments with smaller statistics, even with exact knowledge of the smearing functions, a biased response can develop, as is the case when we examine ensembles of 200 experiments, each with 18 $t\bar{t}$ events (number of signal events estimated in our Run I data sample, to be discussed in Chapter 7), without considering background probability. The response as a function of input A_2 is shown in Fig. 5.5.

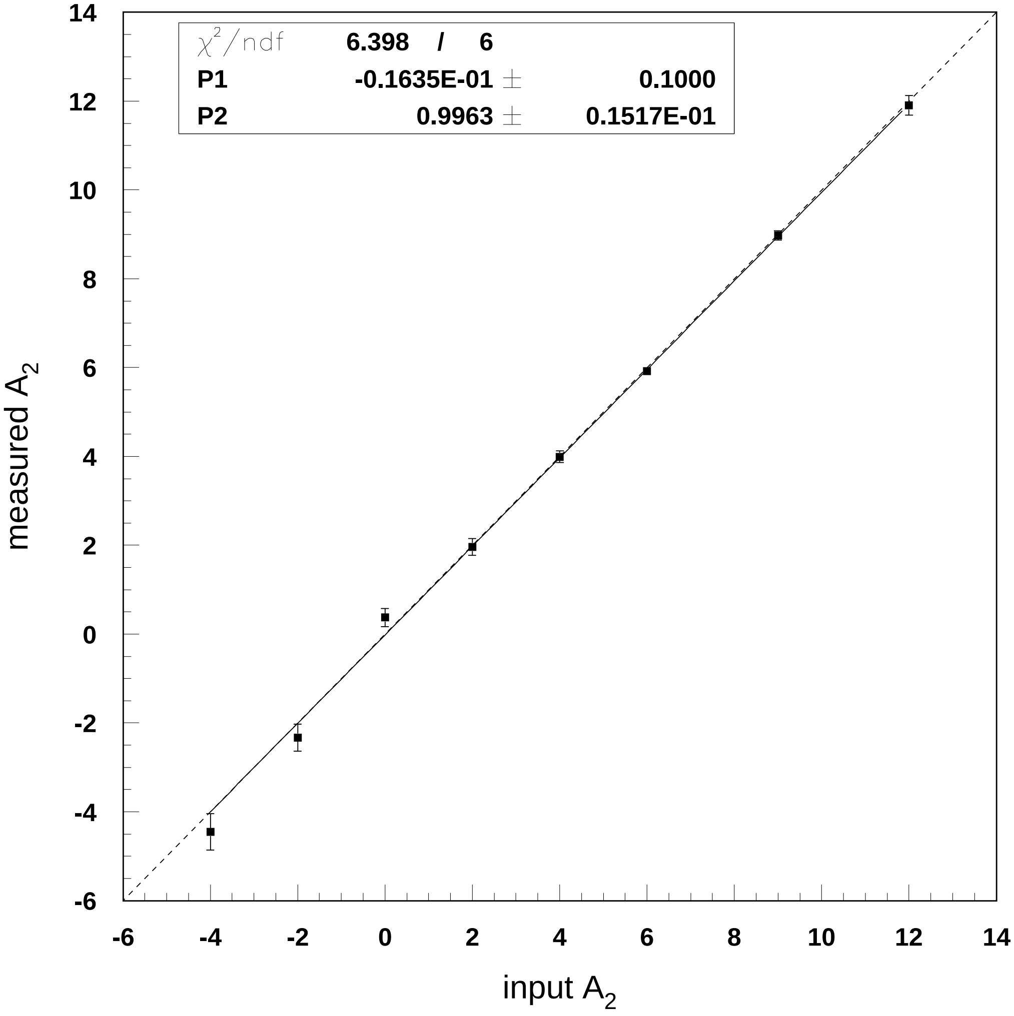

Figure 5.1: Extracted A_2 for a single experiment of 2000 $t\bar{t}$ events as a function of input A_2. The likelihoods for these experiments use only $t\bar{t}$ signal probabilities. The error bars are from the widths of the likelihood fits. The solid line corresponds to a linear fit to the data points. The dashed line is the diagonal corresponding to a slope of 1 and no offset.

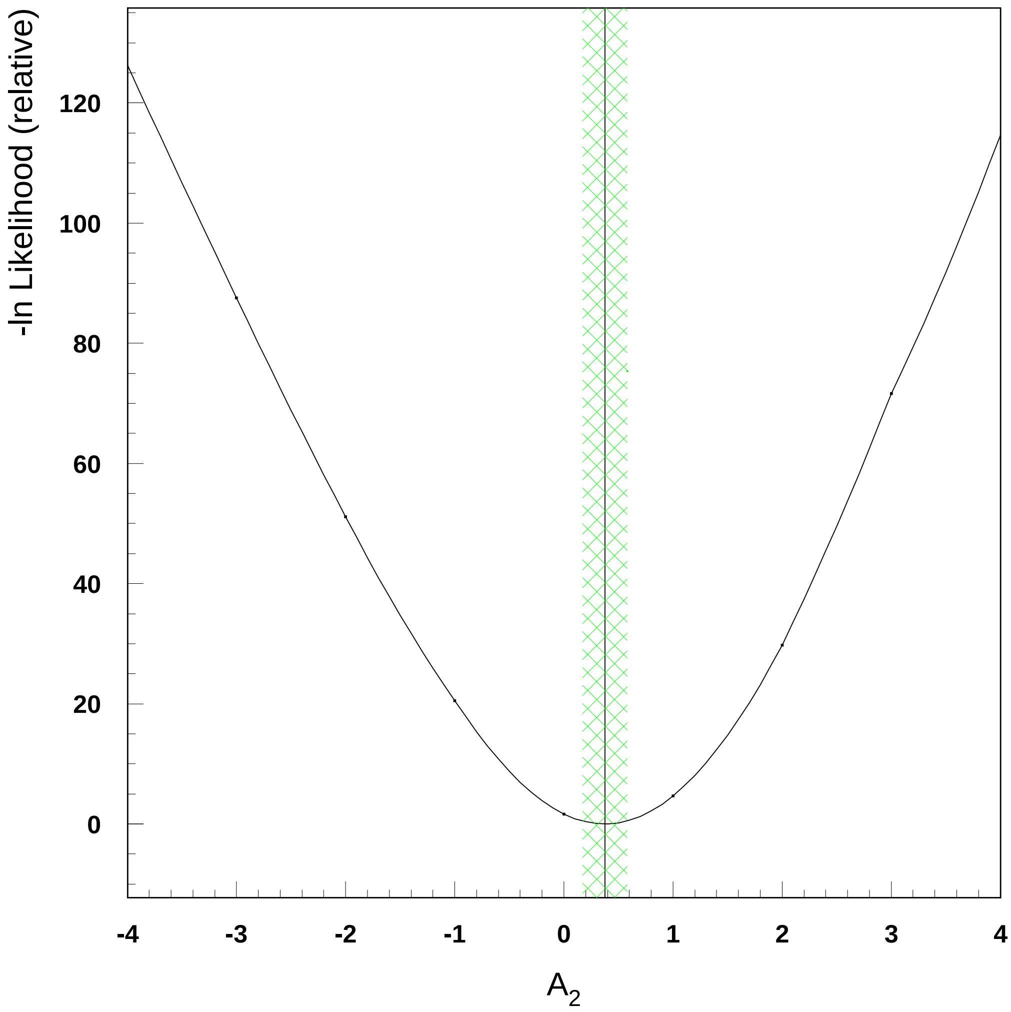

Figure 5.2: -ln(Likelihood) as a function of A_2, for an experiment of 2000 SM $t\bar{t}$ MC events. The vertical line indicates the extracted A_2 value and shaded region represents the estimated δA_2. Only the $t\bar{t}$ signal probability is used in the likelihood.

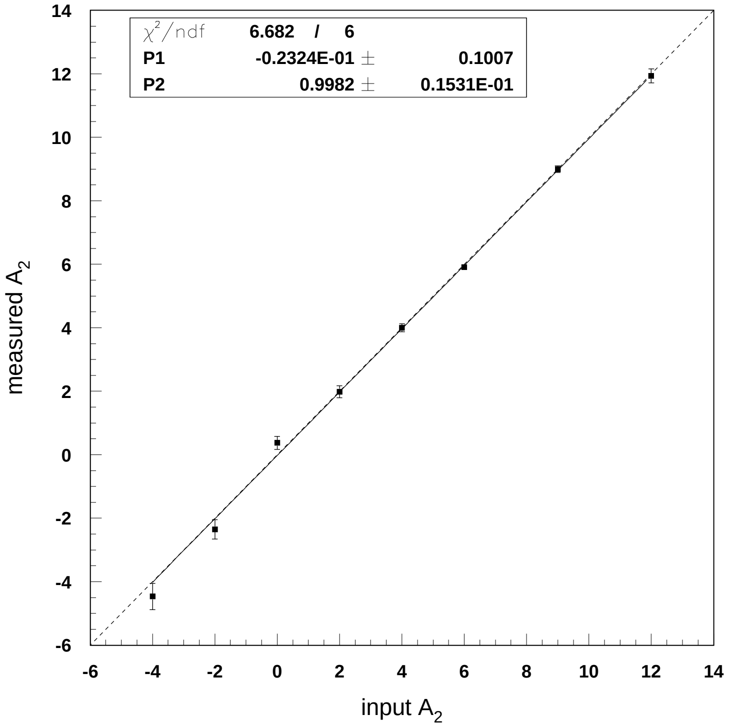

Figure 5.3: Response for pure $t\bar{t}$ experiments of 2000 events as in Fig. 5.1, but with the inclusion of a background probability in the calculation of total event probability in the form $P(A_2, c_1) = c_1 P_{t\bar{t}}(A_2) + c_2 P_{W+jets}$.

5.4 Studies using Signal and Background

To understand the effect of background on our measurement of A_2, we perform ensemble tests with varying number of $t\bar{t}$ and W+4 jets events, and minimize the likelihood in both A_2 and c_1. Figure 5.6(a) shows the response for single experiments of 2000 signal with 2000 W+4 jets background events. The response remains virtually unaffected relative to the case of pure signal. The corresponding extracted c_1, shown in Fig. 5.6(b), are consistent with the expected value of 0.5. It should be noted that the statistical fluctuations here among the A_2 samples only reflect that

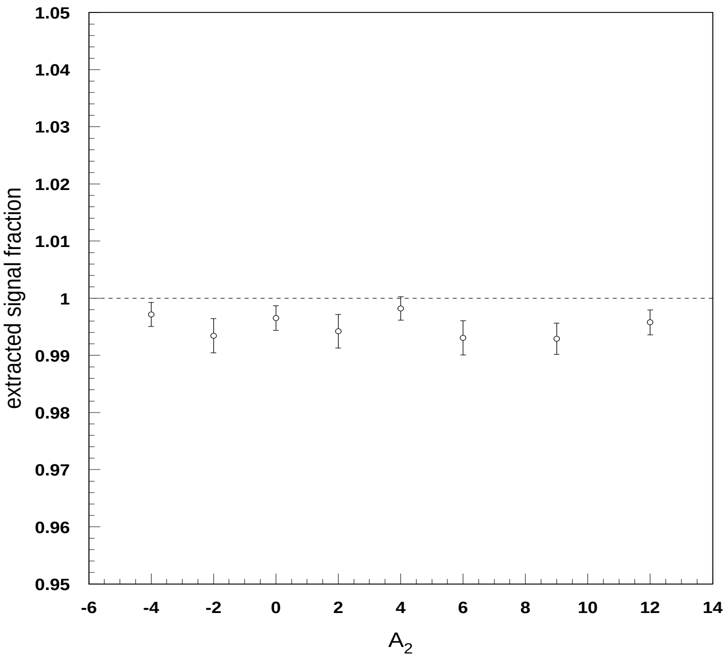

Figure 5.4: Extracted signal fraction c_1 as a function of input A_2, for pure $t\bar{t}$ experiments of 2000 events.

of the signal events since the same 2000 background events are used for each of the A_2 values.

Figure 5.7 shows the response for ensembles of 200 experiments, each with a composition of 18 $t\bar{t}$ and 53 W+jets events (corresponding to our data sample of 71 events). The observed bias is consistent with that for pure $t\bar{t}$ experiments, indicating that the inclusion of W+jets background has relatively small impact on the response. The dependence of response for A_2 on signal fraction (mostly the statistics of the signal as the effect of the background is small) is shown for two A_2 values (0 and 2) in Fig. 5.8.

The extracted c_1 as a function of input c_1 is shown in Fig. 5.9 for four A_2 values. The linear fits are consistent with each other. This implies that c_1 calibrations can

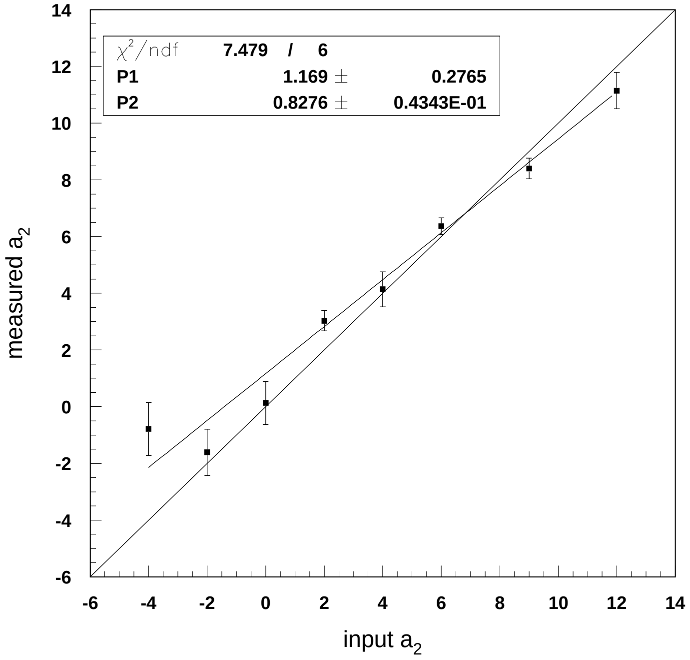

Figure 5.5: Response as a function of input A_2 for ensembles of 200 experiments, each with 18 $t\bar{t}$ events and no background. Only the $t\bar{t}$ signal probability is used in the likelihoods.

be derived and applied with little dependence on the knowledge of the true A_2 value.

5.5 Cross-check of Integration

To confirm that our probability calculation and numerical integrations are correct, we calculated the total cross section in two ways. Ignoring acceptance, and noting that $\int W(x|y)P(y)dydx = \int P(y)dy$, we checked that the same result is obtained by integrating the first integral over x and y, and the second integral over y. The results, as ratios $\int W(x|y)P(y)dydx / \int P(y)dy$, are shown in Fig. 5.10 for four A_2 values.

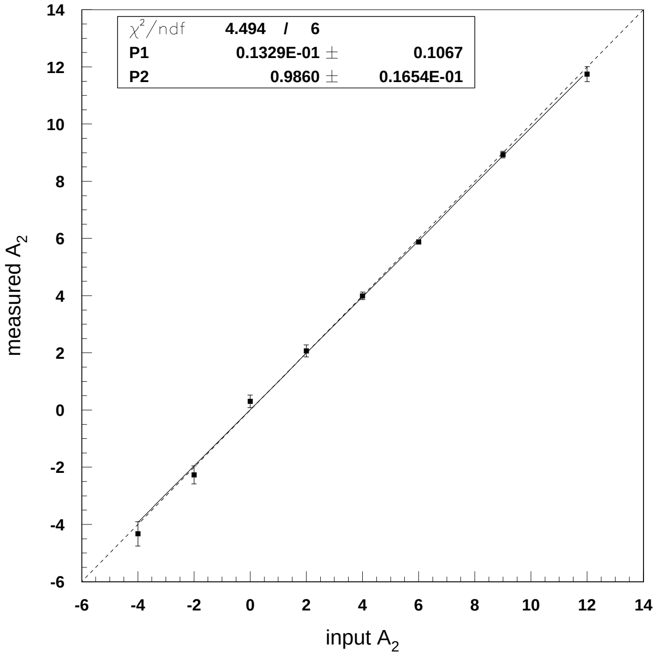

(a)

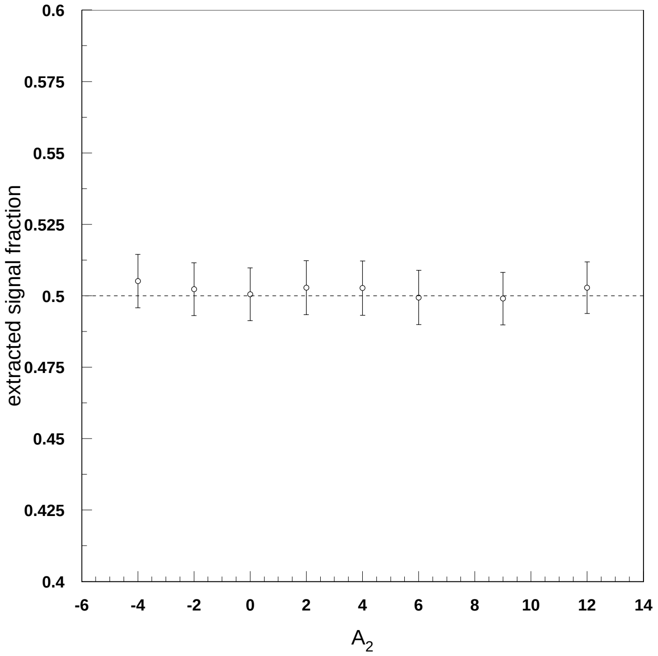

(b)

Figure 5.6: Response for single experiments of 2000 $t\bar{t}$ and 2000 W+jets events, as a function of input A_2. The probability densities in the likelihood are calculated as $P(A_2, c_1) = c_1 P_{t\bar{t}}(A_2) + c_2 P_{W+jets}$; (a) Extracted A_2. (b) Extracted signal fraction c_1. The expected signal fraction is 0.5.

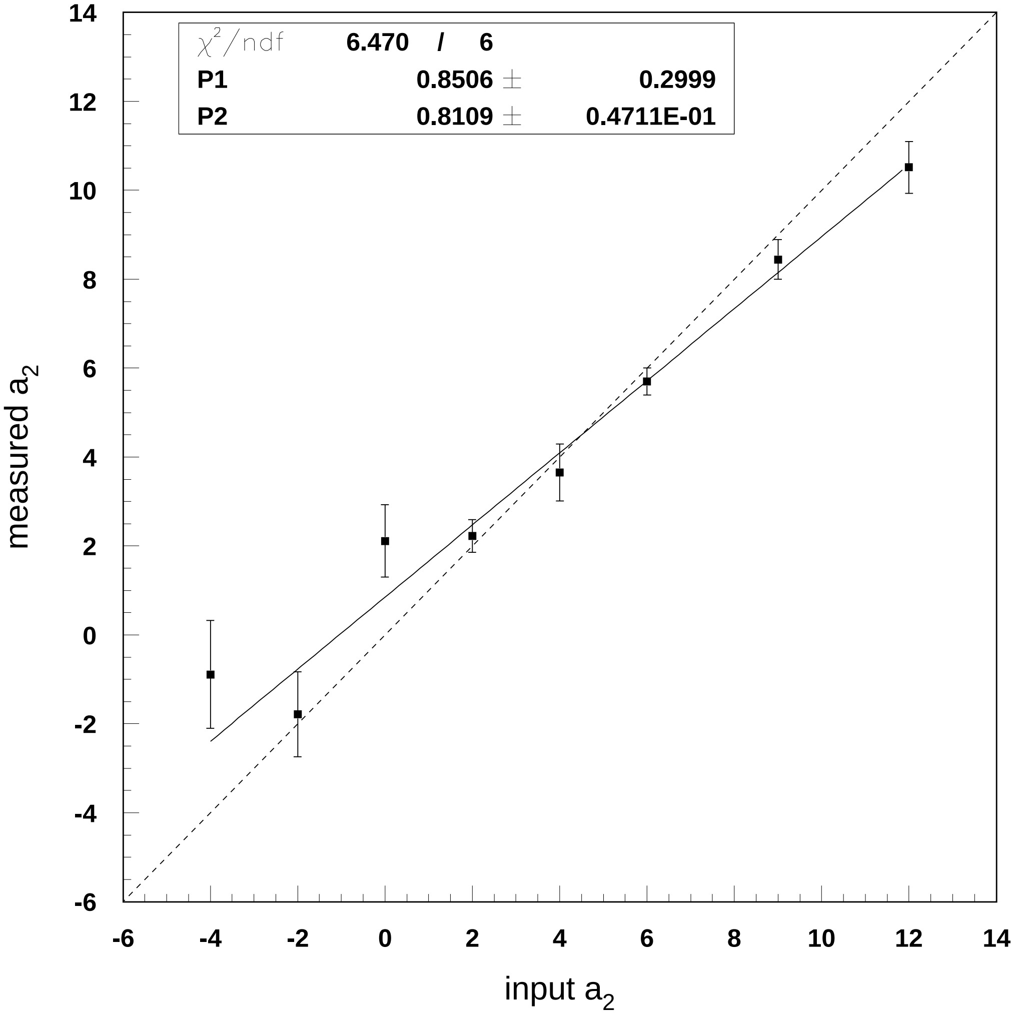

Figure 5.7: Response as a function of input A_2 for ensembles of 200 experiments, each with 18 $t\bar{t}$ and 53 W+jets background events.

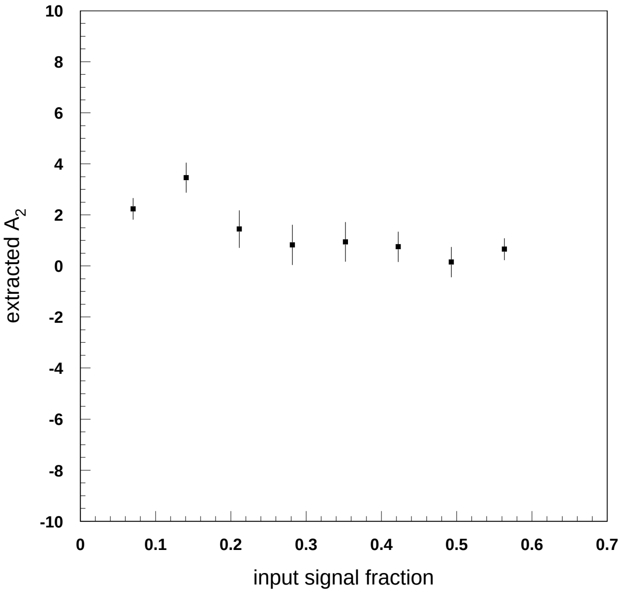

(a) $A_2 = 0$

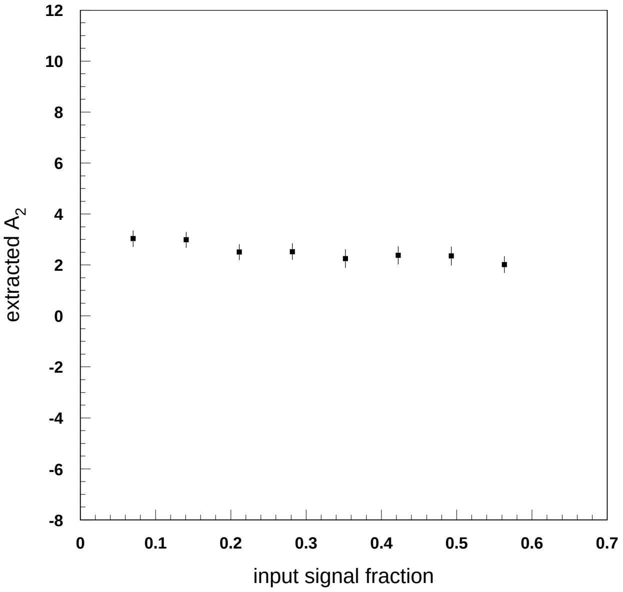

(b) $A_2 = 2$

Figure 5.8: Response from ensembles of 200 experiments, each with a total of 71 events, as a function of signal fraction, for $A_2 = 0$ and 2. The extracted A_2 departs from the expected value for small signal fractions (or poor signal statistics).

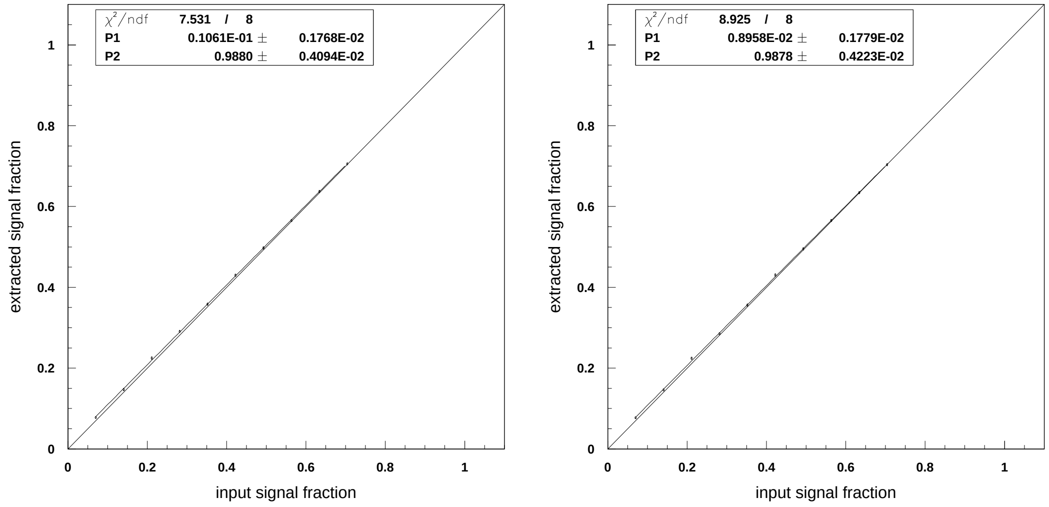

(a) A_2 = -2

(b) $A_2 = 0$

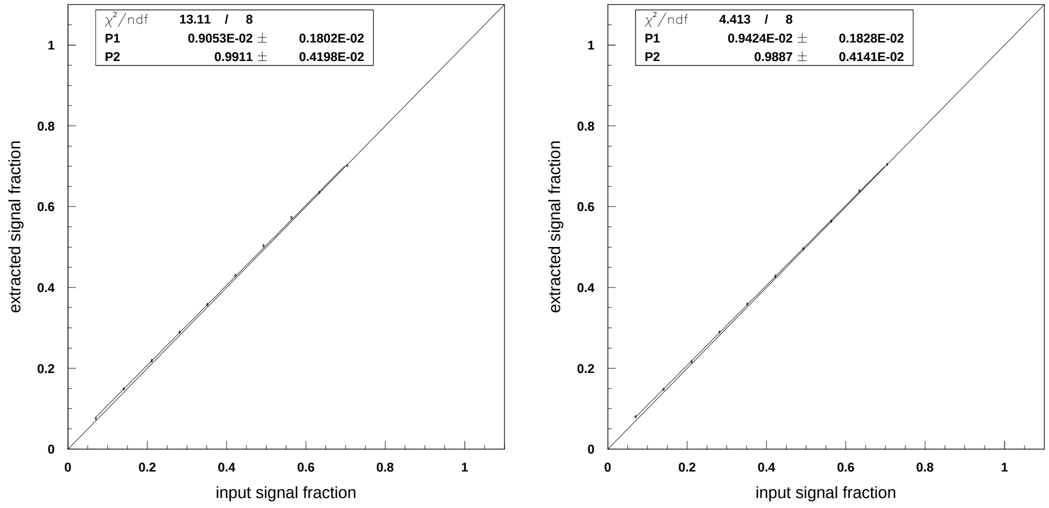

(c) $A_2 = 2$

(d) $A_2 = 4$

Figure 5.9: Extracted signal fraction as a function of signal-background composition, for 200 experiment of 71 events for 4 A_2 values.

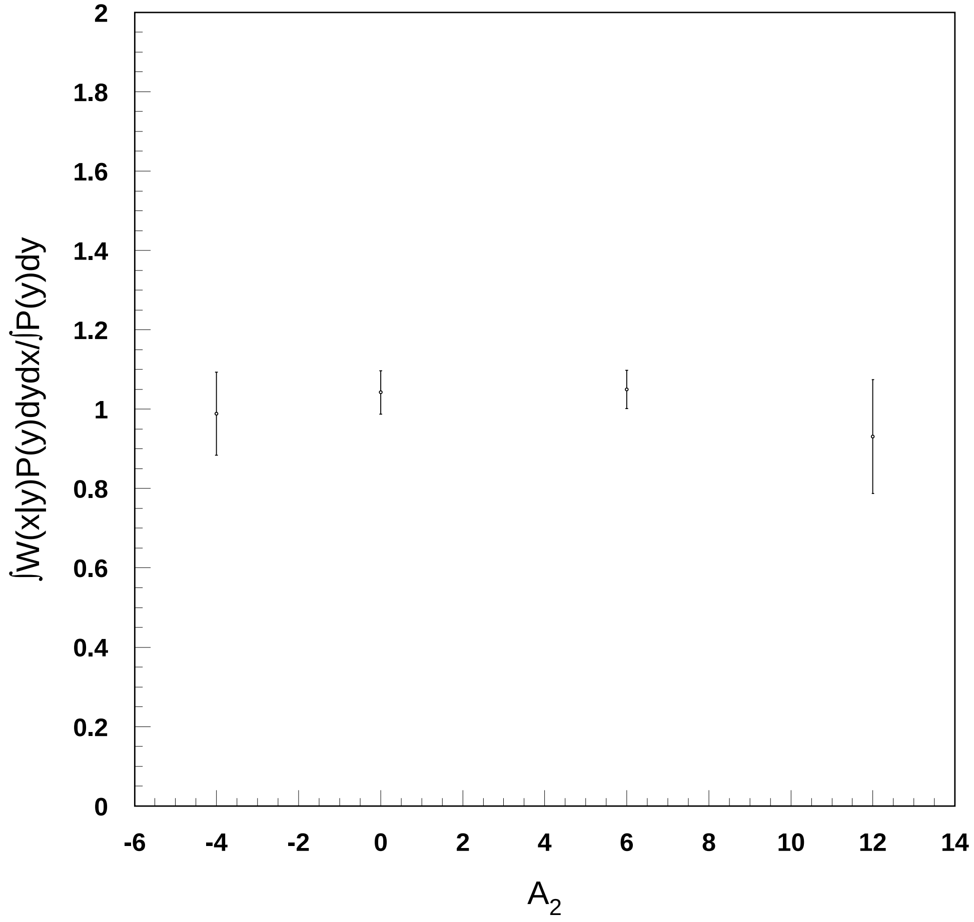

Figure 5.10: Ratios $\int W(x|y)P(y)dydx$ to $\int P(y)dy$, for 4 A_2 input values.

Chapter 6

Full DØ Simulation and Reconstruction

We next present the more realistic studies carried out with $t\bar{t}$ and W+jets Monte Carlo events that were passed through the full detector simulation and reconstruction. As with the smeared MC samples, we perform ensemble tests of these events for large and small statistics, and different signal to background compositions. The same procedures for determining the estimator of A_2, and estimating the response of the method, as in the smeared MC studies are also followed.

6.1 Event Samples

6.1.1 Signal Events

We used the PYTHIA event generator (Version 6.2) to process the decay and fragmentation of our parton-level Monte Carlo events (section 5.2), retaining all the specifications used in Run I: the CTEQ3M parton distribution function, initial and final state radiation switched on, and multiple interactions switched off. The events are then processed through DØGEANT, the detector simulation program[85], which is based on GEANT 3.15[86]. DØGEANT, however, does not describe accurately the efficiencies of the WAMUS PDTs. Therefore, outputs from DØGEANT were run through a standard correction package DØ MUSMEAR, which changes the efficiencies to the measured values on a chamber-by-chamber basis. We used the Run 1b "postzap" version for the measured efficiencies. The outputs are then passed through DØRECO[63] for final event reconstruction, and the Ntuple-Maker where the standard CAFIX 5.0 jet energy corrections are applied and event information extracted into an Ntuple, a common analysis-file format.

6.1.2 W+jets background

For W+jets Monte Carlo events, we used the samples that were generated for the previous top-mass analysis[87]. The parton-level events were produced using VECBOS[82], with the CTEQ3M parton distribution function and the dynamical scale set to be the average jet p_T. These events were then passed through the ISAJET event generator[88] for QCD evolution and fragmentation, followed by the same detector simulation and event reconstruction process as used for signal $t\bar{t}$ events. A total of 74,537 events were processed.

6.2 Event Selection

We begin with the same event selection designed for the previous top-mass analysis [87]. Besides the electron and muon channels, events were also divided into whether there was a "tag" muon consistent with originating from $b \to \mu + X$ decay. For each of these four channels, somewhat different selection criteria were used. The resulting data sample is referred to as the "precut" sample in the published D0 measurement of the mass of the top in the single-lepton $t\bar{t}$ events [73]. The primary criteria (for both tagged and untagged events unless otherwise specified) are:

- An isolated electron with E_T >20 GeV and $|\eta|$ <2.0, or an isolated muon with p_T >20 GeV/c and $|\eta|$ <1.7.
- At least 4 jets with E_T >15 GeV and $|\eta|$ <2.0.
- E_T^{cal} (the missing transverse energy obtained only from the calorimeter) $>$ 25 GeV/c for e+jets (untagged), and $>$ 20 GeV/c for μ+jets events.
- $\not{E}_T$(obtained by subtracting the transverse momenta of any identified muon in the event from E_T^{cal}) >20 GeV/c.

There were additional criteria based on whether an event is tagged or untagged. Details can be found in Ref. [73].

Since our lowest-order matrix elements describe events with only four final-state quarks (or gluons), we further require there are exactly 4 jets in an event. There are 91 events in the D0 precut sample, of which 71 events contain exactly 4 jets.

For our Monte Carlo samples, less than 15% of the events remain after the selections. We first use the samples that contain only one electron ($e + jets$ events). Within these samples, 4000 events for each A_2 input value and background are used for likelihood calculations and ensemble studies.

6.3 Studies using Signal

We begin our studies with experiments of 4000 $t\bar{t}$ events for each A_2 value, using only the $t\bar{t}$ signal probability in the likelihood. Fig. 6.1 shows the A_2 response as a function of input value. There is a small bias that can be attributed to poorly reconstructed events. By including a background probability in the likelihood and minimizing both A_2 and c_1 simultaneously, the response for A_2 shown in Fig. 6.2 becomes less biased, as some of the poorly reconstructed events, which usually have small signal and large background probabilities, are now considered background-like and have reduced effects on A_2. The extracted c_1 is about 0.91, which indicates that 9 % of the $t\bar{t}$ events are assigned to background.

We now use the statistic appropriate for the Run I data, which corresponds to 18 $t\bar{t}$ out of 71 events, for our ensemble studies. Figures 6.3 and 6.4 show the responses from 200 experiments of 18 pure $t\bar{t}$ events for different input A_2. Figure 6.3 uses only a $t\bar{t}$ likelihood, while W+jets background probability is included in Fig. 6.4. The results of the linear fits are consistent for the two figures. As was observed in the smeared MC studies, the bias increases for experiments with low statistics.

6.4 Studies using Signal and Background

We now examine MC experiments that include both $t\bar{t}$ signal and W+jets background events. Figure 6.5 shows the effect of adding the 4000 W+jets events to our 4000 $t\bar{t}$ events for each A_2 sample, and extracting A_2 and c_1 simultaneously (it should be noted that since the W+jets events are reused, the estimated widths at each A_2 values are somewhat correlated). Again, the response in A_2 is less biased when compared to studies with signal only, but yields a smaller signal fraction c_1 of $\approx 45\%$. The smaller signal fraction reflects the poorly reconstructed signal events, since they become even more background-like (higher background probability relative to the total event probability) when compared to the properly reconstructed ones. This increased linearity, however, comes at the expense of the uncertainties

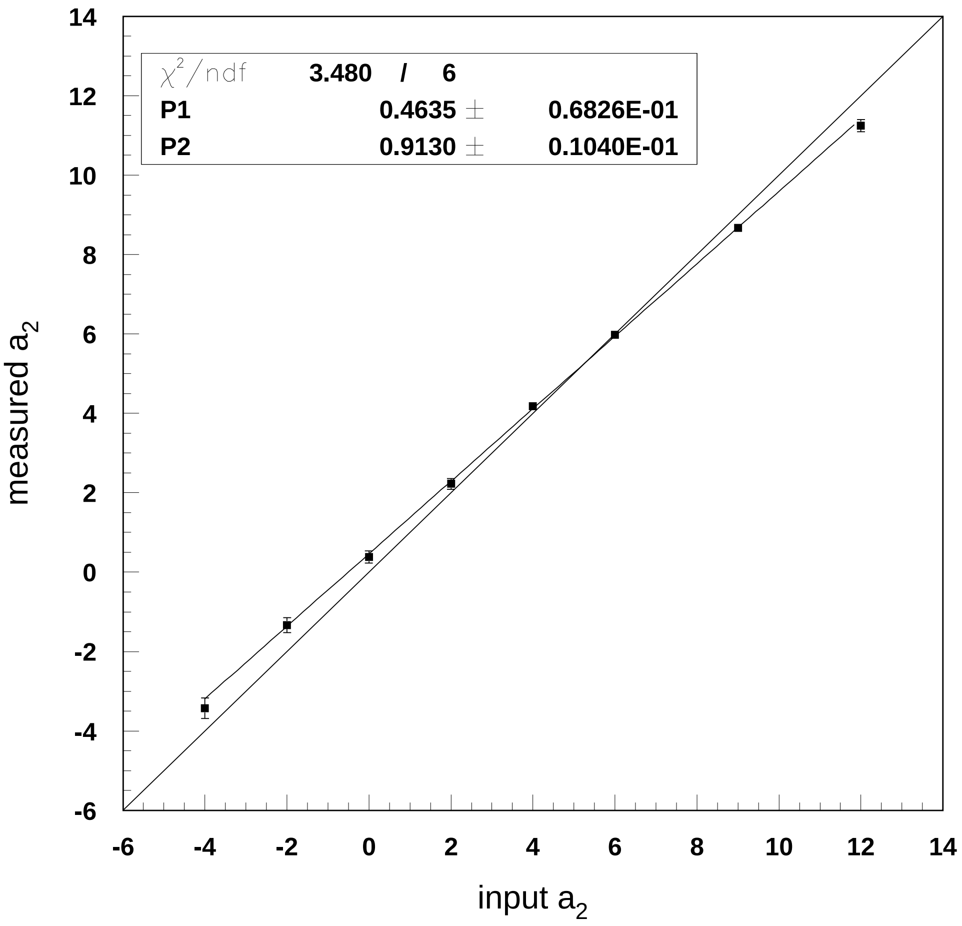

Figure 6.1: Response for single experiments of 4000 pure $t\bar{t}$ events as a function of input A_2. The likelihoods for these experiments use only the probabilities for signal.

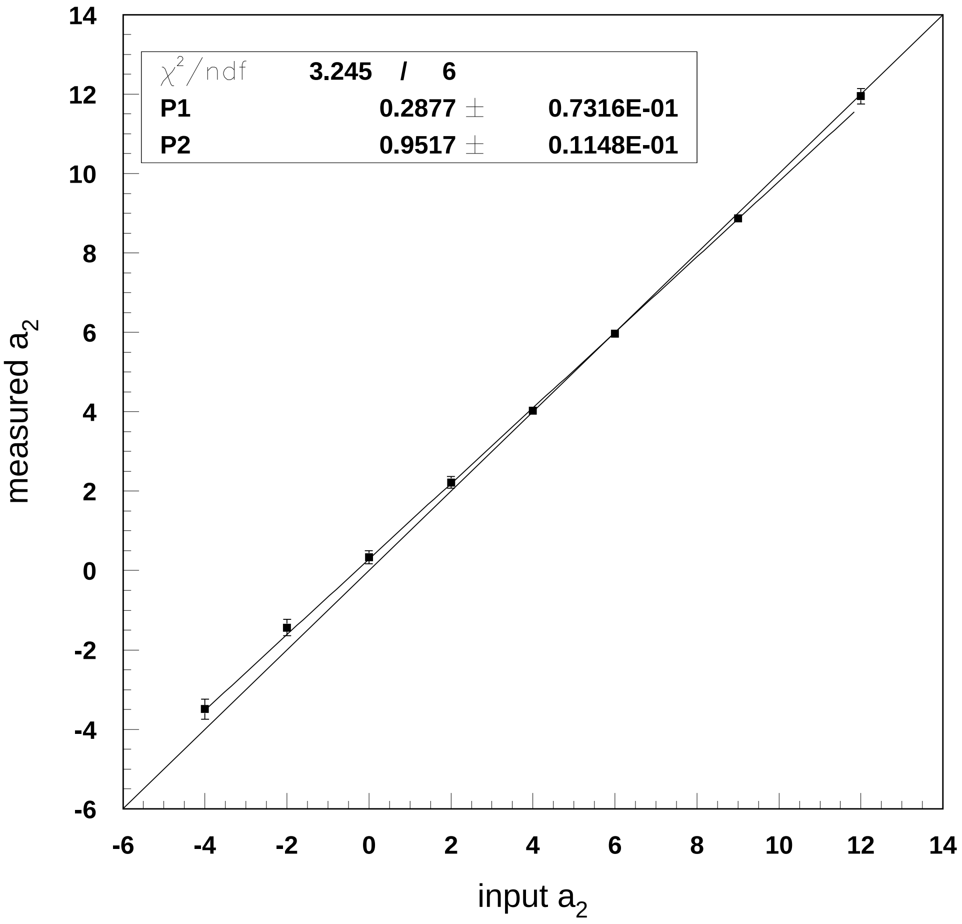

Figure 6.2: Same as Fig. 6.1, but with both signal and background probabilities included in the likelihood calculation in the form $P = c_1 P_{t\bar{t}} + c_2 P_{W+jets}$ for the extraction of A_2.

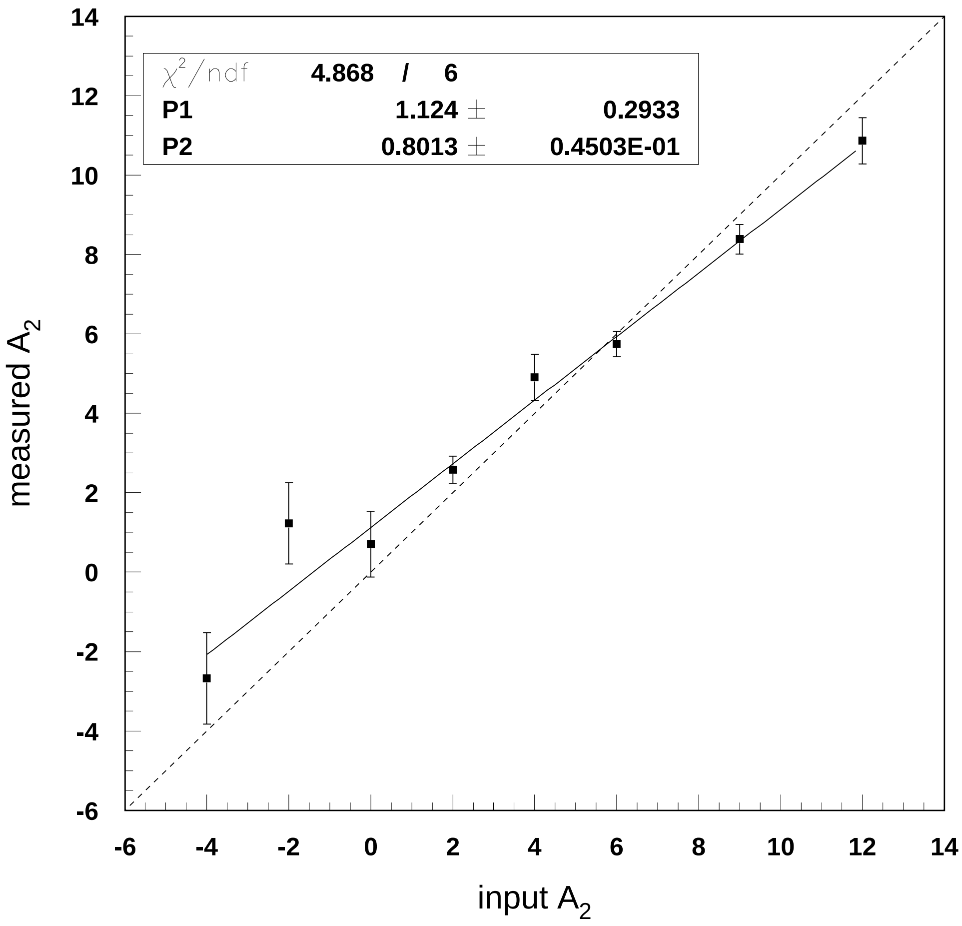

Figure 6.3: Response for 200 experiments of 18 pure $t\bar{t}$ events as a function of input A_2. The likelihoods for these experiments use only the probabilities for signal.

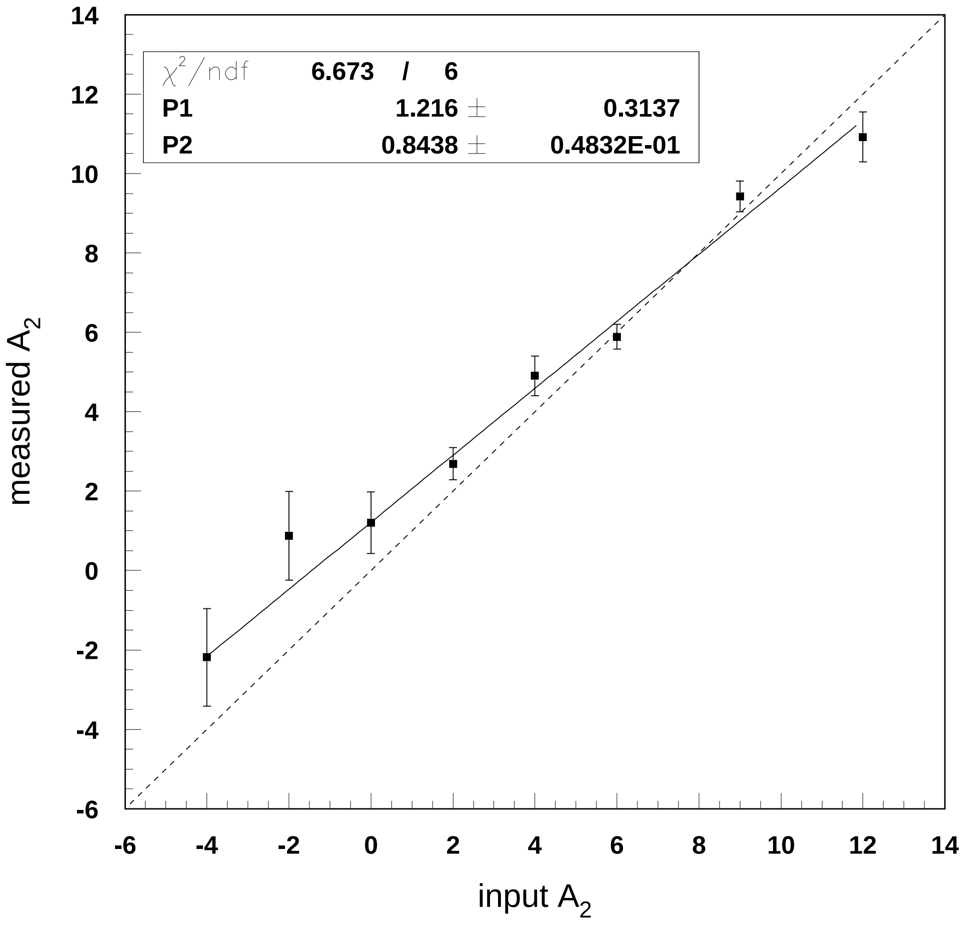

Figure 6.4: Same as Fig. 6.3, but with both signal and background probabilities included in the likelihood calculation in the form $P = c_1 P_{t\bar{t}} + c_2 P_{W+jets}$ for the extraction of A_2.

on the extracted A_2, which were also increased.

For statistics that correspond to our data sample, we perform ensemble tests with experiments of 71 events. We first examine the determination of signal fraction c_1. Figure 6.6 shows the extracted c_1 as a function of input signal fraction for four A_2 values, from 200 experiments each containing a total of 71 events. The linear fits for each A_2 value are consistent with each other, which indicates that there is little correlation between A_2 and c_1 calibrations, as was the case for the smeared MC studies. We therefore first determine the signal fraction in our data sample, and use the linear fits to correct this to the true value. The measured c_1 is 0.23, or $\approx$ 0.25 after correction using any of the 4 linear fits. This corresponds to 18 signal and 53 background events in a sample of 71 total events. We therefore perform ensemble tests for A_2 using experiments that correspond to this composition.

The ensemble distributions of extracted A_2, together with the corresponding estimated uncertainty δ_{A_2}, from experiments consisting of 18 $t\bar{t}$ signal and 53 W+jets background events for each of the A_2 values, are shown in Fig. 6.7 to 6.10. Figure 6.11 shows the response as a function of input A_2 value. (The triangles represents events with an isolated muon ($mu + jets$ events), for which the event probability is calculated by performing an extra integration over the muon energy resolution, as is the case in data.) The result of the linear fit is consistent with the case of no background events. This fit is used to correct the likelihood for data. Applying this to our Monte Carlo experiments, we re-minimize the corrected likelihoods and extract the A_2 and their estimated uncertainties δ_{A_2}, as described in Section 5.2. As a cross-check, we compare the percentage of time the input A_2 value is within the interval $A_2 \pm \delta_{A_2}$, against the expected 68% for one standard deviation uncertainty. The result, as a function of input A_2, is shown in Fig. 6.12. Because the width estimation at the boundary (A_2 = -15 and 25) is less reliable, we do not include

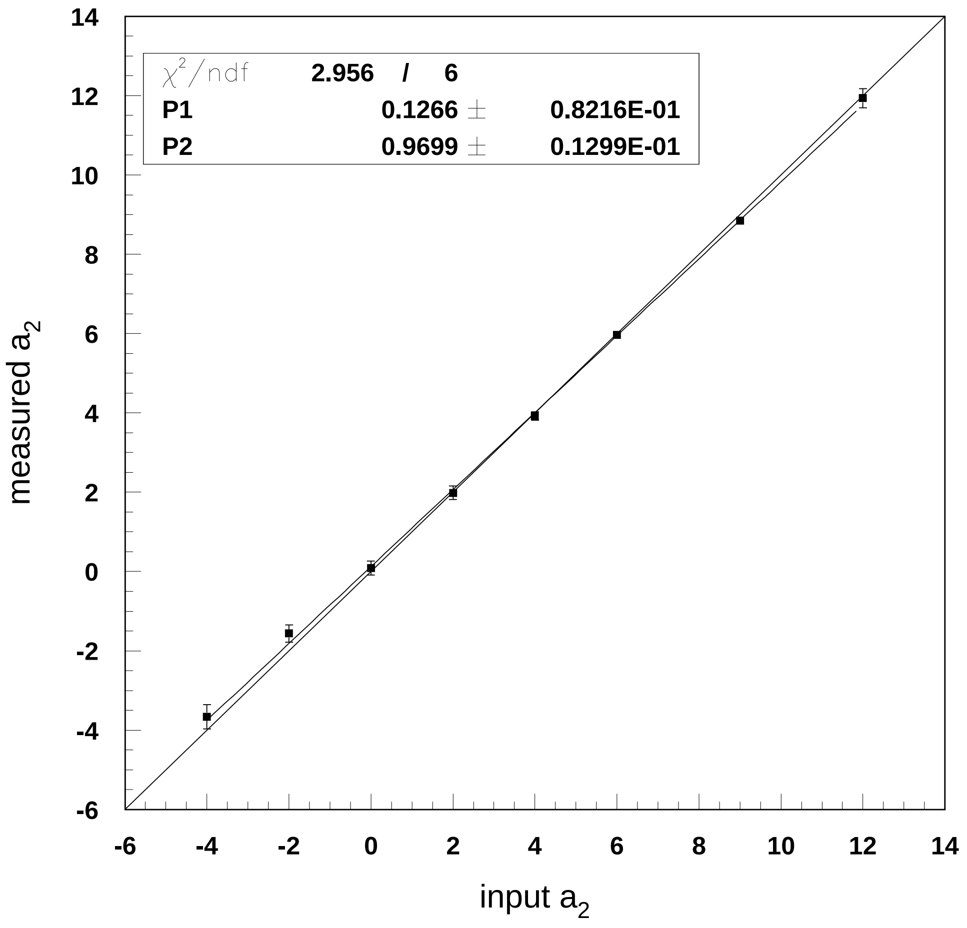

Figure 6.5: Response for single experiments of combinations of 4000 $t\bar{t}$ signal and 4000 W+jets background events.

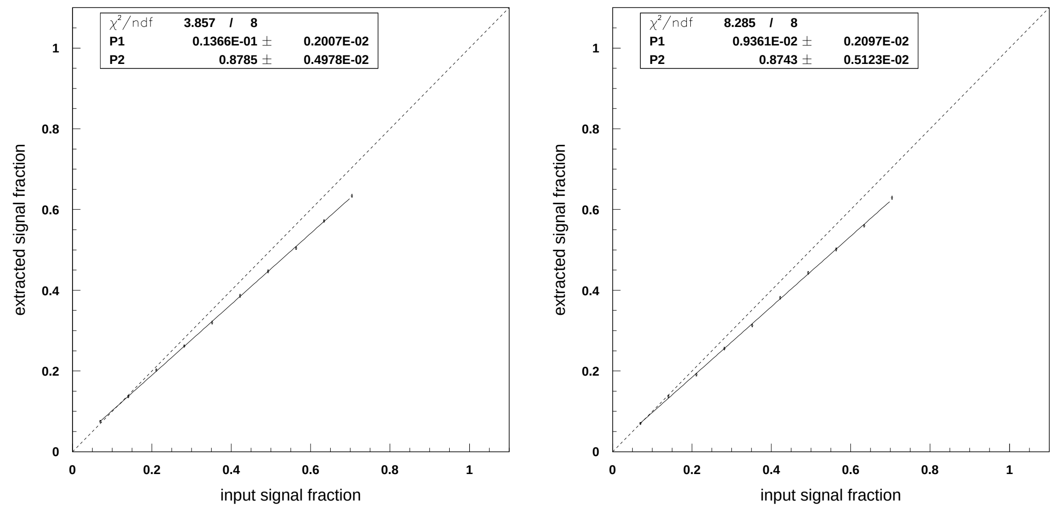

(a) A_2 = -2 (b) $A_2 = 0$

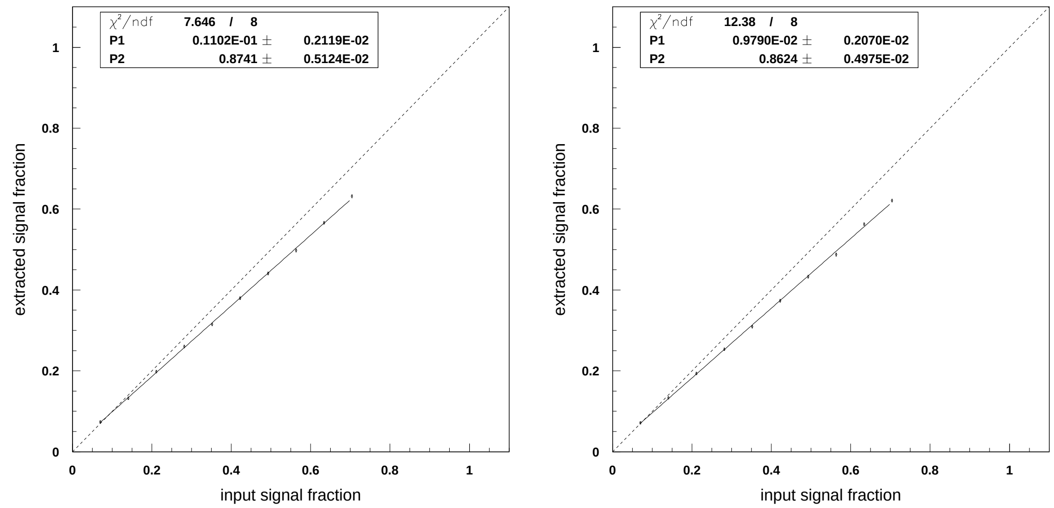

(c) $A_2 = 2$ (d) $A_2 = 4$

Figure 6.6: Extracted signal fraction as a function of signal-background composition, for 200 experiments of 71 events from four different A_2 samples. The solid line is a linear fit to the Monte Carlo data points. The dashed line (diagonal) corresponds to a slope of 1 and no offset.

events that minimize at the boundary in the calculation of the percentage. For large input A_2 values (larger than ≈ 10), as a result of the way the likelihoods are shaped, our δA_2 tend to be overestimations and less reliable. Therefore, we decided if data falls into this region, instead of δA_2 estimation, it would be better to carry out a limit estimation for the A_2 value, as the data sample would most likely be produced with the true A_2 value also in this region.

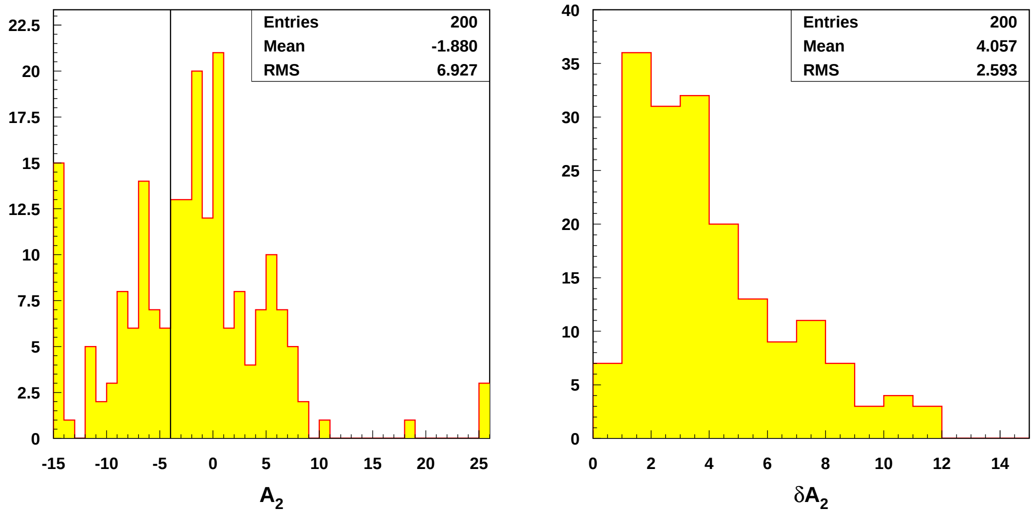

(a) A_2 = -4

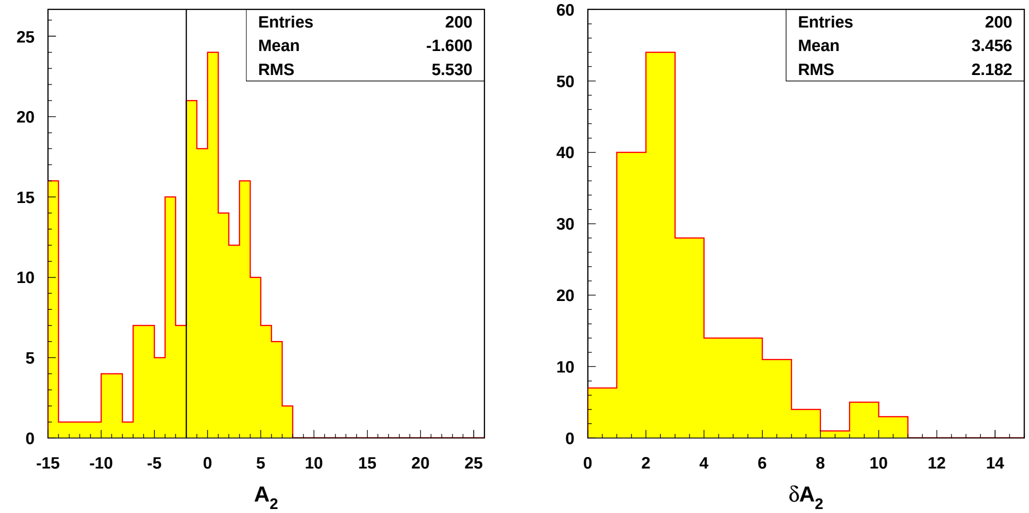

(c) A_2 = -2

Figure 6.7: Ensemble distributions for (a) A_2 = -4 and (b) A_2 = -2. The left plots show the distribution of extracted A_2 and the right plots correspond to the estimated uncertainties for each extracted A_2. The solid lines on the left plots correspond to the input A_2 value.

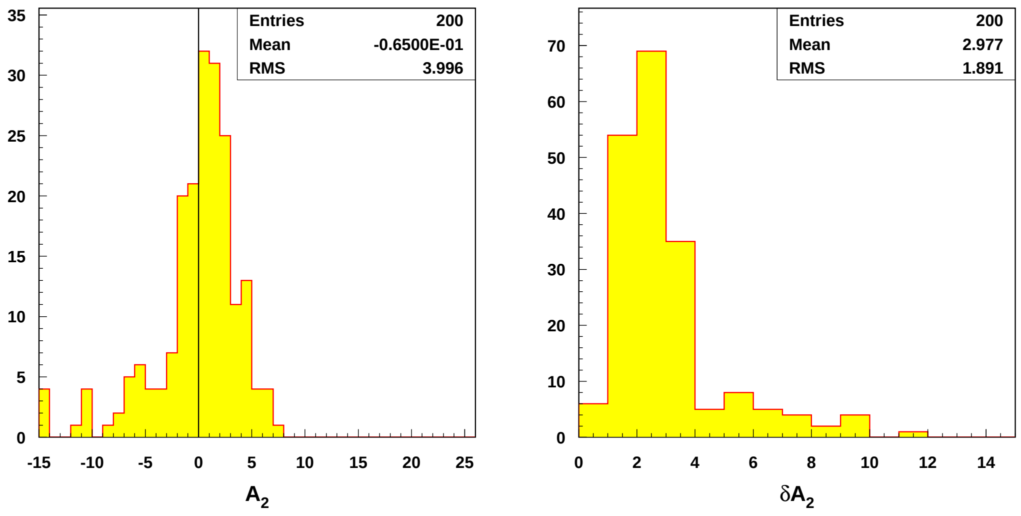

(a) $A_2 = 0$

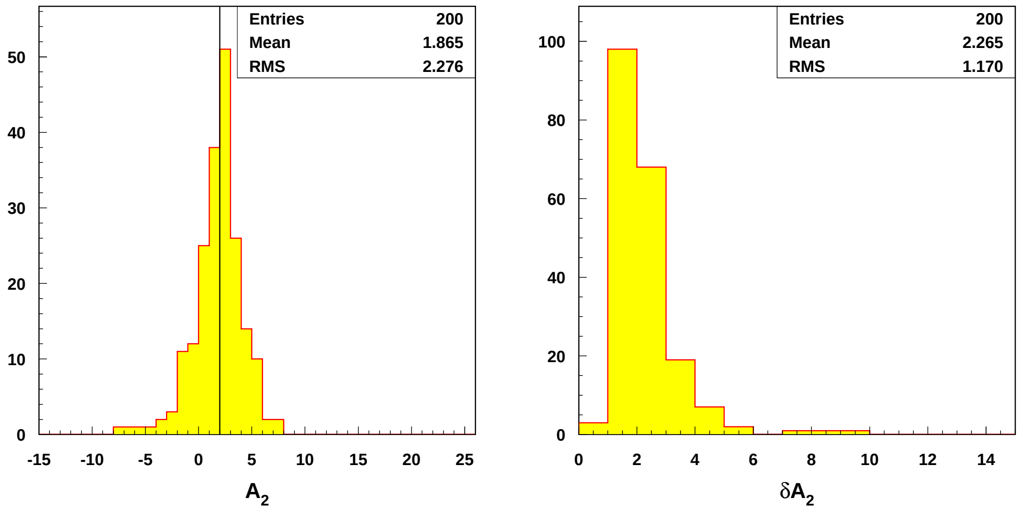

(c) $A_2 = 2$

Figure 6.8: Same as Fig. 6.7 but for (a) $A_2 = 0$ and (b) $A_2 = 2$.

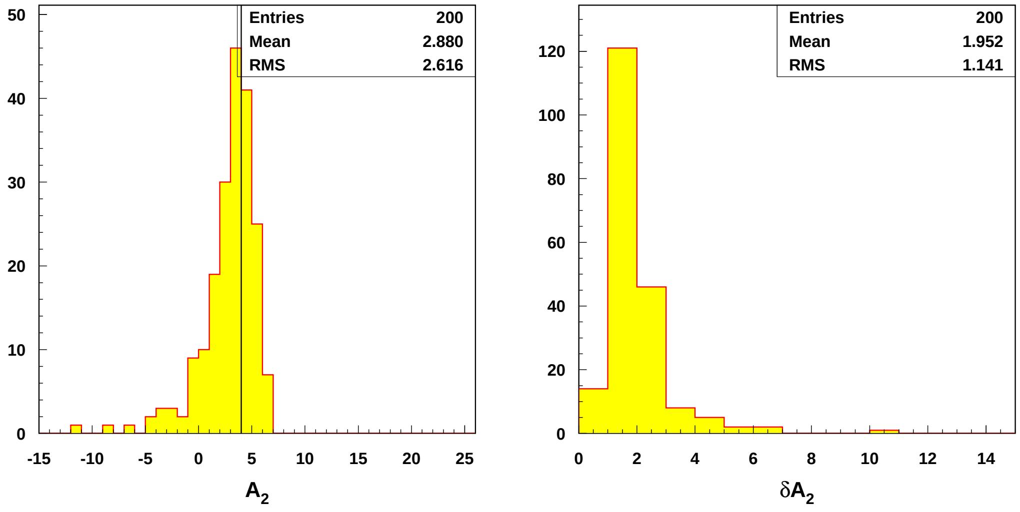

(a) $A_2 = 4$

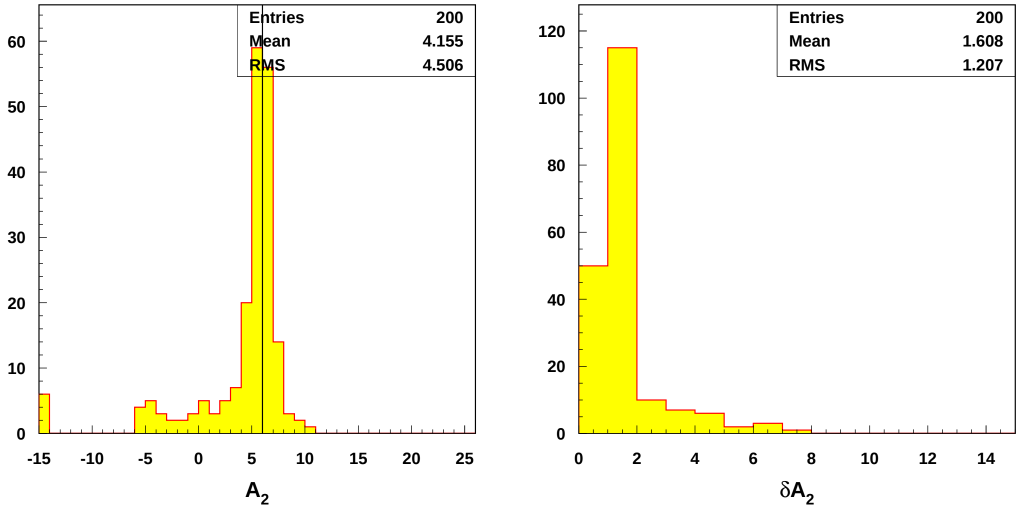

(c) $A_2 = 6$

Figure 6.9: Same as Fig. 6.7 but for (a) $A_2 = 4$ and (b) $A_2 = 6$.

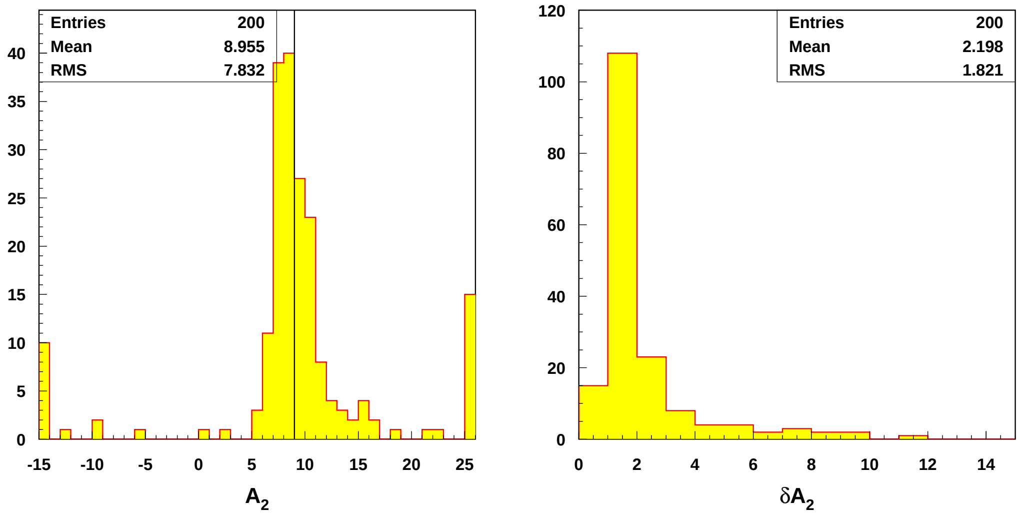

(a) $A_2 = 9$

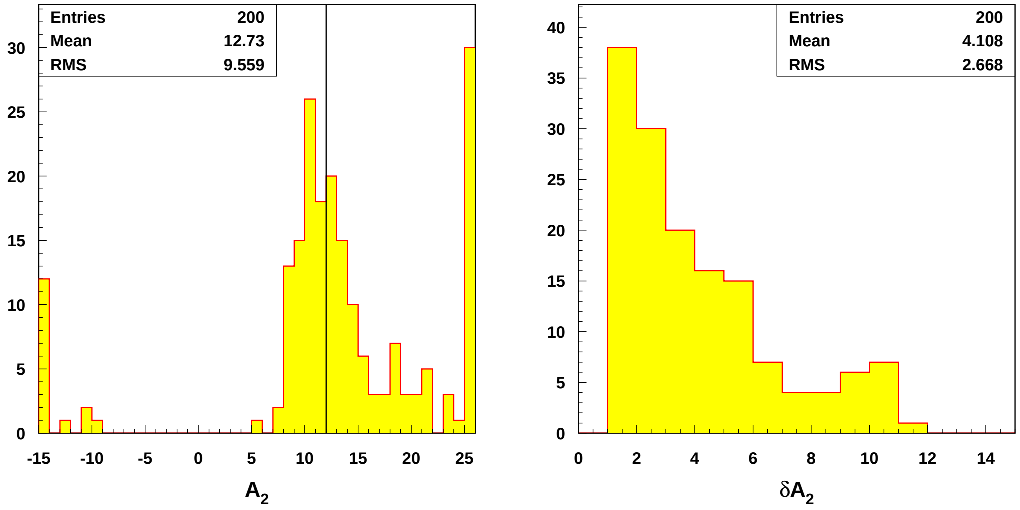

(c) $A_2 = 12$

Figure 6.10: Same as Fig. 6.7 but for (a) $A_2 = 9$ and (b) $A_2 = 12$.

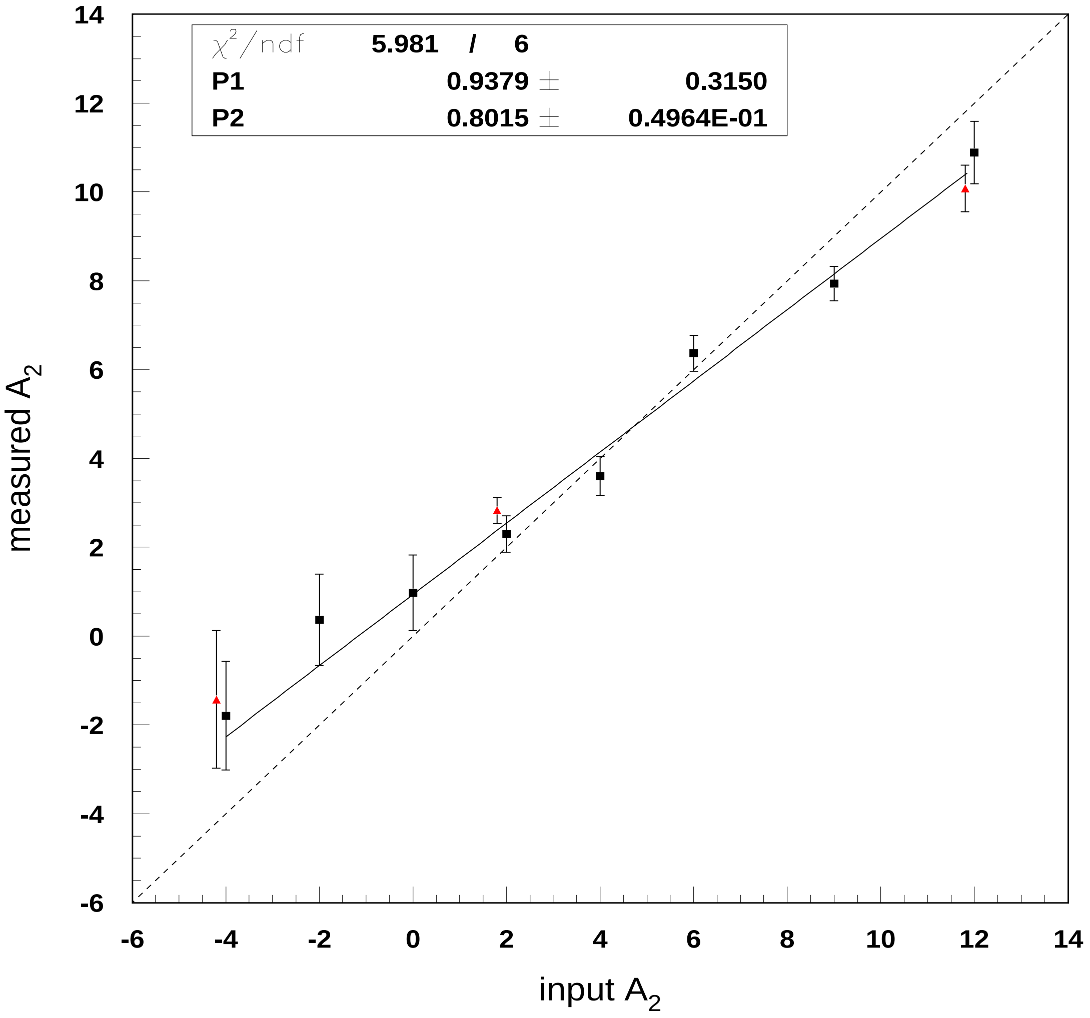

Figure 6.11: Response as a function of input A_2 for ensembles of 200 experiments each consisting of 18 $t\bar{t}$ signal and 53 W+jets background events. The squares, for which the linear fit is based on, represent events containing an electon. The triangles correspond to events with an isolated muon, and are displaced slightly in input A_2 for ease of comparison.

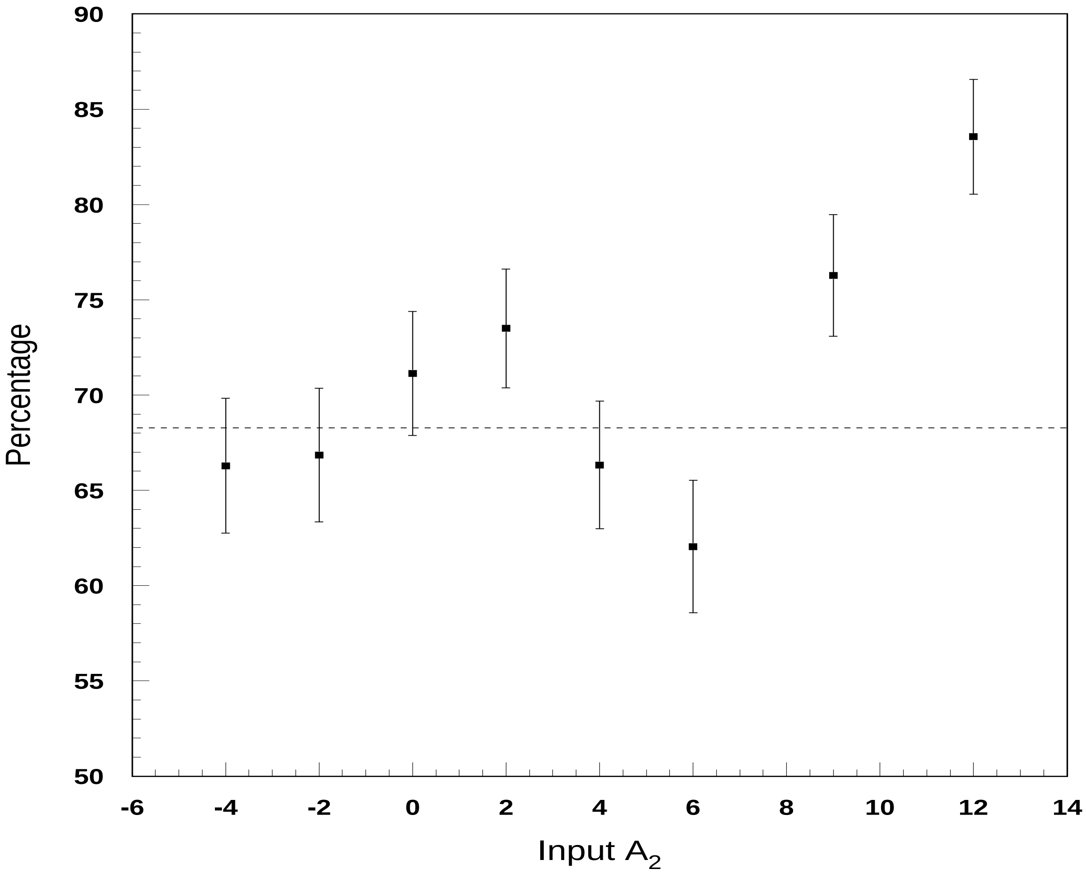

Figure 6.12: Percentage of times (or experiments) that the input A_2 value lies within A_2(extracted)$\pm\delta_{A_2}$, after applying the response correction from Fig. 6.11. The error bars correspond to binomial uncertainties for 200 experiments. The dashed line represent the expected value (68.27%).

Chapter 7

Results of the Analysis

7.1 Extracted Parameters

We now apply the A_2 extraction method to data. Our Run I data sample contains 35 e+jets and 36 μ+jets candidates. For the μ+jets candidates, we perform an additional integration over the muon resolution function (see Section 2.5) instead of assuming a δ-function for the transfer function in calculating event probabilities. We minimize the $-\ln(\mathrm{L})$, simultaneously as a function of A_2 and signal fraction c_1, obtaining the most probable A_2 value of 3.21 ± 1.43. The result is shown in Fig. 7.1. The extracted signal fraction is 0.23, and from the c_1 calibration in Fig. 6.6, this represents a true signal fraction of 0.25, or 18 signal and 53 background in the 71-events sample. Using the A_2 calibration developed in Section 6.4 (Fig. 6.11) to modify/correct the likelihood, we obtain the likelihood distribution in Fig. 7.2. After recalculating the most probable A_2 value and its statistical uncertainty, which takes into account the correlation between A_2 and c_1, our final result is A_2 = 2.84 ± 1.78.

Figure 7.3 shows comparisons between data and expected distributions (from

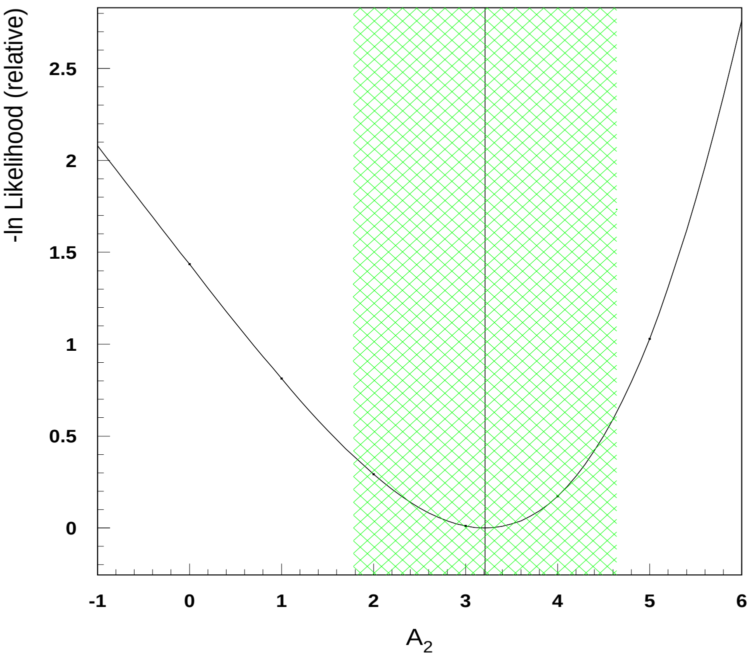

Figure 7.1: –ln(Likelihood) as a function of A_2 for data, before applying the response correction from Fig. 6.11. The most probable value is $A_2 = 3.21$ with an uncertainty of 1.43 (represented by the shaded area).

Monte Carlo) of four physical variables: transverse-momentum (p_T) of the leading-jet, p_T of the lepton, $H_T = \sum E_T^{jet}$, and missing transverse momentum ($\not\!\!E_T$). For the expected distributions, both the total and the separate contributions from the 18 $t\bar{t}$ signal and the 53 W+jets events are shown. A comparison for the background probabilities (P_{W+jets}) is shown in Fig. 7.4. It is clear that the results from Monte Carlo agree well with the data, thereby providing confidence in the extracted parameters.

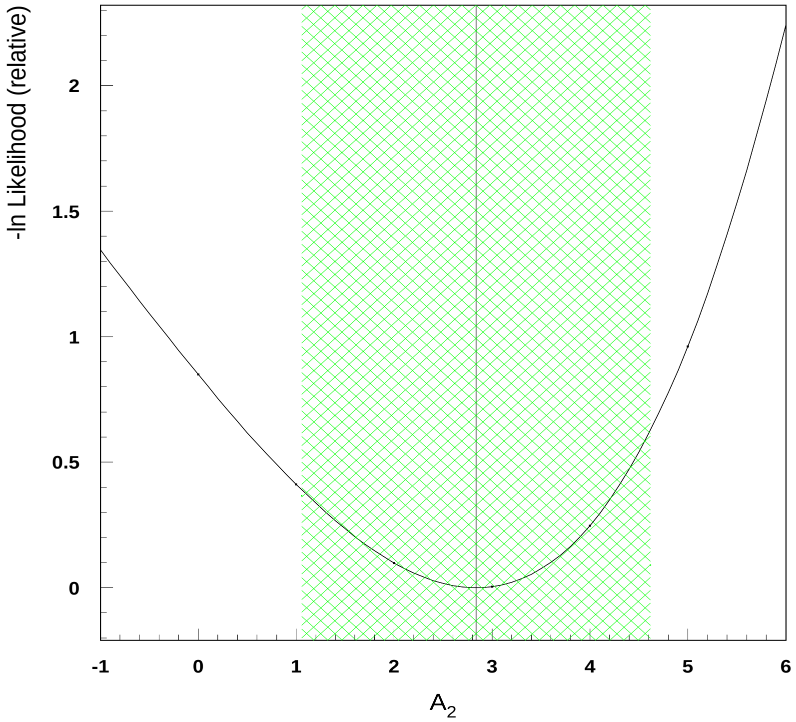

Figure 7.2: –ln(Likelihood) as a function of A_2 for data, after applying the response correction from Fig. 6.11. The most probable value is $A_2 = 2.84$, with an uncertainty of 1.78 (represented by the shaded area).

7.2 Systematic Uncertainties

The uncertainty estimated directly from the likelihood corresponds to only the statistical uncertainty of the analysis. Since our method is calibrated using Monte Carlo events, the uncertainties in certain input assumptions to the Monte Carlo (MC), such as the top mass, can introduce systematic biases in our measurement that are not reflected in the statistical error. The general approach in assessing the effect of such uncertainties is to generate a different sets of MC samples, with input parameters modified by their uncertainties. The changes in the measurement of

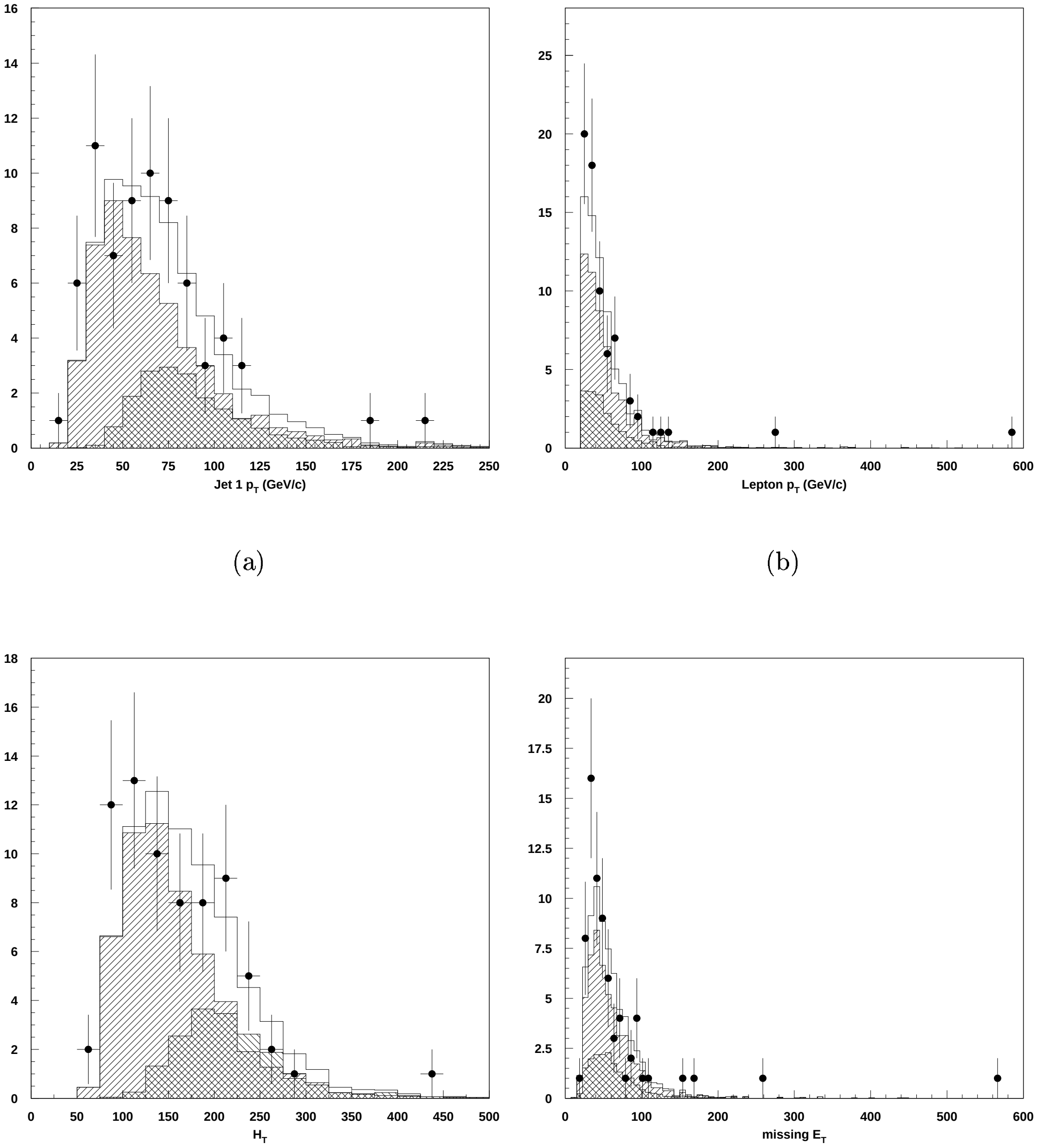

(a) (b)

(c) (d)

Figure 7.3: Distribution in (a) leading-jet p_T, (b) lepton p_T, (c) $H_T = \sum E_T^{jet}$ and (d) $\not{E}_T$, for the 71 $t\bar{t}$ candidates (data points). This is compared to the distribution expected from a sum of MC simulations of 18 $t\bar{t}$ signal and 53 W+jets background events (unshaded histogram). The separate contributions from signal (left-hatched) and background (right-hatched) are also shown.

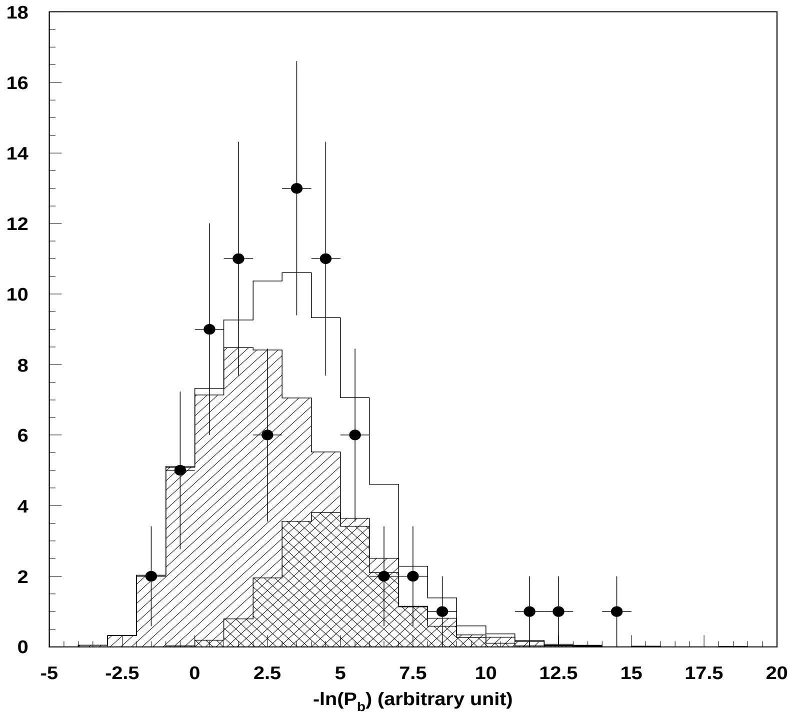

Figure 7.4: Distribution in probability for a background interpretation of the 71 $t\bar{t}$ candidates (data points). This is compared to the distribution expected from a sum of MC simulations of 18 $t\bar{t}$ signal and 53 W+jets background events (unshaded histogram). The separate contributions from signal (left-hatched) and background (right-hatched) are also shown.

A_2 resulting from these alternative calibrations provide estimates of the individual contributions to the overall systematic uncertainty.

The matrix element method used in this analysis allows a different approach for estimating some of the systematic uncertainties. Since the event likelihood derivation starts with the parton-level probabilities, we can vary the assumptions of our Monte Carlo model directly in the likelihood calculation of the data events. The resultant variations on the measurement would provide an estimate of the systematic uncertainty due to the uncertainty on the assumptions.

We discuss below the estimation of the dominant systematic uncertainties in our analysis.

7.2.1 Mass of the Top Quark

To estimate the dependence of A_2 on the value of top mass, we re-analyze the data sample using a different top-mass assumption in the likelihood. The currently accepted value of the top mass is $M_t = 174.3 \pm 5.1$ GeV/c^2 [3]. Figure 7.5 shows the A_2 results for three top-mass assumptions M_t=170, 175, and 180 GeV/c^2. The difference between 170 and 180 GeV/c^2 is 0.84. We therefore assign a systematic uncertainty of $0.84/2 = 0.42$ to our measurement of A_2 from uncertainty in the mass of the top quark.

7.2.2 Jet Energy Scale

The relative jet energy scale between Monte Carlo and data has an estimated uncertainty of ±(2.5%+0.5GeV) [73]. We estimate the effect of this uncertainty on our A_2 measurement by scaling the jet energies in the data sample up and down according to this uncertainty, and then re-extracting A_2. The results are shown in

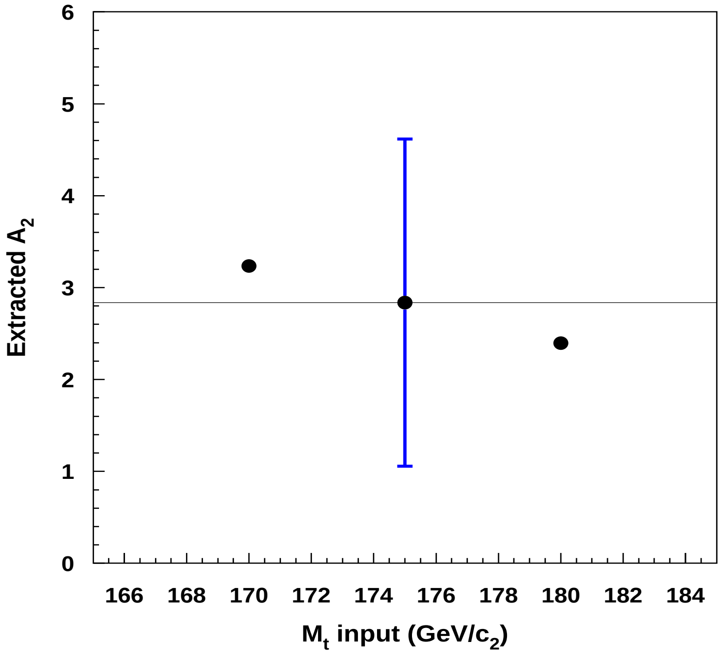

Figure 7.5: Run I data analyzed using different top masses. The horizontal line shows the value of our A_2 measurement and the error bar corresponds to the statistical uncertainty on A_2. The difference in A_2 for the two extreme points is 0.84

Fig. 7.6. The difference in A_2 response between the two extreme jet energy scales gives a systematic uncertainty on A_2 of 0.09.

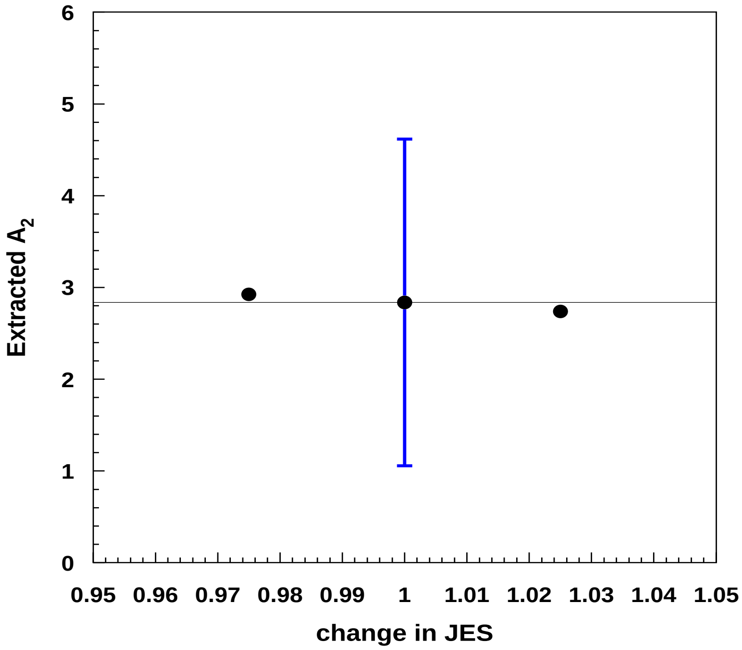

Figure 7.6: Run I data analyzed by changing the jet energies in the events according to the uncertainty on the jet energy scale. The points correspond to changes in jet energies of −(2.5%+0.5GeV), 0, and +(2.5%+0.5GeV). The systematic error on A_2 assigned from this effect is defined by half the difference of the two extreme points, and equals 0.09.

7.2.3 Average Acceptance $\langle A \rangle$

The average acceptance $\langle A \rangle$ is calculated from the Monte Carlo, and its precision is therefore limited by the statistics of the MC samples. We estimate the effect of this statistical uncertainty on our measurement of A_2 by recalculating the average-acceptance function $\langle A(A_2) \rangle$ as follows.

For the A_2 values for which we have Monte Carlo samples, we simply fluctuate the average acceptance N_{acc}/N_{gen} according to a binomial distribution. That is, we choose a new total number of accepted events N'_{acc} based on expected fluctuations in N_{acc}.

For A_2 values not based on separate MC samples (A'_2), as described in Section 4.4, the average acceptance is estimated by reweighting the existing samples, event-by-event, as $[\sum_{i=1}^{N_{acc}} P(x_i, A'_2)/P(x_i, A_2)]/N_{acc}$. Hence, $\langle A(A'_2)\rangle$ depends on the distribution of accepted events in the existing samples, in addition to the total number. Before reweighting, we simulate the fluctuation within the event distribution using Poisson statistics. That is, for each event i, we choose a new number n_i according to a Poisson distribution for an expected value of 1 (since this is the observed number for one event). The new average acceptance is then given by $[\sum_{i=1}^{N_{acc}} n_i P(x_i, A'_2)/P(x_i, A_2)]/N_{acc}$. Finally, the new average acceptance is corrected by the factor $N'_{acc}/(\sum_{i=1}^{N_{acc}} n_i)$ to take into account the effect of binomial fluctuation in the total number of accepted events.

We generated 20 new average acceptance functions $\langle A(A_2)\rangle$ and applied these to our data sample. Figure 7.7 shows the distribution of extracted A_2 values for these acceptance functions. We assign the RMS of that distribution (0.04) as the systematic uncertainty on our A_2 measurment from the uncertainty on acceptance.

7.2.4 Parton Distribution Functions

We used the CTEQ3M parton distribution function (PDF) [36] in our Monte Carlo generation and in the likelihood calculations. These PDFs are based on next-to-leading order QCD theory. Figure 7.8 compares two other PDFs (CTEQ6M and CTEQ6L) to that of CTEQ3M. To estimate the systematic uncertainty on A_2 due to uncertainty on the PDF, we re-analyze the data sample with each of the two PDFs and select the result that shows the larger difference in A_2 from the value

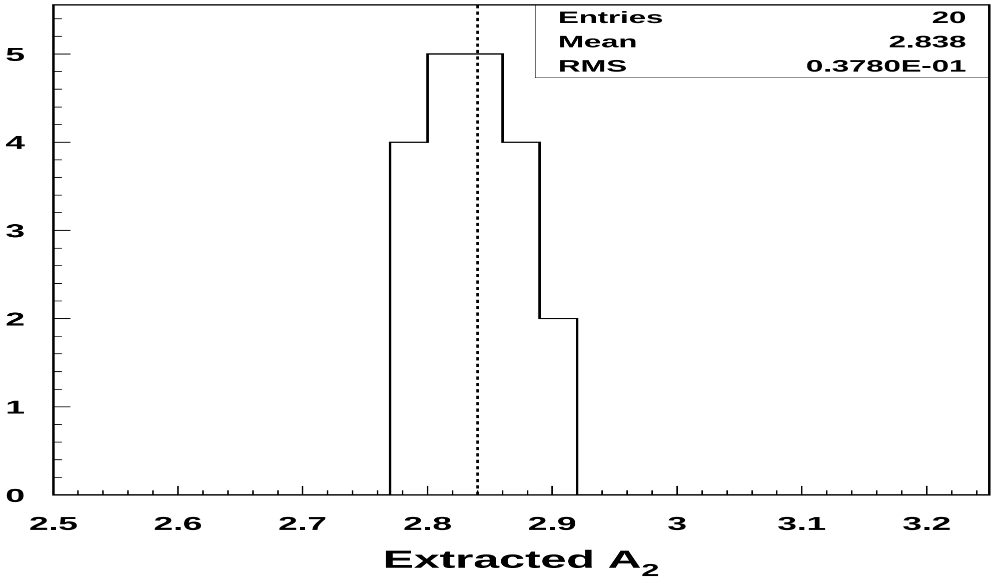

Figure 7.7: Response from data using 20 average acceptance functions obtained by fluctuating the Monte Carlo samples (see text). The dashed line represents our measured A_2 value.

obtained using CTEQ3M. Figure 7.9 shows the -ln(Likelihood) as a function of A_2 for the choices CTEQ3M and CTEQ6L. (Figure 7.9(a) is identical to Fig. 7.2.). The extracted A_2 shows a difference of 0.02, and we assign this to be the systematic uncertainty due to uncertainty on PDFs.

7.2.5 Monte Carlo Calibration

The A_2 calibration applied to data, as shown in Fig. 6.6, is derived from Monte Carlo experiments. As a result, like in the case for average acceptance $\langle A \rangle$, the precision of the calibration is limited by statistics. For each measured A_2, the statistical uncertainties on the calibration constants translate into a systematic uncertainty on the true corrected A_2. Since

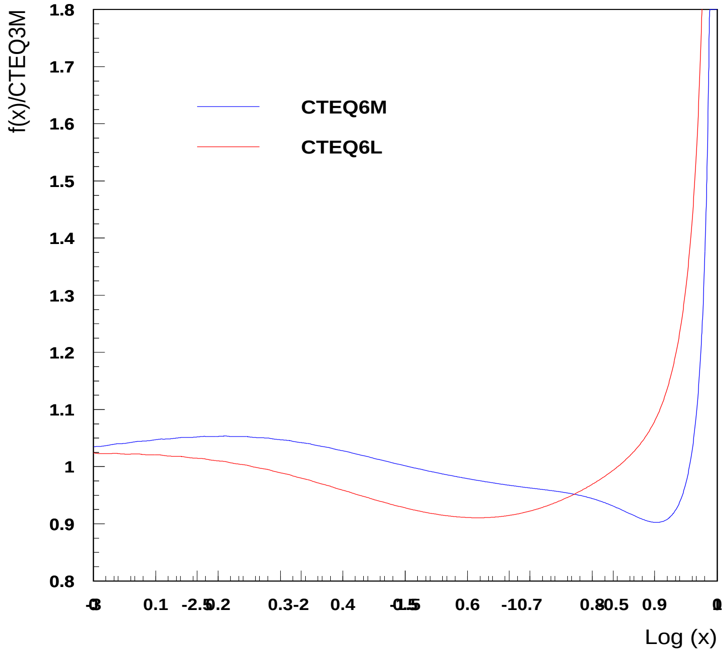

Figure 7.8: Comparison of different PDFs with CTEQ3M, which was used in our analysis

$$A_2(measured) = p_1 + p_2 A_2(true) \quad , \tag{7.1}$$

where p_1 and p_2 are the calibration constants, the uncertainty on $A_2(true)$ is, denoting $x = A_2(true)$ and $y = A_2(measured)$, given by

$$\begin{aligned} \delta x &= \delta(\frac{y - p_1}{p_2}) \\ &= \sqrt{(\delta p_1)^2(\frac{\partial x}{\partial p_1})^2 + (\delta p_2)^2(\frac{\partial x}{\partial p_2})^2 + 2\rho_{p_1 p_2}(\frac{\partial x}{\partial p_1})^2(\frac{\partial x}{\partial p_2})^2 \delta p_1 \delta p_2} \end{aligned} \tag{7.2}$$

where $\rho_{p_1 p_2}$ is the covariance of p_1 and p_2. From Eq. 7.2, the systematic uncertainty

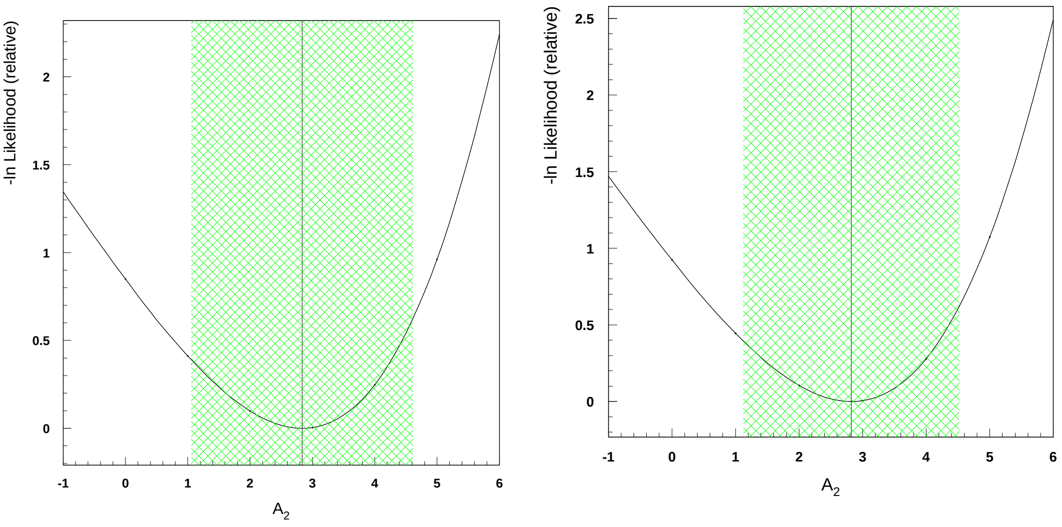

(a) CTEQ3M

(b) CTEQ6L

Figure 7.9: $-\ln$(Likelihood) as a function of A_2 for the data sample, (a) using CTEQ3M and (b) CTEQ6L in the calculation of the likelihoods. The cross-hatched region reflects the statistical uncertainty on each A_2

on the true A_2 due to uncertainty on the Monte Carlo calibration is 0.29.

7.2.6 Model for $t\bar{t}$ Production

Because of the lack of a fundamental description of the fragmentation and hadronization of partons, these processes are generally implemented somewhat differently in different Monte Carlo generators. To assess the effect of the different modelings, we perform ensemble tests using another widely used Monte Carlo generator: HERWIG [80]. Because of the difficulty of generating new Run I Monte Carlo with a different generator, we use the HERWIG Monte Carlo samples that were generated previously for the Run I top-mass analysis [87], which were studied and verified extensively in Run I. The hard process in these samples corresponds to the SM ($A_2 = 0$) "tree-level" matrix element (leading order in QCD), without the inclusion of $t\bar{t}$ spin-correlation. These MC events were passed through the same full DØ simulation and reconstruction process as our PYTHIA events. To provide an appropriate comparison, we also used a Run I PYTHIA sample generated at SM values and containing no spin-correlation between t and $\bar{t}$. While the ideal comparison would be based on samples that are closer to our measured A_2 value, our estimate of systematic error should be comparable. Our contention is supported by the Run I W-boson helicity measurement [77], which is especially sensitive to the production and decay angles of final-state partons, and finds only a small difference between results using these two $t\bar{t}$ models. The large statistical uncertainty of the current data does not warrant the additional studies for finite values of A_2, but this extension of the current analysis would be advisable for the anticipated $\approx$ 70-fold increase in data from Run II. Figures 7.10 and 7.11 shows the ensemble distribution of extracted A_2 and their uncertainties δA_2 for 200 experiments of PYTHIA and HERWIG events, respectively, with each experiment composed of 18 $t\bar{t}$ signal and 53 W+jets background events. The difference between the two estimators of A_2 response (the modes of the distributions) is 0.46, and we assign this as the systematic uncertainty due to different modeling of $t\bar{t}$ production.

7.2.7 Multiple Interactions

The main hard collision can be accompanied by secondary partonic collisions in the same $p\bar{p}$ interaction. Although such secondary interactions tend to be considerably "softer" than $t\bar{t}$ production, they nevertheless add energy to the event.

To estimate the effect of multiple-parton interactions, we generate a PYTHIA Monte Carlo sample at $A_2 = 2$, with multiple interactions switched on, and process

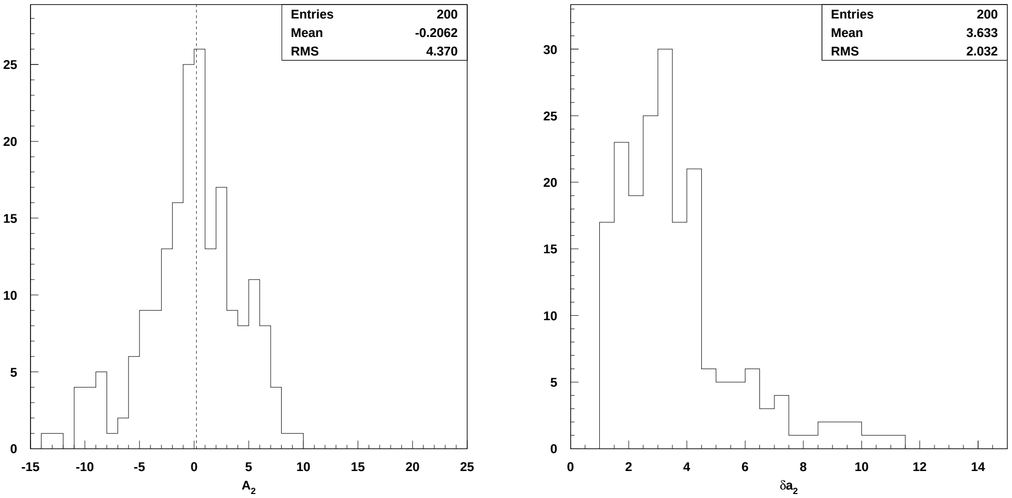

(a) A_2

(b) δA_2

Figure 7.10: Ensemble distributions for A_2 and its uncertainty δA_2 for "experiments" with 18 SM PYTHIA $t\bar{t}$ events and 53 W+jets events. The mode of the distribution is at $A_2 = 0.20$ (dashed line), consistent with the input value for SM of $A_2 = 0$.

the events the same way as our default samples (which were generated without multiple interactions). The ensemble distribution of 200 experiments, each composed of 18 signal and 53 background events, after applying the response correction derived from the default samples, is shown in Fig. 7.12 for the case with multiple interaction switched off, and Fig. 7.13 for multiple interaction switched on. The difference of 0.37 is assigned as the uncertainty on A_2 due to possibility of multiple interactions.

7.2.8 $gg \to t\bar{t}$ Production Process

According to leading-order QCD calculations, at the Tevatron $p\bar{p}$ collision center-of-mass energy of 1.8 TeV in Run I, the $q\bar{q} \to t\bar{t}$ process contributes 90% of the $t\bar{t}$ cross section, with the remaining 10% from the $gg \to t\bar{t}$ process. In our Monte

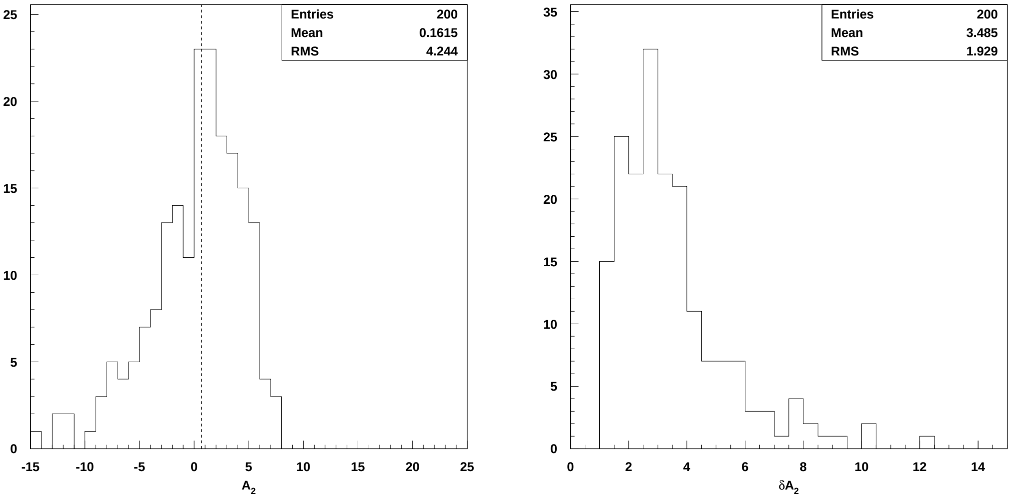

(a) A_2 (b) δA_2

Figure 7.11: Ensemble distributions for A_2 and its uncertainty A_2 for "experiments" with 18 SM HERWIG $t\bar{t}$ events and 53 W+jets events. The mode of the distribution is at A_2 = 0.66 (dashed line).

Carlo samples we included only events from the $q\overline{q} \to t\bar{t}$ process, with corresponding matrix element in the likelihood calculations. The effect of events produced through the $gg \to t\bar{t}$ process is estimated by performing ensemble tests with signal $t\bar{t}$ events from the Monte Carlo sample that corresponds to $A_2 = 0$ and replacing, on average, 10 % of them with $gg \to t\bar{t}$ events. Figure 7.14 and 7.15 show the A_2 distribution of 200 experiments, with only $q\overline{q} \to t\bar{t}$ events, and with $gg \to t\bar{t}$ events included, respectively. The difference of 0.27 in the modes of the distributions is taken as the systematic uncertainty due to $gg \to t\bar{t}$ events.

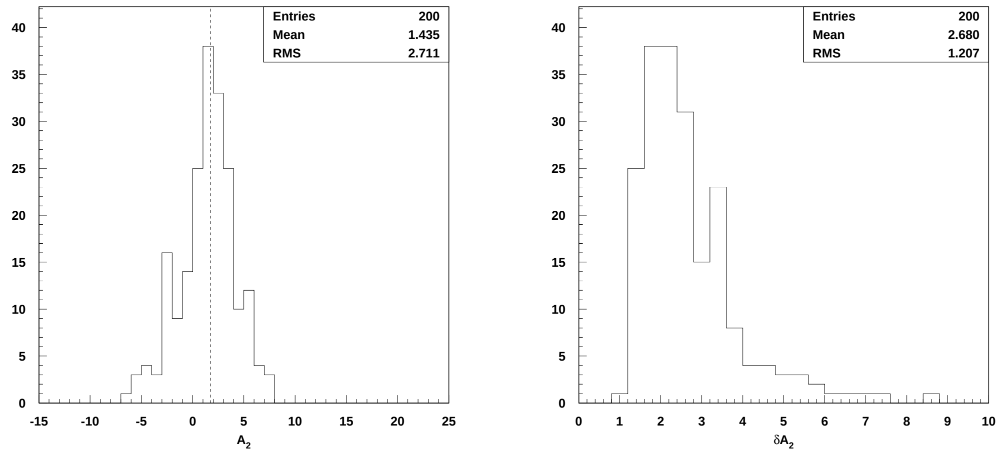

(a) A_2 (b) δA_2

Figure 7.12: Ensemble distribution for A_2 and its uncertainty A_2 for "experiments" with 18 $t\bar{t}$ events ($A_2 = 2$) without multiple interactions and 53 W+jets events. The mode is at $A_2 = 1.75$ (dashed line).

7.2.9 Multijet Background

As mentioned in Section 4.3, according to the previous top analysis [73] , the background in the "precut" data sample consists of 22 ± 5% multijet events. Our requirement that there be exactly 4 jets in an event further reduces the multijet contribution to the background to 20%. Since there is no precise QCD theoretical formulation for the differential cross section for these multijet events, we did not include the multijet contribution in our likelihood calculation but used instead W+jets MC to represent the background. To estimate the effect of the multijet events on our A_2 measurement, we perform ensemble tests in which, on average, 20% of the background consists of multijet data (there are $\approx$ 250 events in our entire selected multijet sample), with $t\bar{t}$ signal consisting of Monte Carlo events corresponding to

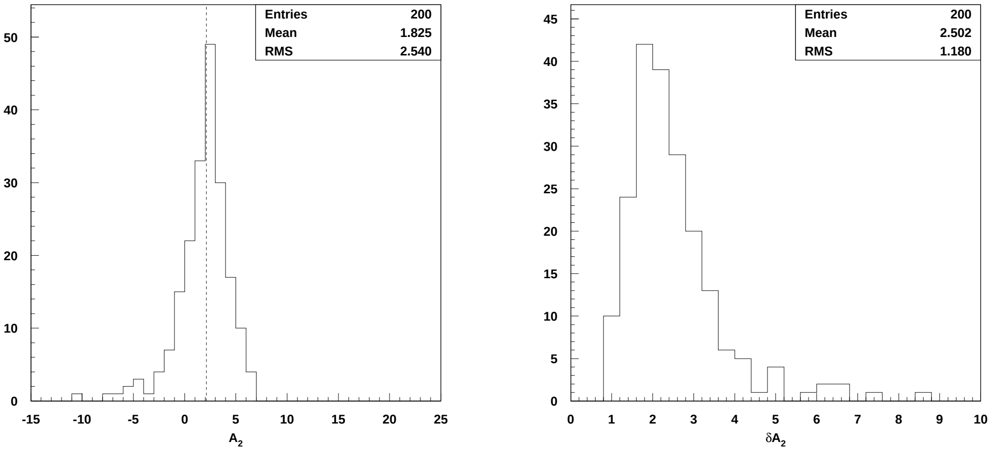

(a) A_2

(b) δA_2

Figure 7.13: Ensemble distribution for A_2 and its uncertainty A_2 for "experiments" with 18 $t\bar{t}$ events ($A_2 = 2$) with multiple interactions and 53 W+jets events. The mode is at $A_2 = 2.13$ (dashed line).

$A_2 = 2$. The result, shown in Fig. 7.16, can be compared to the ensemble test result without multijet events in Fig. 7.12. The difference in the modes of the distributions (0.28) is taken as the systematic uncertainty from mulitjet background.

7.3 Summary of Systematic Uncertainties

A summary of the major systematic uncertainties is shown in Table 7.1. The combined uncertainty is obtained by adding the individual estimates in quadrature. The total systematic uncertainty on A_2 is therefore ± 0.88.

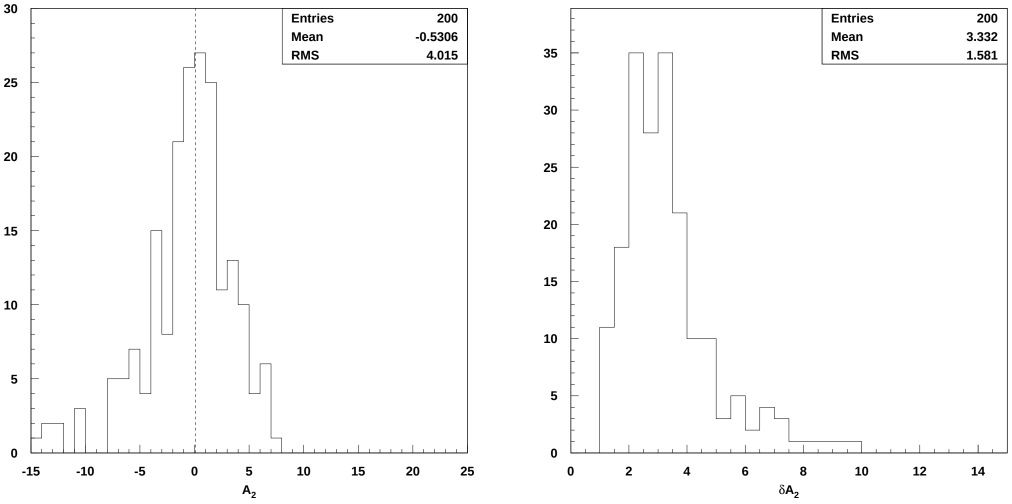

(a) A_2

(b) δA_2

Figure 7.14: Ensemble distribution for experiments with 18 $t\bar{t}$ events (for $A_2 = 0$) and 53 background events. The $t\bar{t}$ events include only those from the $q\bar{q} \to t\bar{t}$ process. The dashed-line represents the mode at $A_2 = 0.1$.

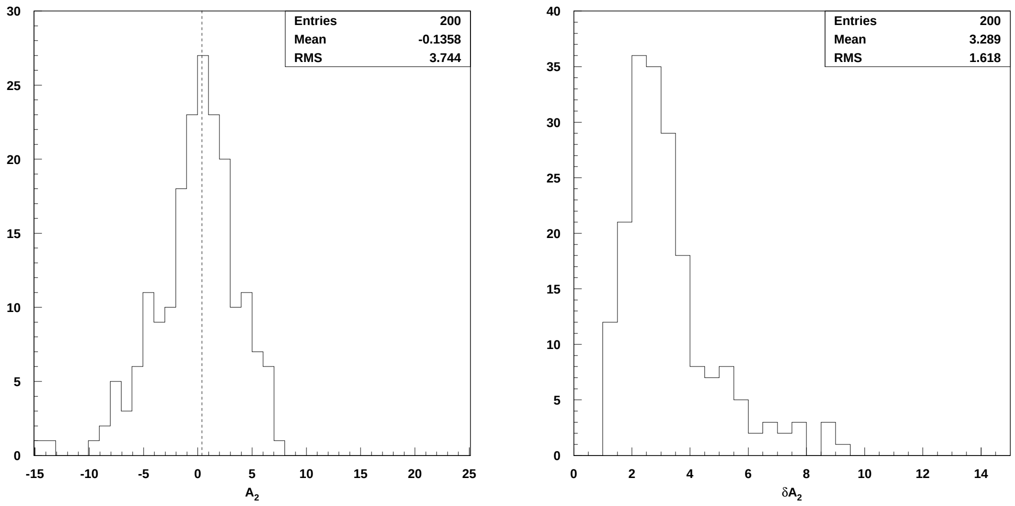

(a) A_2 (b) δA_2

Figure 7.15: Same as Fig. 7.14, except that for the $t\bar{t}$ events on average 90% are from the $q\bar{q} \to t\bar{t}$ and 10% from the $gg \to t\bar{t}$ process. The dashed-line represents the mode at $A_2 = 0.37$.

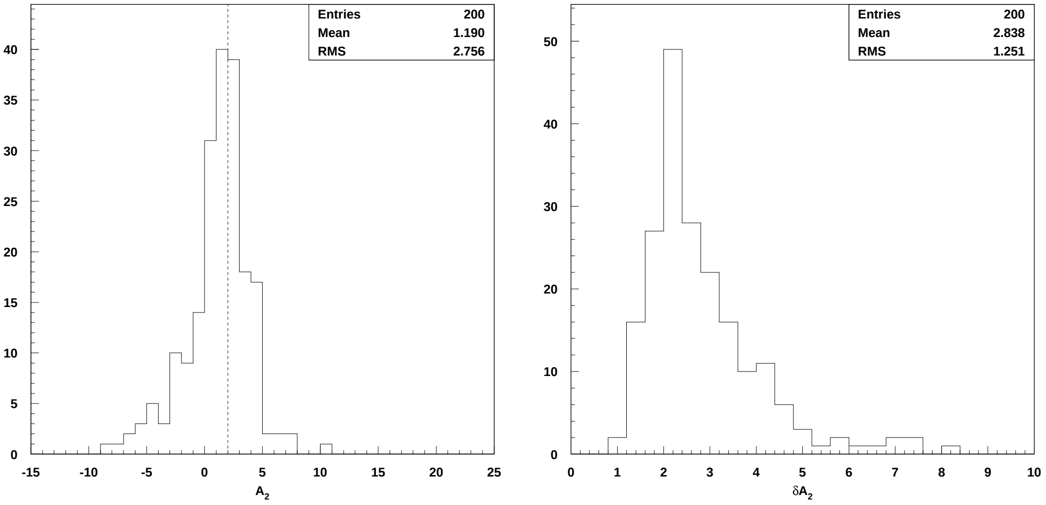

(a) A_2

(b) δA_2

Figure 7.16: Ensemble distribution for experiments with 18 $t\bar{t}$ events (for $A_2 = 2$) and 53 background events. The backgound events contains on average 80% W+jets and 20% multijet events. The dashed-line represents the mode at $A_2 = 2.03$.

Table 7.1: Uncertainties on the measurement of A_2.

Top mass	0.42
Jet energy scale	0.09
Acceptance	0.04
Parton distribution functions	0.02
MC calibration	0.29
$t\bar{t}$ model	0.46
Multiple interactions	0.37
$gg \to t\bar{t}$ process	0.27
Multijet background	0.28
Total	0.88

Chapter 8

Conclusions

With the largest mass of all observed fundamental particles, the top quark provides a promising tool for probing regimes of higher energy and possible new physics. By searching for deviations from the predictions of the SM, the production and decay processes of the top quark can either reveal the presence of new physics or further extend the range of validity of the Standard Model. In this analysis, we used the effective-Lagrangian approach to introduce three non-standard $gt\bar{t}$ couplings (A_1, A_2 and A_3) in the $t\bar{t}$ production process. With A_1 and A_3 maintained at their SM values, we compared the predictions for different A_2 to $t\bar{t}$ data through a matrix-element method. This method utilizes simultaneously all the kinematic information (except unclustered energy) of an event, thereby providing powerful discriminator for non-standard A_2 predictions.

Applying this method to our 71 candidate events from Run I, with an estimated signal/background composition of 18/53, we obtain

$$\boxed{A_2 = 2.84 \pm 1.78(\text{stat}) \pm 0.88(\text{syst})} \tag{8.1}$$

If we combine the statistical and systematic uncertainty in quadradure, the result of 2.84 ± 1.99 is about 1.4 σ away from the Standard-Model value ($A_2 = 0$). This is the first measurement of anomalous coupling at the $t\bar{t}$ production vertex, and is consistent with the SM. With the higher statistics of $t\bar{t}$ events from Run II, it is expected that a more precise measurement can be attained, possibly for all three anomolous couplings extracted simultaneously.

Bibliography

[1] G. L. Kane, *Modern Elementary Particle Physics: The Fundamental Particles and Forces*, (Addison-Wesley, 1993); A. Das and T. Ferbel, *Introduction to Nuclear and Particle Physics* (World Scientific, 2003).

[2] H. Georgi and S. L. Glashow, *Unity of All Elementary-Particle Forces*, Phys. Rev. Lett. **32**, 438 (1974); H. Georgi, H. R. Quinn and S. Weinberg, *Hierarchy of Interactions in Unified Gauge Theories*, Phys. Rev. Lett. **33**, 451 (1974).

[3] S. Eidelman *et al.* (Particle Data Group), *Review of Particle Physics*, Phys. Lett. B **592**, 1 (2004).

[4] G. 't Hooft *et al.*, *A Theory Of Everything?*, Nature **433**, 257 (2005); J. R. Ellis, *The Superstring: Theory of Everything, Or of Nothing?*, Nature **323**, 595 (1986); J. R. Gribbin, *The Search for Superstrings, Symmetry, and the Theory of Everything* (Little, Brown & Company, 2000).

[5] M. Maltoni, T. Schwetz, M. A. Tórtola, and J. W. F. Valle, *Status of global fits to neutrino oscillations*, New J. Phys. **6**, 122 (2004), and references therein.

[6] M. M. Nieto and R. J. Hughes, *Antimatter: Its History and its Properties*, in Proceedings of the Workshop on Antiproton Science and Technology, Santa

Monica, Calif., October 1987; J. R. Ellis, *Antimatter Matters*, Nature **424**, 631 (2003)

[7] M. E. Peskin and D. V. Schroeder, *Introduction to Quantum Field Theory* (Addison-Wesley, Reading, 1995); M. Kaku, *Quantum Field Theory: a Modern Introduction* (Oxford University Press, New York, 1993).

[8] G. 't Hooft, *Gauge Theory and Renormalization*, Presented at International Conference on the History of Original Ideas and Basic Discoveries in Particle Physics, Erice, Italy, 29 Jul - 4 Aug 1994; hep-th/9410038.

[9] G 't Hooft and M. Veltman, *Regularization and Renormalization of Gauge Fields,*, Nucl. Phys. **B44**, 189 (1972).

[10] C. Quigg, *Gauge Theories of the Strong, Weak and Electromagnetic Interactions* (Addison-Wesley, Reading, 1997); I. J. R. Aitchison and A. J. G. Hey, *Gauge Theories in Particle Physics, Vol. 1 & 2* (Institute of Physics Publishing, 2002 & 2004).

[11] E. Noether, "Invariante Variationsprobleme", Nach. kgl. Ges. Wiss. Göttingen 235-257 (1918); D. L. Karatas and K. L. Kowalski, *Noether's Theorem for Local Gauge Transformations* Am. J. Phys. **58**, 123 (1990).

[12] G 't Hooft, *Gauge theories of the forces between elementary particles*, Scientific American 242 6, 104-138 (1980).

[13] R. P. Feynman, *QED: the Strange Theory of Light and Matter* (Princeton University Press, Princeton, 1986).

[14] R. K. Ellis, *QCD and Collider Physics* (Cambridge University Press, Cambridge, 1996).

[15] D. Robson, *A Basic Guide for the Glueball Spotter*, Nucl. Phys. **B130**, 328 (1977); G. B. West, *The Glueball: The Fundamental Particle of Nonperturbative QCD*, Talk given at 3rd AUP Workshop on QCD: Collisions, Confinement, and Chaos, Paris, France, 3-8 Jun 1996. hep-ph/9608258; K. K. Seth, *Present Status of Glueball Searches*, Nucl. Phys. **A675**, 25c (2000).

[16] D. J. Gross and F. Wilczek, *Asymptotically Free Gauge Theories*, Phys. Rev. Lett. **30**, 1343 (1973); G. Altarelli and G. Parisi, *Asymptotic Freedom in Parton Language*, Nucl. Phys. **B126**, 298 (1977).

[17] K. G. Wilson, *Confinement of Quarks*, Phys. Rev. D **10**, 2445 (1974).

[18] B. Andersson, G. Gustafan, G. Ingelman and T. Sjöstrand *Parton Fragmentation and String Dynamics*, Phys. Rept. **97**, 31 (1983).

[19] E. Fermi, *An Attempt of a Theory of Beta Radiation.1*, Nuovo Cimento **11**, 1 (1934); Z. Phys. **88**, 161 (1934); R. P. Feynman and M. Gell-Mann, *Theory of Fermi Interaction*, Phys. Rev. 109, 193 (1958); R.E. Marshak and E. C. G. Sudarshan, *Chirality Invariance and the Universal Fermi Interaction*, Phys. Rev. **109**, 1860 (1958); N. Cabibbo, *Unitary Symmetry and Leptonic Decays*, Phys. Rev. Lett. **10**, 531 (1963).

[20] P. W. Higgs, *Broken Symmetries, Massless Particles and Gauge Fields*, Phys. Lett. **12**, 132 (1964); L. Susskind, *Dynamics of Spontaneous Symmetry Breaking in the Weinberg-Salam Theory.* Phys. Rev. D **20**, 2619 (1979).

[21] S. L. Glashow, *Partial Symmetries of Weak Interactions*, Nucl. Phys. **22**, 579 (1961); S. Weinberg, *A Model of Leptons*, Phys. Rev. Lett. **19**, 1264 (1967); A. Salam, in *Elementary Particle Theory*, N. Svartholm (Almqvist and Wiksell,

Stockholm, 1969), p.367; S. L. Glashow, J. Iliopoulos, and L. Maiani, *Weak Interactions with Lepton-Hadron Symmetry*, Phys. Rev. D **2**, 1285 (1970).

[22] P. Langacker, *Precision Tests of the Standard Electroweak Model* (World Scientific, Singapore, 1995); G. Altarelli and M. W. Grunewald, *Precision Electroweak Tests of the Standard Model*, Phys. Rept. **403**, 189 (2004); hep-ph/0404165; LEP Collaborations, *A Combination of Preliminary Electroweak Measurements and Constraints on the Standard Model*, hep-ex/0412015.

[23] S. D. Ellis, Z. Kunszt, and D. E. Soper, *One-Jet Inclusive Cross Section at Order α_s^3: Quarks and Gluons*, Phys. Rev. Lett. **64**, 2121 (1990); B. Abbott *et al.*, *Inclusive Jet Production in $p\overline{p}$ Collisions*, Phys. Rev. Lett. **86**, 1707 (2001); The QCD/SM Working Group Summary Report, hep-ex/0403100.

[24] C. Quigg, *Beyond the Standard Model in Many Directions*, hep-ph/0404228.

[25] B. Abbott *et al.* (DØ Collaboration), *Observation of the Top Quark*, Phys. Rev. Lett. **74**, 2632 (1995).

[26] F. Abe *et al.* (CDF Collaboration), *Observation of Top Quark Production in $p\overline{p}$ Collisions*, Phys. Rev. Lett. **74**, 2626 (1995).

[27] The CDF Collaboration, the DØ Collaboration, and the Tevatron Electroweak Working Group, *Combination of CDF and DØ Results on the Top-Quark Mass*, hep-ex/0507091.

[28] M. Kobayashi and T. Maskawa, *CP Violation in The Renormalizable Theory of Weak Interaction*, Prog. Theor. Phys. **49**, 652 (1973); L. Wolfenstein, *Parametrization of the Kobayashi-Maskawa Matrix*. Phys. Rev. Lett. **51**, 1945 (1983).

[29] V. Abazov *et al.* (DØ Collaboration), $t\bar{t}$ *Production Cross Section in* $p\bar{p}$ *Collisions at* $\sqrt{s}$*=1.8 TeV*, Phys. Rev. D **67**, 012004 (2003), and references [32] - [50] therein.

[30] I. Bigi and H. Krasemann, *Weak Decays of Heavy Vector Mesons Toponium and Open Top*, Z. Phys. C **7**, 127 (1981); J. H. Kühn, *Weak Interactions of Quarkonia*, Acta Phys. Polon. B **12** 347 (1981); Act. Phys. Austr. Suppl. **XXIV**, 203 (1982); I. Y. Bigi, Y. L. Dokshitzer, V.A. Khoze, J. H. Kühn, and P. M. Zerwas, *Production and Decay Properties of Ultraheavy Quarks*, Phys. Lett. B **181**, 157 (1986).

[31] W. Buchmuller and D. Wyler, *Effective Lagrangian Analysis of New Interactions and Flavor Conservation*, Nucl. Phys **B268**, 621 (1986).

[32] K. Hikasa, K. Whisnant, J.-M. Yang, and B.-L. Young, *Probing Anomalous Top Quark Interactions at the Fermilab Tevatron Collider*, Phys. Rev. D **58**, 114003 (1998).

[33] T. Stelzer, W. F. Long, *Automatic Generation of Tree Level Helicity Amplitudes*, Phys. Commun. **81** 357 (1994).

[34] A. Juste (private communication).

[35] H. Murayama, I. Watanabe, and K. Hagiwara, *HELAS: HELicity Amplitude Subroutines for Feynman Diagram Evaluations*, KEK Report 91-11 (1991)

[36] H. L. Lai, J. Botts, J. Huston, J. G. Morfin, J. F. Owens, J. W. Qiu, W. K. Tung, H. Weerts, *Global QCD Analysis and the CTEQ Parton Distribution*, Phys. Rev. D **51**, 4763 (1995)

[37] G. Mahlon and S. J. Parke, *Maximizing Spin Correlations in Top Quark Pair Production at the Tevatron*, Phys. Lett. B **411**, 133 (1997)

[38] Leon M. Lederman, *The Tevatron*, Scientific American, **264(3)**, 48, 1991.

[39] Helen T. Edwards, Ann. Rev. Nucl. Part. Sci., **35**, 605, 1985.

[40] FNAL, *Design Report Tevatron I projects*, FNAL internal note, 1984 (unpublished).

[41] FNAL, *A Report of the Design of the Fermi National Accelerator Laboratory Superconducting Accelerator*, FNAL internal note, 1979 (unpublished).

[42] S. Abachi *et al.* (DØ Collaboration), *The DØ Detector*, Nucl. Inst. Methods **A338**, 185 (1994).

[43] M. P. Church and J. P. Mariner, Ann. Rev. Nucl. Part. Sci. **43**, 253, 1993.

[44] D. Mohl, G. Petrucci, L. Thorndahl, and S. van der Merr, *Physics and Technique of Stochastic Cooling*, Phys. Rep. **C58**, 73, 1980.

[45] P. Rice-Evans, *Spark, Streamer, Proportional and Drift Chambers*, (The Richelieu Press, London, 1974), Chap. 10.

[46] F. Sauli, CERN Report 77-09, 1977 (unpublished).

[47] F. Sauli, *Principles of Operation of Multiwire Proportional and Drift Chambers*, in *Experimental Techniques in High Energy Physics*, edited by T. Ferbel (Addison-Wesley, 1987), p.79.

[48] A.R. Clark *et al.*, *DØ vertex drift chamber construction and test results*, Nucl. Instrum. Methods **315**, 193 (1992).

[49] A.R. Clark *et al.*, *The central tracking detectors for DØ*, Nucl. Inst. Meth. **279**, 243 (1989).

[50] R. Avery *et al.*, *Performance of the forward drift chambers for the DØ detector*, IEEE Trans. Nucl. Sci. **NS-40**, 573 (1993).

[51] J. F. Detoeuf *et al.*, *The DØ Transition Radiation Detector*, Nucl. Instrum. Methods **A265**, 157 (1988); **A265**, 310 (1989).

[52] C. Fabjan, *Calorimetry in High-Energy Physics*, in *Experimental Techniques in High Energy Physics*, edited by T. Ferbel (Addison-Wesley, Reading, 1987).

[53] B. Rossi, *High Energy Particles* (Prentice-Hall, Inc., Englewood Cliffs, NJ, 1952).

[54] S. J. Wimpenny *et al.*, *The hadron and electron Response of uranium/liquid argon calorimeter modules for the D-Zero detector*, Nucl. Inst. Meth. **A279**, 107 (1989).

[55] M. Abolins *et al.*, *Hadron and electron response of uranium/liquid argon calorimeter modules for the DØ detector*, Nucl. Inst. Meth. **A280**, 36 (1989).

[56] C. Gerber *et al.*, *Muon Momentum Determination*, DØ Note 2140, 1994 (unpublished).

[57] B. Abbott *et al.* (DØ Collaboration), *Studies of WW and WZ production and limits on anomalous WW gamma and WWZ couplings*, Phys. Rev. D **60**, 072002 (1999).

[58] M. Abolins *et al.*, *A high luminosity trigger design for the Tevatron collider experiment in DØ*, IEEE Trans. Nucl. Sci., **36(1)**, 384, 1989.

[59] M. Abolins, D. Edmunds, P. Laurens and B. Pi, *The fast trigger for the DØ experiment*, Nucl. Inst. Meth., **A289** 543, 1990.

[60] M. Abolins *et al.*, *The Level One Framework*, DØ Note 328, 1986; DØ Note 705, 1988 (unpublished).

[61] D. Cutts *et al.*, *Operation of the DØ Data Acquisition System; the new generation*, in Proceedings of the Conference on Computing in High-Energy Physics, Tsukuba, Japan, March 1991.

[62] J. T. Linnemann *et al.*, *The DØ Software Trigger*, in Proceedings of the Conference on Computing in High-Energy Physics, Annecy, France, 1992.

[63] A. Para *et al.*, *The DØ Offline Production and Analysis*, in Proceedings of the Conference on Computing in High-Energy Physics, Annecy, France, 1992.

[64] M. Narain, *Electron Identification in the DØ Detector*, in *The Fermilab Meeting: DPF 92***2**, edited by C. H. Albright *et al.* (World Scientific, 1992), p. 1678.

[65] M. Narain, *Electron Identification in the DØ Detector*, DØ note 1584, 1992 (unpublished).

[66] P. D. Acton *et al.* (OPAL Collaboration), *Studies of Strong and Electroweak Interactions Using Final State Photon Emission in Hadronic Z^0 Decays*, Z. Phys. C **58**, 405 (1993).

[67] D. Buskulic *et al.* (ALEPH Collaboration), *Measurement of Prompt Photon Production in Hadronic Z Decays*, Z. Phys. C **57**, 17 (1992).

[68] P. Abreu *et al.* (DELPHI Collaboration), *Study of Final State Photons in Hadronic Z^0 Decay and Limits on New Phenomena*, Z. Phys. C **53**, 555 (1992).

[69] O. Adriani *et al.* (L3 Collaboration), *Determination of the number of light neutrino species*, Phys. Lett. B **292**, 463 (1992).

[70] D, Elvira, *Jet Energy Scale at D0*, DØ Note 3287, 2001 (unpublished).

[71] F. Hsieh and H. Lan, *Post-CAFIX Jet Corrections For Top Mass Analyses*, DØ Note 3055, 1996 (unpublished).

[72] F. Hsieh, *Study of the Jet Energy Scale Using γ + 1 jet Events*, DØ Note 3130, 1996 (unpublished).

[73] B. Abbott *et al.* (DØ Collaboration), *Direct Measurement of the Top Quark Mass by the DØ Collaboration*, Phys. Rev. D **58**, 052001 (1998).

[74] S. Abachi et. al. (DØ Collaboration), *Top Quark Search with the DØ 1992-1993 Data Sample*, Phys. Rev. D **52**, 4877 (1995).

[75] B. Abbott, *et al.* (DØ Collaboration), *Determination of the Absolute Jet Energy Scale in the DØ Calorimeters*, Nucl. Inst. Meth. **A424**, 352; DØ Notes 3287 and 3288, 1999 (unpublished).

[76] V. M. Abazov *et al.* (DØ Collaboration), *A precision measurement of the mass of the top quark*, Nature **429**, 638 (2004).

[77] V. M. Abazov *et al.* (DØ Collaboration), *Helicity of the W Boson in Lepton+Jets $t\bar{t}$ Events*, Phys. Lett. B **617**, 1 (2005); F. Canelli, Ph. D. Thesis, University of Rochester, 2003.

[78] A. van Doren and L. de Ridder, *An Adaptive Algorithm for Numerical Integration over an n-dimensional Cube*, J. Comput. Appl. Math. **2**, 207 (1976).

[79] G. P. Lepage, *A New Algorithm for Adaptive Multidimensional Integration*, J. Comp. Phys. **27**, 192 (1978); *VEGAS: An adaptive Multidimensional Integration Program*, CLNS-80/447, Cornell University (1980).

[80] G. Marchesini, B.R. Webber, G. Abbiendi, I.G. Knowles, M.H. Seymour, and L. Stanco, Computer Phys. Commun. **67**, 465 (1992)

[81] T. Sjöstrand, P. Eden, C. Friberg, L. Lönnblad, G. Miu, S. Mrenna, and E. Norrbin, Comp. Phys. Commun. **135** 238 (2001); *PYTHIA 6.206 Physics and Manual*, hep-ph/0108264.

[82] F.A. Berends, H. Kuijf, B. Tausk, and W.T. Giele, *On the production of a W and jets at hadron colliders*, Nucl. Phys. **B357**, 32 (1991).

[83] F. James, CERN Program Lib. D506 http://wwwasdoc.web.cern.ch/wwwasdoc/minuit

[84] D. Bickel, *Robust Estimators of the Mode and Skewness of Continuous Data*, Computational Statistics and Data Analysis **39**, 153 (2002).

[85] A. Jonckheere, *DØGEANT User's Guide*, DØ note 969, 1990 (unpublished).

[86] F. Carminati *et al.*, *The GEANT Manual*, CERN, Geneva 1996 (unpublished).

[87] S. Snyder, *Measurement of the Top Quark Mass at DØ*, Ph.D. Thesis, SUNY, Stony Brook, 1995.

[88] H. Baer, F. E. Paige, S. D. Protopescu, and X. Tata, *ISAJET 7.40: A Monte Carlo Event Generator for P P, Anti P P, and e+ e- reactions*, hep-ph/9810440.

Appendix A

Phase Space Calculation for Single Lepton $t\bar{t}$ Events

For a six-body decay in $q\overline{q} \to t\bar{t}$ events like the one in Fig. A.1, the Lorentz invariant phase space is given by the 4-momentum of the initial-state (q_1,q_2) and final-state ($p_{q's}, p_e, p_\nu$) particles [3]:

$$d\Phi_6(q_1 + q_2; p_1, p_2, p_3, p_4, p_e, p_\nu) = \delta^4(q_1 + q_2 - \sum_{i=1}^{6} p_i) \prod_{i=1}^{6} \frac{d^3 \overrightarrow{p}_i}{(2\pi)^3 2E_i} \quad . \tag{A.1}$$

As discussed in subsection 4.2.3, to perform the numerical integration that leads to the event probability, it is advantageous to transform the integration variables from the particles' momentum to $(\overrightarrow{\Omega}_{quarks}, \rho_1, M_1, m_1, M_2, m_2, \overrightarrow{p}_e)$, where $\overrightarrow{\Omega}_{quarks}$ are the solid angles of the final-state quarks, $\rho_i = |\overrightarrow{p}_{quark_i}|$ is the modulus of the momentum of the i-th quark, and (M, m) are the top and W masses.

Instead of performing the Jacobian transformation of the variables, the ρ_i (first transformed from $\overrightarrow{p}_{quark_i}$) can be transformed by introducing δ-functions of the mass variables, and integrate over ρ_i (with the δ-functions), taking into account the

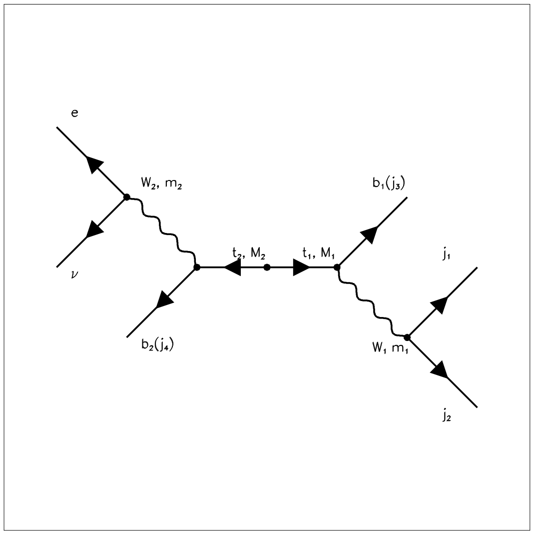

Figure A.1: Feynman diagram for the single-lepton $t\bar{t}$ event.

relations between ρ_i and the masses.

To uncover all the relations between the masses and ρ_i, we first integrated the energy-momentum δ-functions in Eq. A.1 over the transverse components (p_x, p_y) of the neutrino's momentum and x_1, x_2 of Eq. 4.1. This results in the following four constraints:

$$\begin{pmatrix} \sum_{i=1}^{6} E_i \\ \sum_{i=1}^{6} p_i^z \\ \sum_{i=1}^{6} p_i^x \\ \sum_{i=1}^{6} p_i^y \end{pmatrix} = \begin{pmatrix} E_{q_1} + E_{q_2} \\ p_{q_1}^z + p_{q_2}^z \\ 0 \\ 0 \end{pmatrix} \tag{A.2}$$

For the all hadronic branch, we have

$$\begin{aligned}\prod_{i=1}^{3}\frac{d^3\overrightarrow{p}_i}{(2\pi)^3 2E_i} &= \delta(p_{W_1}^2-m_1^2)dm_1^2\;\delta(p_{t_1}^2-M_1^2)dM_1^2\;\prod_{i=1}^{3}\frac{d^3\overrightarrow{p}_i}{(2\pi)^3 2E_i} \\ &= \frac{dm_1^2\;dM_1^2\;d\rho_1}{\left|\frac{\partial p_{W_1}^2}{\partial\rho_2}\right|\;\left|\frac{\partial p_{t_1}^2}{\partial\rho_3}\right|}\;\prod_{i=1}^{3}\frac{\rho_i^2 d\Omega_i}{(2\pi)^3 2E_i}\end{aligned} \tag{A.3}$$

in the last step the δ-functions were integrated with respect to ρ_2 and ρ_3 using the relation:

$$\int f(x)\delta[g(x)]dx = \frac{f(a)}{|g'(a)|} \quad ,\text{with} \quad g(a)=0 \quad . \tag{A.4}$$

The values of the partial derivatives are:

$$\begin{aligned}\frac{\partial p_{W_1}^2}{\partial\rho_2} &= \frac{\partial(p_1+p_2)^2}{\partial\rho_2} \\ &= \frac{\partial}{\partial\rho_2}(m_1^2+m_2^2+2E_1E_2-2\rho_1\rho_2 cos\theta_{12}) \\ &= 2E_1\frac{\rho_2}{E_2}-2\rho_1 cos\theta_{12}\end{aligned} \tag{A.5}$$

and

$$\begin{aligned}\frac{\partial p_{t_1}^2}{\partial\rho_3} &= \frac{\partial(p_1+p_2+p_3)^2}{\partial\rho_3} \\ &= \frac{\partial}{\partial\rho_3}(m_1^2+m_2^2+m_3^2+2\,p_1\cdot p_2+2E_1E_3-2\rho_1\rho_3 cos\theta_{13}+2E_2E_3-2\rho_2\rho_3 cos\theta_{23}) \\ &= 2E_1\frac{\rho_3}{E_3}-2\rho_1 cos\theta_{13}+2E_2\frac{\rho_3}{E_3}-2\rho_2 cos\theta_{23} \quad .\end{aligned} \tag{A.6}$$

For the leptonic branch the integration of the δ-functions is performed over ρ_4 and the neutrino's longitudinal momentum p^z_ν. The values of the derivatives are

$$\begin{aligned}\frac{\partial p^2_{W_2}}{\partial p^z_\nu} &= \frac{\partial (p_e + p_\nu)^2}{\partial p^z_\nu} \\ &= \frac{\partial}{\partial p^z_\nu}(m_e^2 + m_\nu^2 + 2E_eE_\nu - 2p^z_e p^z_\nu - 2\vec{p}^{\,t}_e \cdot \vec{p}^{\,t}_\nu) \\ &= 2E_e\frac{p^z_\nu}{E_\nu} - 2p^z_e\end{aligned} \tag{A.7}$$

and

$$\begin{aligned}\frac{\partial p^2_{t_2}}{\partial \rho_4} &= \frac{\partial (p_e + p_\nu + p_4)^2}{\partial \rho_4} \\ &= \frac{\partial}{\partial \rho_4}(m_e^2 + m_\nu^2 + m_4^2 + 2\,p_e \cdot p_\nu + 2E_eE_4 - 2\rho_e\rho_4 cos\theta_{e4} + 2E_\nu E_4 - 2\rho_\nu\rho_4 cos\theta_{\nu 4}) \\ &= 2E_e\frac{\rho_4}{E_4} - 2\rho_e cos\theta_{e4} + 2E_\nu\frac{\rho_4}{E_4} + 2E_4\frac{\rho_\nu}{E_\nu}\frac{\partial\rho_\nu}{\partial\rho_4} - 2\rho_\nu cos\theta_{\nu 4} - 2\frac{\partial\rho_\nu}{\partial\rho_4}cos\theta_{\nu 4} \quad .\end{aligned} \tag{A.8}$$

where $\frac{\partial\rho_\nu}{\partial\rho_4}$ is given by Eq. A.2 and the W-mass constraint.

Combining everything together, the phase space for $t\bar{t}$ events is

$$\begin{aligned}d\Phi_6 = &\frac{d^3\vec{p}_e}{(2\pi)^3 2E_e}\frac{d\rho_1}{(2\pi)^3 2E_\nu}\prod_{i=1}^{4}\frac{\rho_i^2 d\Omega_i}{(2\pi)^3 2E_i} \\ &\times \frac{dm_1^2}{|2E_1\frac{\rho_2}{E_2} - 2\rho_1 cos\theta_{12}|}\frac{dM_1^2}{|2E_1\frac{\rho_3}{E_3} - 2\rho_1 cos\theta_{13} + 2E_2\frac{\rho_3}{E_3} - 2\rho_2 cos\theta_{23}|} \\ &\times \frac{dm_2^2}{|2E_e\frac{p^z_\nu}{E_\nu} - 2p^z_e|}\frac{dM_2^2}{|2E_e\frac{\rho_4}{E_4} - 2\rho_e cos\theta_{e4} + 2E_\nu\frac{\rho_4}{E_4} - 2\rho_\nu cos\theta_{\nu 4}|} \quad .\end{aligned} \tag{A.9}$$